Dynamics of Thin Films through Molecular Simulations

Muhammad Rizwanur Rahman

Department of Mechanical Engineering

Imperial College London

Submitted in partial fulfillment of the requirements for the degree of
Doctor of Philosophy
and for the Diploma of Imperial College

This page intentionally left blank.

Declarations

Declaration of Originality

This thesis describes works carried out in the Department of Mechanical Engineering, Imperial College London. The work is *my own*, except otherwise acknowledged. This work builds upon an impressive body of literature, the discussion of which is appropriately referenced; any direct quotes are in *italics*. All other texts/figures are written/generated by myself with assistance from Daniele Dini, Edward R Smith, Li Shen, James P Ewen, and David M Heyes.

Copyright Statement

The copyright of this thesis rests with the author. Unless otherwise indicated, its contents are licensed under a Creative Commons Attribution-Non Commercial 4.0 International Licence (CC BY-NC). Under this licence, you may copy and redistribute the material in any medium or format. You may also create and distribute modified versions of the work. This is on the condition that: you credit the author and do not use it, or any derivative works, for a commercial purpose. When reusing or sharing this work, ensure you make the licence terms clear to others by naming the licence and linking to the licence text. Where a work has been adapted, you should indicate that the work has been changed and describe those changes. Please seek permission from the copyright holder for uses of this work that are not included in this licence or permitted under UK Copyright Law.

IMPERIAL

This page intentionally left blank.

Dynamics of Thin Films through Molecular Simulations

Abstract

Thin liquid films play pivotal roles in various natural phenomena and engineering processes. Yet, our understanding is limited by the scarcity of atomic insights. This work investigates the nanoscopic details of thin films and their rupture, and the transport of surfactants along the film surfaces. At this scale, experimental investigations are prohibitive; and conventional theoretical approaches are inadequate due to their reductive approximations. Therefore, this work employs molecular dynamics simulations which enables the examination at the most fundamental scale.

Present investigations of film interfaces through stress-cluster analysis reveals that higher temperature results in a more disconnected surface stress-field, contributing to an overall decrease in surface tension. Local variation of surface tension is responsible for Marangoni convection leading to rupture. The processes by which these rupture sites emerge − traditionally categorized as spinodal and heterogeneous rupture − are found to share similar molecular origin. Present study on the growth of rupture sites identified the limitations of continuum scale theories in explaining retraction rates for thinner films, and corrections are proposed that rectify the discrepancies. Notably, a spatio-temporal memory of rupture is identified, highlighting the concept of deterministic outcomes emerging from stochastic processes.

Finally, the transport mechanism of surfactant molecules, along the deforming surfaces of thin films and droplets, is investigated. The continuum scale transport equation is solved by employing a finite difference scheme, incorporating inputs from MD simulations. This model provides confirmation of the validity of the transport equation at the nanoscale. By uniquely confirming the applicability of the transport equation for a molecularly thin film, this study elucidates the long-debated relation-

ship between the continuum and the nanoscale. Together, the findings from this research represent an important step in bridging the physics of fluids across scales, offering new insights to the dynamics of thin films.

SUPERVISORS

Professor Daniele Dini
Professor in Tribology (Head), Director of Research
Fellow of the Royal Academy of Engineering
Shell/RAEng Chair in Complex Engineering Interfaces
Department of Mechanical Engineering, Imperial College London.

Dr. Edward Smith
Senior Lecturer in Multiscale Fluid Dynamics
Department of Mechanical and Aerospace Engineering
Brunel University London.

Dr. James P Ewen
Royal Academy of Engineering Research Fellow
Department of Mechanical Engineering
Imperial College London.

EXAMINERS

Prof. Erich Muller
Professor of Thermodynamics
Fellow of the Royal Society of Chemistry
Department of Chemical Engineering
Imperial College London.

Dr. Rohit Pillai
Senior Lecturer
Department of Mechanical Engineering
University of Edinburgh.

Acknowledgments

Words seem surprisingly inadequate, and the scope of this document too limited to fully express my thanks to those without whom this journey would have been impossible. Thus, this acknowledgment is far from complete.

To *Prof. Daniele Dini* − I continually marveled at the depth of Daniele's understanding, the magnitude of his integrity and dedication in nurturing the next-generation of scientists, his remarkable insights in portraying the 'Big Picture', and his extraordinary ability to relate physics across scales − from principles to practice. "Never stop doing science wherever you are" Daniele said. Whether in academic research or in personal quest, Daniele was always there, and as he has promised, will always be there − which I have absolute confidence in. To *Dr. Edward Smith* − who has always been exceptional in guiding me through this journey. Ed never stopped asking the right question, and encouraging to address the origin of the problem. When I was mired in the minute details, or in any philosophical conundrum, Ed never gave up on me, and always extended a hand. Without him, this thesis would never be what it is today. Thank you. To *Prof. David Heyes* − it has been an honor working with, it is rare to meet a revered scientist of his stature who is as generous and humble. To *Dr. Li Shen* − who tirelessly spent countless hours with me, discussing films and bubbles which often transcended the physics of films, weaving through the coherence of the universe, of sociology, or even of the human nature. To *Dr. James Ewen* − who was always steps ahead in any topic, knowing almost the entirety of the literature. Before I knew it, my wonderful times at Imperial had drawn to a close, leaving behind a treasure of memories and insights.

To my parents, Prof. A. K. M. Shafiqur Rahman and Prof. Razia Begum − to whom I owe everything, for all that has come before and all that will follow. My father always exemplifies the charismatic teacher I have looked up to since childhood. “Go around the world, a part of me will always be with you wherever you go”, my mom said, hiding her tears, as she bid me farewell for the first time, “just don’t forget where you belong”. To my sibling, Mushfiqur Rahman − for whom I could let many things go, knowing he is holding the fort strong. Stepping outside would be unimaginable if he wasn’t there for me. To my late father-in-law, Nasir Ahmad − within a very short time, he left a lasting impression. And, to my beautiful wife, Nusrat Ahmad − not only did she relentlessly put up with all my eccentricities and idiosyncrasies, she also sacrificed many of her own dreams for the sake of mine. I never thanked. This journey belongs as much to her as it does to me.

To my uncle Dr. Shahiduzzaman Harun − who has been the north star in our family, thanking him is never enough. To Dr. Shabbir Mustafiz − the constant supervisor in my life outside of academia, the true extent of his contributions is impossible to sketch. I wish my ‘Chachamia’ were still alive today. To Prof. Morris Flynn, Dr. Prashant Waghmare, Prof. Toufique Hasan, Prof. Nasim Hasan, Prof. Hamid Kalim, and all my teachers who have played a part. To Dr. Anjan Goswami, Dr. Abhishek Kumar Ghosh, and my dear friend Plabon − with whom I shared countless enlightening conversations, I am indebted to them.

To the trustees of Beit Fellowship for Scientific Research, Shell University Technology Center, and the Department of Mechanical Engineering of Imperial College London, for funding my PhD. Special thanks to Erik, Ben, Carlos Corral-Casas, Jason, Eliane, Stavros and Paul-Anael for their help, and many fruitful discussions. I am thankful to Prof. Erich Muller, and Dr. Rohit Pillai for their time to examine this thesis, and for the insightful discussions. Last, but not the least, I thank every member in Imperial Tribology Group, it has been a privilege being amidst them.

This page intentionally left blank.

Contents

Declarations **3**

Abstract **5**

Acknowledgments **8**

Dedication **19**

1 Preamble **23**

1.1 Laplace's Demon 24

1.2 The World of Neglected Dimensions 26

1.3 Thesis Outline 27

1.4 Scientific Communications 31

2 Introduction **33**

2.1 Thin Films Everywhere 34

2.2 Interfaces and Interfacial Forces 36

2.3 Interfacial Tension 37

2.4 Stability and Rupture of Thin Films 44

2.5 Thin Film Retraction: Taylor-Culick Theory 46

2.6 Transport of Surfactant along the Surface 48

2.7 Overview 52

Gallery: Lights and Colors **55**

Echoes of Imagery 63

3 Surface Structure: The Intrinsic Interface **65**
3.1 Introduction . . . 66
3.2 Simulation Details . . . 67
3.3 Interfacial Density profiles . . . 70
3.4 Interfacial Pressure Profiles . . . 73
3.5 Surface Stress and Fractal Dimension . . . 77
3.6 Percolating Stress Clusters at the Surface . . . 80
3.7 Summary . . . 84

4 Thin Film Rupture: Formation to Fragmentation **86**
4.1 Introduction . . . 87
4.2 Simulation Details: . . . 88
4.3 Overview of the Life Span of a Film . . . 91
4.4 Modes of Rupture . . . 92
4.5 Memory of Rupture . . . 96
4.6 Formation of a Nucleus . . . 103
4.7 Frustration and Coalescence . . . 107
4.8 Summary . . . 111

5 Thin Film Rupture: An Expanding Nucleus **114**
5.1 Introduction . . . 115
5.2 Simulation Details . . . 115
5.3 Nucleus Formation . . . 120
5.4 Short-Term Retraction . . . 121
5.5 Taylor-Culick Retraction . . . 122
5.6 Surface Tension Modulation by Temperature Rise . . . 123
5.7 Surface Tension Modulation due to Curvature . . . 125
5.8 Transition Regime . . . 128
5.9 Summary . . . 130

6 Transport on the Surface **132**
6.1 Introduction . . . 133
6.2 Problem Description . . . 134

6.3 Molecular Description of the System 134
6.4 Continuum Description of Surfactant Transport 139
6.5 Surfactant Transport 145
6.6 Spreading Length 149
6.7 Summary 151

7 Conclusion **153**
7.1 Key Findings 154
7.2 Future Works 158

Appendix A Appendix to Chapter 4 **162**
A.1 Nuclei Growth 163
A.2 Rupture Memory 165
A.3 Neighbor Effect on the Rupture Propagation 165
A.4 Further Details and Discussions 170

Appendix B Appendix to Chapter 6 **174**
B.1 A molecular version of the transport equation 175

Appendix C General Appendix **176**
C.1 Some definitions in MD simulations 176
C.2 Minkowski dimension 180

References **182**

List of Figures

2.1 The film around a bubble 35
2.2 Thin film - a molecular view 39
2.3 Bubbles and films 44
2.4 A collapsing bubble 47

3.1 Liquid-vapor coexistence 69
3.2 Surface density profiles 71
3.3 Oscillating intrinsic density profiles 72
3.4 Pressure profiles at surface layer 73
3.5 Pressure components 75
3.6 Net pressure at surface and surface tension 76
3.7 Stress map at surface 78
3.8 Percolation network of surface stress 81
3.9 Stress clusters at surface 82

4.1 Portrait of the life of a thin-film 92
4.2 Spontaneous rupture of thin films 93
4.3 Memory of rupture 97
4.4 Local energetics of rupture sites 101
4.5 Film stability, nucleus formation and growth 104
4.6 Early growth and velocity field 106
4.7 Frustration and coalescence 106
4.8 Growth and Frustration 108
4.9 Dewetting patterns 112

5.1 Thin film retraction 116
5.2 Thickness dependence of hole growth 119
5.3 Formation and Growth of a nucleus 119
5.4 Regimes of retraction, and correction to Taylor-Culick speed 121
5.5 Temperature field around an expanding nucleus 124
5.6 Temperature rise around an expanding nucleus 126
5.7 Curvature effects 127

6.1 Surfactant monolayer spreading on deforming surface 135
6.2 Molecular descriptions 136
6.3 Measurement of diffusion coefficient 138
6.4 Evolution of the surface 145
6.5 Spatio-temporal variation of surfactant concentration 146
6.6 Spatio-temporal variation of surfactant concentration - II 147
6.7 Variation of surfactant concentration on a droplet 148
6.8 Spreading of monolayer 149

7.1 Micelle Generator 160

A.1 Synthetic rupture 163
A.2 Coalescence of synthetic rupture sites 164
A.3 Rupture memory - II 166
A.4 An analogy for the concept of inherent structures 167
A.5 Neighbor effect 168
A.6 Neighbor effect on nucleus-evolution 169
A.7 Modality of dewetting 171
A.8 Surface corrugations and local thickness 173

C.1 Fractal dimension by box counting method 180

Nomenclature

Δs	Distance between two points x_1 and x_2 in curved coordinates along s axis following a deforming surface
Δx	Distance between two points x_1 and x_2 in rectangular coordinates along x axis
$\delta(\dots)$	Dirac delta function
ϵ	Infinitesimal distance
$\epsilon_{\gamma,\kappa}$	Correction arising from variation of γ due to curvature
$\epsilon_{\gamma,T}$	Correction arising due to the existence of a transition regime
$\epsilon_{\gamma,T}$	Correction arising from variation of γ due to temperature
Γ	Local surfactant concentration at t
γ	Surface tension
Γ_0	Local surfactant concentration at $t = t_0$
$\mathbf{e_n}$	Unit vector normal to the local surface
$\mathbf{e_n}$	Unit vector tangential to the local surface
$\mathbf{u_s}$	Velocity vector along the deforming surface
$\mathcal{H}$	Hamaker constant
μ	Viscosity
Φ	Fractal dimension
ρ	Density

τ_i Inertial time scale

ε Strength of interaction between two particles at a separation distance r

ς Length of a grid/box for covering a fractal area

ζ Function fitting an instantaneous liquid-vapor surface

D_s Surface diffusion coefficient

h_0 Film's initial thickness

Oh Ohnesorge number

$P_{\text{Config.}}$ Configurational contribution of pressure

$P_{\text{Kin.}}$ Kinetic contribution of pressure

P_{SM} Pressure contribution due to surface movements

P_N Pressure normal to the surface

P_T Pressure tangential to the surface

R_0 Initial radius of a rupture site

r_c Cut-off radius

t_0 Time of restarting a simulation

t_n Time of nucleation of the first rupture site

U^* Non-dimensional retraction speed, U/U_{TC}

U_{TC} Taylor-Culick retraction speed

V Interaction Potential

This page intentionally left blank.

To

Abbu & Ammu

– who have been the best university I've ever attended.

This page intentionally left blank.

বেড়ার নিয়ম ভাঙলেই পথের নিয়ম আপনিই বেরিয়ে পড়ে।
(Break the trail's bounds, and new paths will unfold.)
−Rabindranath Tagore

The moving finger writes; and, having writ,
Moves on: nor all thy piety nor wit
Shall lure it back to cancel half a line,
Nor all thy tears wash out a word of it.

– Omar Khayyam

This page intentionally left blank.

The butterfly counts not months but moments,
and has time enough.

Rabindranath Tagore

1 Preamble

1.1 Laplace's Demon

Once upon a time, 'Love' and 'Hate' were believed to be the twin fundamental forces governing all natural processes. This poetic contrast of the ancient Greek philosophers formed the very foundation of the 'chemical theory' for nearly two millennia (Israelachvili, 2011). As centuries passed, the abstract ideas of viewing natural phenomena as manifestations of mysterious forces evolved, and mankind transcended from non-empirical philosophical interpretations to an evidence based scientific worldview. The journey to understand how natural forces act on objects, and how objects react to the forces − from minuscule particles to vast celestial bodies − was a long and winding road that traversed the works of Aristotle (384-322 BC), Ibn Sina (980-1037), and Galileo (1564-1642), reaching its pinnacle with Sir Isaac Newton (1643-1727). Newton, arguably the most pivotal figure in the history of science, gave the working definition of the conservation of momentum that governs motion from Earth to the heavens. In contrast to the ancient mysterious forces, modern physics has progressed to describe nature through the lens of the complex interplay of the four fundamental forces: weak and strong nuclear forces acting at the sub-atomic scale, the electromagnetic force defining the intermolecular interactions that dictate physics at atomic and molecular scales, and the gravitational force that governs the motion and structure of celestial bodies across the vastness of space. These forces collectively explain the full spectrum of physical phenomena, from the incredibly small to the expansively large.

The potential of classical mechanics formalized by Newton, and furthered through the works of Leibniz, Pascal, Lagrange, Euler and other contemporary scientists, intrigued Pierre-Simon Marquis de Laplace (1749–1827) to imagine a 'vast intellect' often referred to as 'Laplace's demon'. If the positions and velocities of all particles in the universe at this very moment were known, as well as the forces acting upon these particles, by applying Newton's laws of motion, this intellect could precisely forecast the unfolding of events one moment after another, ad infinitum (Carroll, 2017, 2022). And, as Laplace's thoughts continued, 'the future just like the past would be present before its eyes'.

Although Laplace's philosophical view of a deterministic world faced substantial criticism*, in practice, majority of the physical and engineering applications do not necessitate an understanding of the entire universe, but only of tiny subsystems that are well within the bounds of Newtonian mechanics. Many engineering challenges focus on understanding a system's behavior and the underlying mechanisms, rather than predicting its future. Niels Bohr aptly remarked, "It is difficult to make predictions, especially about the future," highlighting the inherent complexity of forecasting outcomes. Having these in mind, modern technology, although limited, proves exceedingly capable in handling small systems (down to the microns and sub-microns), effectively acting as a miniature, and localized version of 'Laplace's demon' within these confined domains. Molecular Dynamics (MD) simulations exemplify this principle by providing a powerful tool to explore the behavior of matter at the atomic and molecular levels. This capability extends particularly to areas where theoretical simplifications must otherwise be made to render problems tractable, or where direct experimental investigation would perturb the system altering its intrinsic properties. For example, in the study of non-equilibrium nanoscale phenomena, where traditional experimental approaches might disrupt the system, MD simulations provide a non-intrusive means to observe and predict molecular behavior. It is precisely this reason why, this thesis employs MD to investigate the dynamics of thin films − a topic of active research where neither experimental investigations are straightforward, nor can reductive theoretical models adequately capture the underlying mechanisms.

The capability of MD naturally leads to a discussion on the reliability of the results

* Laplace's idea of a deterministic universe has been met with critique and opposing views. The central argument is even if such an extraordinary intellect existed, it would still struggle to predict the past and future based solely on the current state of the universe for several reasons. Firstly, without possessing infinite precision in the knowledge of particles' locations and momentum, even the smallest inaccuracies could trigger the butterfly effect, leading to significant deviations over time. Secondly, the inherent probabilistic nature of the universe, as given by the uncertainty principle, prohibits this intellect from simultaneously knowing both the momentum and position of particles with absolute certainty − if one is known precisely, the other must remain uncertain. Moreover, the second law of thermodynamics introduces another fundamental obstacle by asserting the irreversibility of universal processes, implying that it is impossible to determine the past with certainty from the current state (Robertson, 2021).

derived from simulations. Indeed, the accuracy of the model critically depends on the quality of the empirical force fields and the molecular models employed to simulate a real system. If discrepancies arise between the simulation outcomes and experimental observations, it suggests a need for refinement in the model parameters, or the force fields. Conversely, if simplified theoretical predictions fail to align with MD results, this indicates a need for adjustments in the theoretical frameworks themselves (Frenkel et al., 1996). Thus, MD connects empirical observations and approximation based theoretical frameworks, by providing a detailed view into the immeasurably small-scale molecular world and their measurable impacts at observable scale. It is this unique property of MD that leads to its frequent characterization as 'computer experiments'.

1.2 The World of Neglected Dimensions

Wolfgang Ostwald famously described the surface as a 'world of neglected dimensions' due to our historically limited understanding of it (Myers et al., 1999). This 'twilight zone,' spanning just a few nanometers between two bulk phases, hosts complex phenomena that often effect the overall dynamics. In a system where a liquid coexists with its vapor, the boundary between the two phases, i.e., the liquid-vapor surface, is typically only a few nanometers thick. When the depth of the liquid phase in such a system is reduced to an extent where it becomes comparable to the interfacial thickness, the scenario fundamentally changes. Such a system qualifies as a thin film where any variation or disturbance at the surface can propagate through the entire film, significantly affecting its overall behavior. If one wishes to put some numbers, the thickness of thin films may vary between few nanometers to few microns; for a scale of comparison, the thickness of human hair is about 80 microns.

Despite their seemingly negligible dimensions, thin films play a crucial role in a wide array of natural and technological processes, ranging from pulmonary respiration to cutting-edge nanotechnology. Given these critical applications, a more detailed and in-depth examination is imperative. However, the traditional continuum framework often falls short in elucidating the mechanisms that govern dynamics at this scale, leading to discrepancies between experimental measurements and theoretical predic-

tions (Maldarelli et al., 2022). Additionally, at such small scales, thermal fluctuations become increasingly significant. Moreover, experimental methods for probing most dynamical properties of thin films are not straightforward (which will be clear as we progress through this thesis), complicating the direct observation and study of nanoscale processes.

The focal points of the research described here center around such complex scenarios. Specifically, the spontaneous rupture of thin films must originate at a fundamental scale where thermal fluctuations play a critical role and cannot be overlooked. In studies of perturbed rupture, clear discrepancies between the theory and observations at scales below one hundred nanometers are well known; the causes of this anomaly remained largely unexplained. From a more practical standpoint, our understanding of the transport mechanisms in deforming thin films is crucial for a multitude of applications, yet this knowledge is notably inadequate.

1.3 Thesis Outline

The introductory chapter of this thesis, *Chapter 2*, briefly charts our current understanding of thin films and surfaces, as well as their significance across various scientific and engineering disciplines. Despite the abundance and importance, several significant gaps remain in the literature - some of which *Chapter 2* illustrates, and the subsequent chapters aim to resolve.

.....

Chapter 3 decouples the surface properties from thermal fluctuations to attain a clearer view of the construction of the surfaces of a thin film, the surface tension and its response to thermodynamic conditions. The methodology employed to calculate the surface tension of the inhomogeneous liquid-vapor interface has been detailed, and the concept of percolating stress network - a new perspective to the surface - is introduced. The highlights of the chapter include:

– Through non-equilibrium molecular dynamics simulations together with an intrinsic sampling method, the sharpest possible view of the outermost molecular

layer of the interface is obtained, which allows careful examination of the different aspects of the properties of these layers in a high resolution.

- Particular attention is given to the understanding of how stress distributes on the surface. This tends to result from the molecular interactions at the interface and depends on a variation of temperature.
- By applying the concepts of fractal dimension and percolating network often used in analyzing complex geometric shapes, and connectivity, this chapter proposes that an interface can be thought of as held together by a connected network of stresses, and this 'connectedness' of such a network decrease as the temperature increases, which in turn results in a decrease in overall surface tension.

The interfacial stress network is the first step towards characterizing the liquid-vapor interface as a mesh of connected networks and how this network is affected by changing external conditions (such as temperature, presence of surfactants, etc.) and intrinsic properties (such as curvature in the case of a bubble).

Chapter 4, which forms the heart of this thesis simulates a freely suspended thin liquid film, and portrays the complete life span of a thin film - all the way from hydrodynamic drainage to the fluctuation-driven black film (films thinner than few tens of nanometers when films appear black due to destructive interference) formation, to stochastic nucleation, to their geometrical frustration, ultimately leading to deterministic coarsening. This study primarily relied on non-equilibrium molecular dynamics simulations, supplemented by finite element analysis in select sections. Key discoveries of this chapter include:

- A spatio-temporal memory of rupture is uncovered which supports the general idea of deterministic outcomes arising from stochastic processes. This underscores the importance of the liquid's inherent structure in predicting the otherwise random nucleation, and explains why the local-parameters fail to predict an impending rupture event.
- This work reveals that the so-called 'heterogeneous' nucleation may occur even without the presence of any defect or impurity of the substrate; and unifies the emerging morphologies commonly characterized as spinodal and heterogeneous nucleation.

– Through a systematic study of the neighbor effect on nucleus growth, a frustrated growth regime is characterized which leads to delayed coalescence and coarsening. This frustrated regime proposes a first-order correction to the classical film retraction theory.

While offering fresh insights into thin film rupture dynamics, the findings presented in this chapter open up new avenues of research, specially when placed in the context of its use in a plethora of applications, e.g. liquid metals, interfaces in the presence of surfactants and additives, complex coatings, distillations, capillary phenomena, surface deformation, atomization and fragmentation.

Chapter 5 extends the film rupture study, but for a single isolated nucleus - which is generally described by the celebrated Taylor-Culick theory. Despite its overwhelming importance, this classical theory of thin-film retraction is limited by its erroneous prediction for films with thickness below 100 nm; the scale at which rupture begins. Work described in this chapter unearths the atomic-scale origins of the retraction process, and corrects the existing theory to provide an accurate understanding of the problem across the scales. The key findings of this chapter:

– A reduction of local surface tension at the film front is confirmed. Further analyses prove that this drop in local surface tension is caused by thermal effects and curvature.

– A transition regime between the retracting film-front (rim) and the (far-field) unperturbed film in identified, which was ignored in the classical formulation (TC).

– Corrections to the TC theory for nanoscopic films are proposed and justified.

This study, while giving unique new insights to rupture for molecularly thin films, also creates avenues to further the ideas to more complex liquid-vapor systems.

Chapter 6 focuses on a more practical problem, where the transport mechanisms of surfactant monolayers on the deforming surface of a thin liquid film are investigated. Concurrently, the continuum scale transport equation is solved through a finite difference scheme, incorporating inputs from molecular simulations.

– Findings provide the first confirmation of the validity of the continuum transport equation at the nanoscale.

By uniquely confirming the applicability of the transport equation for a molecularly thin film, this study elucidates the long-debated relationship between the continuum scale − where long-wave approximations prevail, and the nanoscale − where their validity ceases.

Chapter 7 concludes this thesis by providing a brief summary of the findings, their potential applications, scope to improve and extend the current work, as well as a layout for future research ideas.

1.4 Scientific Communications

Journal publications

4. *Nanoscale Surfactant Transport: Bridging Molecular and Continuum Models*, **MR Rahman**, L Shen, JP Ewen, DM Heyes, D Dini, ER Smith (under review).
3. *Life and Death of a Thin Liquid Film*, **MR Rahman**, L Shen, JP Ewen, DM Heyes, D Dini, ER Smith, Communications Physics, Nature, 2024.
2. *Non-equilibrium molecular simulations of thin film rupture*, **MR Rahman**, L Shen, JP Ewen, B Collard, DM Heyes, D Dini, ER Smith, The Journal of Chemical Physics, 2023.
1. *The Intrinsic Fragility of the Liquid–Vapor Interface: A Stress Network Perspective*, **MR Rahman**, L Shen, JP Ewen, D Dini, ER Smith, Langmuir, 2022.

Conference presentations

3. Thin Film Dynamics: Formation, Frustration and Fragmentation, 3^{rd} meeting of the UK Fluid Network Special Interest Group on Non-Equilibrium Molecular Dynamics, Imperial College London, London, UK, 2024.
2. Propagation of Thin-Film Rupture at the Atomic Scale, 75^{th} Annual Meeting of the Division of Fluid Dynamics, American Physical Society, Indianapolis, USA, 2022.
1. Intrinsic Stress Network and the Perception of Surface Tension, American Physical Society's March Meeting, Chicago, USA, 2022.

Talks

4. Surfactant Transport on Thin Films, Shell Global Solutions, Hamburg, Germany, 2024.
3. Dynamics of Clean and Surfactant Laden Thin Films, Shell Surfactant Network, (online) 2024.
2. Rupture of Molecularly Thin Films, Brunel University London, UK, 2023.
1. Molecular Insights of Thin Film Rupture, Shell Global Solutions, Hamburg, Germany, 2023.

This page intentionally left blank.

We live on an island surrounded by a sea of ignorance. As our island of knowledge grows, so does the shore of our ignorance.

John Archibald Wheeler

2 Introduction

2.1 Thin Films Everywhere

From the swift blink of an eye to the sleek surface of today's *oled* screens of a smart phone, to the hundreds of semiconductors inside it, and even the majestic sweep of snow avalanches, a closer examination reveals that thin films are the silent arbiters of both nature's whims and technological advancements. Though slender in dimension, their influence is anything but negligible, as is the complex physics governing their dynamics. Our formal understanding of thin films can be dated back to Beauchamp Towers in 1883 who studied how oil layers influence the frictional behavior in high sliding velocities. Towers faced harsh criticism though, an excerpt (Craster and Matar, 2009) -

> *... So-called scientific research is rapidly becoming nothing but a method by which considerable incomes may be earned in finding out things of no earthly use to any mortal. (T. C. H. Birmingham, Letter to the editor, The Engineer, 1884.)*

This very study however, motivated Osborne Reynolds (Reynolds, 1886) to substantially simplify the Navier-Stokes equations with the assumptions of viscous flow in thin channels. Reynolds' reduced version of the Navier-Stokes equations is what we now know as the 'Lubrication Theory', an essential ingredient in today's numerous engineering applications.

Modern science has established the vast significance that thin films hold in a wide spectrum of applications (Craster and Matar, 2009; Durán-Olivencia et al., 2019), ranging from natural processes like gravity currents, lava flows, and oceanic science (Ancey, 2007; Goldstein et al., 2014) to biological transport processes in lungs and cell membranes, tear-films in our eyes, and in disease transmission and forensic analyses (Bourouiba, 2021; Grotberg, 2001; Tammaro et al., 2021; Villermaux, 2020), to more common place engineering applications in miniaturized micro-electronic, micro-fluidic and biomedical devices (Griesser, 2016; Piegari and Flory, 2018; Stone et al., 2004), complex coatings, distillations and insulation (Eijkel and Berg, 2005; Stone et al., 2004) - to name a few. As the recognition of their importance has grown, so too has the scientific literature on thin films become richer and more extensive, giving rise to an entirely new branch of physics dedicated to thin films. Our understanding of

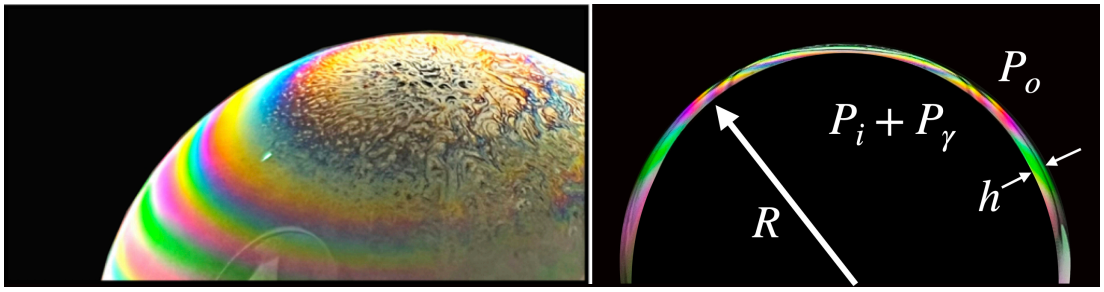


Figure 2.1: Figure at the left showing interference patterns on a soap bubble representing the spatial variation of thickness. Figure at the right shows balance between the pressure inside and outside the bubble which is established by an additional pressure related to its curvature and surface tension.

thin films, therefore, has significantly advanced since the days of Reynolds. However, as the range of applications expands, the need for a deeper understanding of the underlying physics has become increasingly imperative.

2.1.1 What is a thin film ?

Most macroscopic engineering applications involve three-dimensional bodies. From this viewpoint, thin films are somewhat of an anomaly due to their predominantly two-dimensional characteristics—the third dimension being so small as compared to the other dimensions. This unique attribute challenges conventional paradigms and necessitates a distinct approach to both study and application. For example, the dominance of gravity diminishes, and surface forces and instabilities gain increasing importance. It is virtually impossible to answer how 'thin' a film should be so as to qualify as a 'thin film', rather the thin film limit is determined by the appearance of anomalies, the predominance of surface forces and the impact of many surface events (Eckertova, 2012). Generally speaking, particularly in technological applications, thin films involve a layer of material typically ranging from a few tens of nanometers to several micrometers in thickness. In these films, the two surfaces are in close proximity, causing the surface properties to exert a significant influence on the overall physical behavior of the system (Eckertova, 2012).

Depending on their applications, thin films can be composed of various materials,

such as simple or amorphous liquids, polymers, and liquid metals. They can exist as suspended (soap bubbles, foams), supported (coatings, paintings, adhesive), or confined (films adhered to the inner surface of hollow tubes) between solid walls. While the liquid shell of a soap bubble (Fig. 2.1, image taken for current study, motivated by previous works of Shen et al.), coatings, or the 'tears of wine' (which are thin films that climb up the sides of a glass due to surface tension gradient) are outright examples from day-to-day observation, the earliest application of thin films dates back approximately 5000 years, when the ancient Egyptians employed thin layers of gold on base-metal statues (Greene, 2014). This technique certainly served decorative purposes (also for deception?), but may have also been used to protect the artifacts from corrosion.

2.2 Interfaces and Interfacial Forces

> *The history of the statistical theory of phase transition and related problems teaches us that progress has come more often from 'good' solutions for idealized models than from solutions for realistic systems that require ill-defined approximations (Rowlinson and Widom, 2013).*

2.2.1 Interface

The surfaces* of a thin film are of paramount importance, for they act as the origin of various surface forces, and their respective consequences. Below the capillary length scale, surface force dominates gravity and becomes the deciding factor in myriad surface phenomenon. The surface, or the interface can be defined as the contact area of two different phases, i.e., liquid-liquid and liquid-gas referred to as fluid interfaces, and solid-liquid, solid-gas, and solid-solid known as non-fluid or solid interfaces (Barnes and Gentle, 2011). This thesis concerns about freely suspended (i.e., unsupported) liquid films, hence all films discussed herein have two free liquid-vapor interfaces; discussions that follow are confined only to these cases.

The dynamics of the liquid-vapor interface are pivotal, and often the primary descriptor, in myriad processes. To characterize the interface, a number of approaches

*'Surface' and 'interface' are used interchangeably in this thesis.

have been developed over the past century, from macro-scale treatment (De Gennes et al., 2013) to the sophisticated molecular dynamics (MD) simulations (Ghoufi et al., 2016), which have changed our perception of the interface quite dramatically (Tarazona et al., 2012a).

From a macroscopic perspective, an interface, or a surface, as these words refer to, is of zero thickness and contains zero mass. The transition between the two homogeneous bulk phases is (macroscopically) smooth and monotonic. This simplistic picture of the surface formed the early stage of the theory of capillarity based on the works of Young and Laplace (Rowlinson and Widom, 2013). However, when viewed with molecular details, surfaces are of non-zero finite thickness, and an inhomogeneous interfacial region emerges between the two bulk phases rendering the physics much more complicated.

God made the bulk; the surface was invented by the devil. – Wolfgang Pauli

At the microscopic scale, the transition must be continuous, not a step function. For the interface between a smooth solid and gas, this transition will naturally occur within a layer that is one molecule thick. But this region is much thicker, in the range of several molecular diameters, for a liquid-vapor interface, and this increases with the system temperature.

2.3 Interfacial Tension

In early nineteenth century, the only force that mankind was undoubtedly sure about was the force that governs the celestial motions - the Newtonian gravity. Yet, observations of phenomena such as the wetting of solids by liquids and the condensation of vapors into liquids posed intriguing questions about the existence of forces potentially surpassing the strength of gravity on a different scale, according to Laplace, these forces were 'insensible at sensible distances' (Rowlinson and Widom, 2013). As our understanding progressed, this 'insensible' forces were latter understood as the 'intermolecular and surface' forces.

The foundational efforts to elucidate the nature of interfaces – the deformable boundaries delineating two equilibrium phases – trace back to the early 19^{th} cen-

tury, marked by the seminal contributions of Young and Laplace. But one can trace even further back[†],

> *His (Isaac Newton's) observations of the colors of thin films (were) the origin of the next great theoretical advance, which had to await, over a hundred years, the coming of Thomas Young. - Albert Einstein*

Young and Laplace's works independently advanced a mechanical framework for understanding interfaces, posing surface tension as a direct manifestation of the anisotropy in pressure attributable to intermolecular attractive forces (Antonin et al., 2011). The Young-Laplace equation establishes a quantitative relationship between the surface tension, γ, of a liquid droplet and the differential pressure, ΔP, across the liquid and vapor phases (Fig. 2.1), expressed as:

$$\Delta P = \gamma \left(\frac{1}{R_1} + \frac{1}{R_2} \right) \tag{2.1}$$

where R_1 and R_2 represent the droplet's principal radii of curvature at equilibrium.

Although the Young-Laplace equation is a cornerstone in the advancement of surface science, critically, this equation in its conventional form, does not distinguish between the phases or between bulk properties and interfacial characteristics (Henderson, 1986; Malijevskỳ and Jackson, 2012). This limitation underscores the necessity for refined models that can accurately account for the complexities inherent at the molecular level, particularly for systems characterized by reduced dimensions. A molecular scale representation of a thin liquid film can be seen in Fig. 2.2. The classical mechanical approach to interfaces presupposes a condition of static equilibrium, neglecting the influence of thermal undulations on the surface's behavior. Bolzmann's kinetic theory, introduced in the late 19^{th} century, bridged this gap by correlating temperature with the kinetic energy of molecules in random motion (Boltzmann, 1872). This advancement laid the groundwork for a more nuanced understanding of phase boundaries, moving beyond the concept of a sharply defined interface to the introduction of the Gibbs dividing surface by Gibbs in the early 20^{th} century (Gibbs, 1928). This conceptual tool delineates the coexisting phases into two distinct, uni-

[†]In 'Foreword' to Isaac Newton, Opticks: Or, A Treatise of the Reflections, Refractions, Inflections & Colors of Light. Based on the 4th Ed., London.

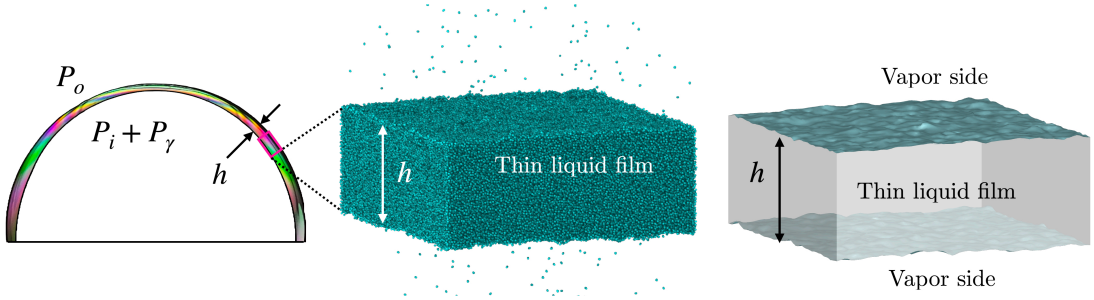


Figure 2.2: Molecular view of a film: the liquid layer of a soap bubble at the left is a macroscopic representation of a film. The central image zooms into a small section within the white rectangle on the bubble, highlighting this region at the molecular scale. The liquid layer coexists with air/vapor outside and inside the bubble. The right image represents the same liquid film, but with the surface molecules visually smoothed to emphasize the continuous surfaces and the corrugations therein.

form subsystems, offering a more sophisticated model of the interface.

The Gibbs dividing surface is identified by its perpendicular orientation to the surface normals across the interface, allowing for an unambiguous definition of normality at any given point. This surface effectively bisects the system (of volume V) into two hypothetical uniform subsystems (of volumes V_α and V_β, where α and β are the two phases), with the choice of surface impacting the volume allocations of the phases, $V_\alpha + V_\beta = V$. However, in contrast to the mechanical treatments, the extensive properties of these phases, such as number density ($N = \rho V$) and internal energy ($U = \phi V$), reveal that:

$$N_\alpha + N_\beta \neq N \text{ and } U_\alpha + U_\beta \neq U$$

Instead, this requires the inclusion of some 'missing' surface contributions (N_s, U_s, etc.) to obtain the total system properties:

$$N_\alpha + N_\beta + N_s = N \text{ and } U_\alpha + U_\beta + U_s = U$$

These adjustments, known as 'surface excess' acknowledge the finite thickness of the interface and the distinct properties inherent to the interfacial region, diverging from

the bulk phases. However, as one zooms in, or, if the system size dramatically decreases where the flat-interface assumption remains no longer valid, it becomes challenging to accurately locate this mathematical plane, i.e., the Gibbs dividing surface (Myers et al., 1999).

The location of the dividing surface, r for a curved interface, or a sphere, is related to the surface tension through the Young-Laplace equation, for simplicity, consider $R_1 = R_2$ in (2.1), i.e., $p_l - p_v = 2\gamma/R$.[‡] where, p_l, p_v are respectively the pressure at the liquid and the vapor side, γ is the surface tension, and R is the mean radius of curvature. A different placement of the dividing surface would require a different γ for the same liquid-vapor system. Tolman (1949) introduced a leading order correction through the introduction of a length, δ, with R termed as the equimolar radius,

$$p_l - p_v = \frac{2\gamma}{R}\left(1 - \frac{\delta}{R} + \mathcal{O}\frac{\delta}{R}^2 \ldots\right) \tag{2.2}$$

The Tolman length, δ separates Gibbs dividing surface from the 'surface of tension' - the surface where surface tension acts. In macroscopic scale, the radius of curvature is large enough to be approximated as a flat interface, and in this limit $\delta \to 0$, therefore any effect of the Tolman length is rendered insignificant. However, as the scale of observation decreases to nanoscale, the separation between the dividing surface and the surface of tension becomes important (Wen et al., 2021).

2.3.1 Forces in films and interfaces

To describe films thinner than few tens of nanometers, intermolecular interaction potential, or the intermolecular forces must be accounted for. These forces are broadly categorized as the short-range (repulsive, act within molecular dimensions, $< 1\,\text{nm}$) and long-range forces (attractive, typically important within $< 100\,\text{nm}$). The short range forces manifest at distances where the electron clouds of interacting particles (atoms, molecules) overlap, whereas, at distances where long range forces act, no appreciable overlap is present.

[‡]In the limit of a flat interface, $p_l - p_v \to 0$, and this dilemma is automatically resolved, as R and γ are no longer related.

The fluctuations in electric dipole moments give rise to one of the most universal long-range forces, i.e., the van der Waals (vdW) interaction, which acts within any combination of molecules and surfaces (Butt and Kappl, 2018; Leckband and Israelachvili, 2001). vdW combines the electrostatic interactions between molecules with permanent dipoles (Keesom interactions, β_{Keesom}), the attractive energy between a dipole in a polar molecule and a induced dipole in a non-polar molecule (Debye interaction, β_{Debye}), and the London dispersion forces, β_{London} which is responsible for the attractive force between non-polar neutral molecules. The vdW interaction can therefore be expressed as:

$$w_{\text{vdw}} = -\frac{1}{r^6}\left(\beta_{\text{Keesom}} + \beta_{\text{Debye}} + \beta_{\text{London}}\right) \tag{2.3}$$

Another major long-range force is the electric double layer force. Unlike van der Waals, which is always attractive between like-molecules or surfaces and thereby facilitate coagulation, electric double layer force between like-molecules is repulsive, hence favors dispersion (when two particles or surfaces with the same charge come close to each other, this leads to repulsive electrostatic forces. Quantum-mechanical short range forces, like steric forces are repulsive too, and determines how close two atoms or molecules can approach each other). The Coulombic or electrostatic interactions are the strongest form of physical interactions, however, these are not the most important interactions in many cases. This is because many systems are charge-neutrals either due to the absence of any charged species, or because the net effect of the system is nullified (Myers et al., 1999). The interplay between the attractive van der Waals forces and the repulsive electrostatic double layer forces make up the DLVO forces which explains the stability of colloidal systems through the competition between coagulation and dispersion - an outcome of the seminal works of Derjaguin, Landau, Verwey, and Overbeek (Leckband and Israelachvili, 2001).

The molecular proximity of the two (liquid-vapor) surfaces of a film may attract or repel each other. If the attractive forces are dominant, they render the film unstable leading to rupture, whereas, repulsive forces stabilize the film (Butt et al., 2023). The attractive potential (gradient of which is the force, i.e., $F = \nabla V$) can be modeled as the inverse of the 6^{th} power of the separation distance between two molecules,

whereas, a good approximation for the repulsive potential is inverse of the distance raised to the 12^{th} power. Combining these two, with the convention that attraction is negative, gives the well known Lennard-Jones 12-6 potential, named after John Edward Lennard-Jones for his remarkable doctoral thesis at Cambridge (Jones, 1924),

$$V_{\mathrm{LJ}} = 4\varepsilon \left[\left(\frac{\sigma}{r}\right)^{12} - \left(\frac{\sigma}{r}\right)^{6} \right] \tag{2.4}$$

Here, ε is the strength of interaction between two particles at a separation distance r, and σ is the characteristic length-scale. 100 years after Lennard-Jones proposed his theory, this potential is still one of the most widely used interatomic potential for its computational efficiency, and its ability in modeling simple systems with physical properties closely matching experimental data (Schwerdtfeger and Wales, 2024).

2.3.2 Statistical mechanical approach

The macroscopic theories leave unanswered the crucial question of how atomistic interactions influence macroscopic thermodynamic properties. Therefore, it becomes imperative to refine our understanding of bulk density to encompass the highly structured density profiles characteristic to an interface. In this context, the statistical approach becomes indispensable as it allows for an examination of the aggregate effects of molecular interactions and fluctuations, that are significant at nanoscales - where phenomena such as molecular orientations and distributions at interfaces become critical to the system's behavior. Furthermore, statistical mechanics provides a bridge between the microscopic molecular dynamics and the macroscopic observable properties, offering a framework to derive thermodynamic quantities directly from molecular properties. In homogeneous equilibrium systems, conventionally pressure is defined as the average force per unit area, and this scalar pressure is equal in all direction. But in general, e.g., in non-equilibrium systems and for systems that are inhomogeneous in nature, the scalar concept of pressure needs to be replaced with a second-order pressure tensor which varies in directions of both the forces and the surfaces the forces act on (Malijevskỳ and Jackson, 2012; Shi et al., 2023).

The statistical approach introduces several methods for calculating surface tension, including the mechanical and thermodynamic routes (Ghoufi et al., 2008; Gloor

et al., 2005; Ibergay et al., 2007). Advances in molecular dynamics simulations, density functional theory, and Monte Carlo simulations have equipped researchers with powerful tools to apply these methodologies in probing the molecular intricacies of interfaces (Rowlinson and Widom, 2013). Following discussions focus exclusively on the mechanical route, aiming to elucidate the atomistic underpinnings that govern macroscopic interfacial phenomena.

The mechanical route: Among various available MD techniques, the mechanical route to the surface tension measurement has gained popularity for its relative simplicity and accuracy. This method replaces the scalar pressure with a second-rank pressure tensor (Walton et al., 1983) and thereby, gives access to the atomic/molecular level detail of the interfacial region through the microscopic definition of the pressure. Following the Irving and Kirkwood (1950a) definition, the diagonal elements of the pressure tensor can be expressed as:

$$\boldsymbol{P}(\boldsymbol{x},t) = \sum_{i=1}^{N} \frac{\boldsymbol{p}_i \boldsymbol{p}_i}{m_i} \delta(\boldsymbol{x}_i - \boldsymbol{x}) + \frac{1}{2} \sum_{i,j}^{N} \boldsymbol{f}_{ij} \boldsymbol{x}_{ij} O_{ij} \delta(\boldsymbol{x}_i - \boldsymbol{x}) \tag{2.5}$$

where, the momentum $\boldsymbol{p_i} = m_i(\dot{\boldsymbol{x}}_i - u)$, $\dot{\boldsymbol{x}}$ is the total particle velocity and u is its streaming part, $\delta(\dots)$ is the Dirac delta function, O_{ij} is the Irving Kirkwood operator (Todd et al., 1995), $\boldsymbol{f}_{ij}$ is the force exerted by atom j on atom i, and $\boldsymbol{x}_{ij} = \boldsymbol{x}_i - \boldsymbol{x}_j$ is the central distance between the two interacting atoms. The average values of the off-diagonal elements in the pressure tensor are zero due to the axial symmetry about the normal direction and the translational symmetry about the plane parallel to the interface. The first term in the right hand side of eq. 2.5 is the kinetic contribution of the pressure tensor, $P^{\text{kin.}}$. The second term denotes the configurational contribution, $P^{\text{config.}}$. The kinetic pressure term corresponds to the ideal gas contribution in an equilibrium system. For a perfect gas in equilibrium, and in the absence of external forces, the interatomic (or, intermolecular) forces are negligible, and the kinetic contribution is dominant. On the other hand, for very low temperature systems or condensed phases, kinetic energy is low enough and the configurational contribution dominates the pressure tensor With the normal (P_N) and the tangential (P_T) components of the pressure, surface tension can be obtained from

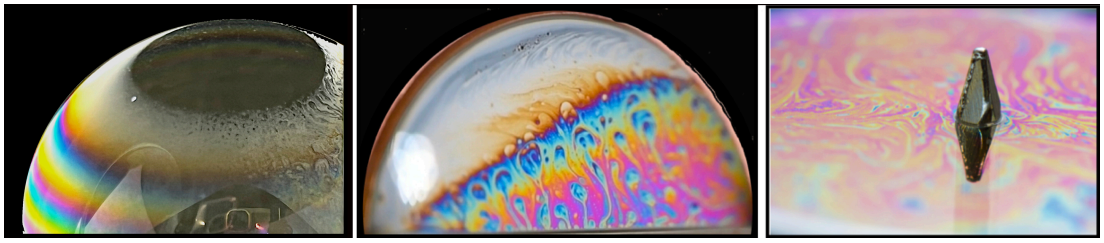


Figure 2.3: A bursting soap bubble (left), interference patterns indicate variation of the film thickness. A planar film (center) shows Marangoni flow due to surface tension gradients. A planar film (right) demonstrates its resilience by withstanding the penetration from a nail.

the Hulshof integral, (Hulshof, 1901) as in Eq. (2.6):

$$\gamma = \int_{-\infty}^{\infty} [P_N(x) - P_T(x)]\, dx. \tag{2.6}$$

Mechanical stability of the interface requires the normal component of the pressure tensor to be uniform and constant throughout the bulk phases and at the interface. On the contrary, the tangential component strongly depends on the position vector in the neighbourhood of the interface; and only at a location far from the interface, this becomes uniform and equal to the normal component. Although Eq. (2.6) requires integration over the entire domain of the two-phase system, the term inside the integration soon becomes zero as one moves a few atomic/molecular diameters away from the interface.

2.4 Stability and Rupture of Thin Films

The stability and rupture of thin liquid films is a captivating spectacle of physics, Fig. 2.3 illustrates a mere fraction of this display [§]. A bubble may bursts in a fraction of a second, and sometimes it can last for hours - even upon the application of a perturbation, bubbles show the unique ability to heal (Courbin and Stone, 2006; Yang and Stone, 2020). These underscore the delicate balance that governs the persistence

[§]A Gallery that follows Chapter 2, includes few more displays of films and bubbles. The experiments generating these images were carried out in order to achieve a first hand realization of the thin-film dynamics which provoked multitudes of ideas for the simulations reported in this thesis, as well as future ideas.

and rupture of such films.

The literature concerning the stability and rupture of thin liquid films is voluminous - encompassing theoretical (Derjaguin and Prokhorov, 1981; Kashchiev and Exerowa, 1980; Saulnier et al., 2002; Scheludko, 1962; Vaynblat et al., 2001), experimental (Casteletto et al., 2003; Evers et al., 1996a; Nikolova and Exerowa, 1999), and numerical (Bresme and Faraudo, 2004; Gamba et al., 1992; Jang and Goddard, 2006; Shen et al., 2013; Tarazona et al., 2012b) investigations. The rupture process, in general, is associated with an activation energy of $\mathcal{O}(\gamma h^2)$ (De Vries, 1958), where h and γ denote, respectively, the thickness and the surface tension of a film. Although this renders this mechanism improbable for thick films (Vrij, 1966a), the probability of rupture increases as thickness decreases, and becomes most significant for films thinner than *ca.* 10 nm. The spontaneity in the rupture process is mostly triggered by the growth of fluctuations, and corrugations of the surface due to thermal motion that weakens the film leading to rupture. These undulations assume increasing importance as thickness decreases and reduce the critical wavelength causing rupture, as highlighted by the molecular dynamics investigation of Zhang et al. (2019).

In addition to the continuous distortion of the liquid-vapor interface due to thermal fluctuations (Langevin, 2020), a slight (local) gradient in surface tension immobilizes the interface (Yaminsky et al., 2010) inducing fluid movement, though it tends to be overlooked in the majority of the theoretical models. The considerations of uniform thickness and a stationary interface, as in the study of Derjaguin and Prokhorov (1981), result in a rupture thickness within the range of a few hundred nanometers. In contrast, Anderson et al. (2010) conducted a linear stability analysis of thinning films, showing that rupture actually occurs when the film thins down to a few tens of nanometers. Yet, the linear theories cannot follow the film evolution until rupture since their validity ceases as the disturbances in the film grows sufficiently. Inclusion of the non-linear terms showed that any local thinning of a free standing film amplifies the influence of the long-range force, and accelerates film rupture (Erneux and Davis, 1993; Prévost and Gallez, 1986) while simultaneously attenuating the effects of surface tension (Williams and Davis, 1982). The importance of relaxing the linear approximations in the film stability and rupture studies is further realized by the

fact that the non-linear theory yields significantly shorter time of rupture from those obtained through the linear models, as much as an order of magnitude (Williams and Davis, 1982).

While an impressive body of literature outlines the complexities of rupture dynamics for free standing non-draining films - which are of significance for numerous colloidal systems, from coalescence of emulsions to fusion of lipid bi-layers, and for biological membranes (Knutton, 1979; Sheludko, 1967) − the crucial role, as well as the ambiguities of the contact line properties in rupture behavior for supported films are also underscored. A method that sidesteps these ambiguities involves eliminating the solid-substrate (Forrest et al., 1996; Ge et al., 2000). Replacing the solid with a liquid substrate cures any contact line singularity at the interface, and exhibits distinct dewetting behavior (Shiri et al., 2023). Regardless, it introduces a nuanced dependency on the properties of the liquid-liquid interface. An unbounded film (as in foams and bubbles), in this context, removes interference from any substrate, whether liquid or solid, and thereby can serve as a reference point of rupture dynamics. The presence of two free surfaces, the undulations therein, and the complexity which predominantly resides in the spatio-temporal dynamics of the liquid-vapor surface contributed to the lack of clarity in the understanding of the origin, and the unfolding of the rupture process. *Chapter 4* investigates the spontaneous rupture of thin free films and carefully examines the associated molecular details.

2.5 Thin Film Retraction: Taylor-Culick Theory

Once rupture is initiated, subsequent growth (as in Fig. 2.4) leads to complete collapse of the film. This is termed as the film retraction process, and has been under scrutiny for almost a century. Despite this, it remains an active area of debate to date. In their pioneering works, Taylor (1959) and Culick (1960) independently derived an equation for film retraction by considering that the growth of a nucleated hole of radius, R − see Fig. 2.4 − is driven purely by the balance between the surface force, F_γ, and the inertia of the liquid mass, m, collected in a rim surrounding the hole, i.e., $F_\gamma = \frac{d}{dt}(m\dot{R})$. Applying the initial condition at (time) $t = 0$, $R = 0$ for finite $\dot{R}$, one

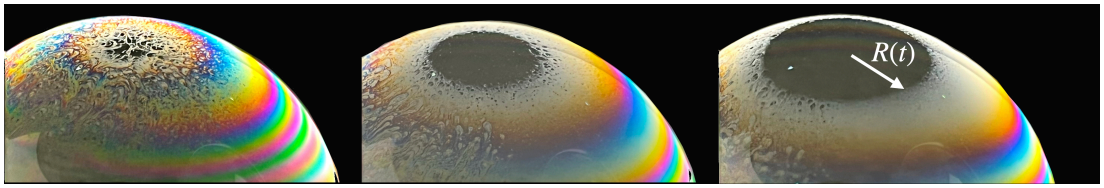


Figure 2.4: A bubble collapsing over time. The rupture generally starts at the apex, which is the thinnest part of the bubble. The rupture site grows, arguably at the Taylor-Culick retraction rate, leading to the complete collapse of the liquid layer.

obtains, upon integration, the Taylor-Culick (TC) speed,

$$U_{\mathrm{TC}} = \sqrt{\phi\gamma/\rho h_0} \tag{2.7}$$

where, h_0 is the thickness of the unperturbed part of the film with density ρ and surface tension γ. In the works of Culick (1960); Taylor (1959), $\phi = 2$. This surprisingly simple and elegant equation captures the overall retraction dynamics, and corrects Dupre's inappropriate energy balance assumption (Dupré, 1869). However, its accuracy is debatable, and it markedly deviates for thinner films (Evers et al., 1996b, 1997; Florence and Mysels, 1974; Lohse and Villermaux, 2020; McEntee and Mysels, 1969; Pierson et al., 2020; Planchette et al., 2019). Among these studies, the seminal work of McEntee and Mysels (1969) conclusively demonstrates that for films thinner than 100 nm, the growth rate of an expanding hole is distinctly slower than the theoretical prediction. The authors convincingly showed that $\phi << 2$ to have reasonable agreements with observations for thinner films.

Taylor's resolution is based on a few key assumptions, (i) when rupture propagates, h_0 remains uniform except at the rim, and (ii) all liquid-mass of the expanding hole is collected inside the rim, i.e., $m = \rho\pi R^2 h_0$. In a more formal derivation, Culick made the assumptions of uniform thickness and constant surface tension everywhere. Whilst the assumptions leading to Eq. (2.7) are not incorrect at the global scale, their local deviations become increasingly important as thickness decreases down to nanometers. A range of continuum based models attempted to explain film rupture process by consideration of the non-uniformity of film thickness (Keller, 1983), surface elasticity

(Petit et al., 2015), surface tension gradients (De Corato et al., 2022), Marangoni stresses (Constante-Amores et al., 2022) and viscous effects (Deka and Pierson, 2020a; Gordillo et al., 2011; Pierson et al., 2020; Savva and Bush, 2009). With continuum models, any additional physics must be included by adding another conservation or balance law - which might add another layer of obscurity. *Chapter 5* reports an MD investigation, aimed to understand the molecular mechanisms responsible for the differences in behaviors observed in the retraction of thin films.

2.6 Transport of Surfactant along the Surface

The understanding of thin films, and the dynamics therein, motivated the consideration of surfactants along the surface of a thin film. Surfactant laden films are ubiquitous in myriad natural processes, and in industrial applications (indeed, pure films, although central to fundamental understanding, are impossible to find in practice). As such, literature concerning surfactants is voluminous. Surprisingly, the transport of surfactant along the deforming liquid-vapor interface of thin films remained overlooked, specially by the molecular dynamics community. In the penultimate chapter of this thesis, *Chapter 6*, the transport mechanism of surfactant monolayer along the deforming surface of a thin water film is investigated.

A Murder Mystery (Nature, 22, 1880)

In the autumn of 1878 a man committed a terrible crime in Somerset, which was for some time involved in deep mystery. His wife disappeared suddenly and entirely from sight. Suspicion immediately fell upon the husband, a clever young fellow of about thirty, but no trace of the missing woman was left behind, and there seemed a strong probability that the crime would remain undetected. A week after the woman had disappeared, some Somerville boatmen looking out towards the sea, were struck by observing in the Long Bay Channel, the surface of which was ruffled by a slight breeze, a streak of calm such as, to use their own illustration, a cask of oil usually diffuses around it when in the water. The feverish anxiety about the missing woman suggested some strange connection between this singular calm and the mode of her disappearance. Two or three days after her brother and three other men went out to the spot where it was observed, and from which it had not disappeared, and with a series of fish-hooks ranged along a long line dragged the bottom of the channel, ... with water glasses the men discovered that it had caught in a skeleton which was held down by some heavy weight. ... From the minute fragments remaining, and the terrible stench, had evidently not lain long in the water. The husband was a fisherman, and Long Bay Channel was a favourite fishing ground, and he calculated, truly enough, that the fish would very soon destroy all means of identification; but it never entered into his head that as they did so their ravages, combined with the process of decomposition, set free the matter which was to write the traces of his crime on the surface of the water. ... The husband was found guilty and executed.[a]

[a]Abridged version, adapted from Bush JW. Interfacial phenomena, MIT OCW. 2013;18:80.

Though not anticipated by the fisherman in Somerset, nor by the then investigating officers, the ability of surfactants in calming down a water body has been known to scientists from even before. The formal understanding can be traced back to 18^{th} century when Benjamin Franklin, inspired by an incidental observation at sea, began to investigate the effect of oil on water. Franklin noted that upon the discharge of oily kitchen waste from a ship, the surrounding sea water displayed a notably calm wake compared to other ships. His ensuing experiments revealed that even minimal quantities of oil could spread rapidly across the water surface, forming an extremely thin layer that effectively dampened surface ripples.

In 1757, being at sea in a fleet, I observed the wake of two of the ships to be

remarkably smooth, while all the others were ruffled by the wind.[¶].

Building on Franklin's observations, systematic experiments were conducted by Lord Rayleigh in 1890, which quantified the spreading of olive oil on water. Rayleigh reported that a mass of 0.81 mg of olive oil could uniformly cover an area of 555 square cm, implying a film thickness of approximately 16 Angstroms. This finding was contemporaneously corroborated by Agnes Pockels, a self-taught German scientist, who independently derived a similar thickness of 13 Angstroms through her own experiments conducted in a domestic setting[‖]. Approximately two decades later, Irving Langmuir further investigated these phenomena, confirming the monolayer thickness and linking it directly to the molecular dimensions of the substances involved. Langmuir's work, which eventually earned him a Nobel Prize, fundamentally advanced our understanding of molecular films at interfaces, known as Langmuir monolayers.

Fast forward to modern times, surfactant dynamics at the liquid-vapor interface represents a critical area of study with widespread implications across various disciplines, including engineering and medicine. This is underscored by a significant body of research highlighting its importance in processes ranging from respiration to solar energy applications (Erinin et al., 2023; Leenaars et al., 1990; Morciano et al., 2020; O'Brien, 1996; Possmayer et al., 2023; Stetten et al., 2018). Surfactants, by virtue of their amphiphilic structure, play a pivotal role in modulating interfacial dynamics. These molecules align at the interface orienting their hydrophilic heads toward, and hydrophobic tails away from the aqueous phase, and forms a monolayer. This monolayer, adsorbed at the interface, breaks the otherwise strong interaction between the liquid molecules, and reduce the net cohesive force at the surface, thereby lowers the surface tension.

The spread of the surfactant layer across the liquid-vapor interface, and subsequent reorganization and reorientation, lead to gradients in concentration, resulting in differential surface tensions. Such gradients foster the development of Marangoni stresses (Scriven and Sternling, 1960a), a phenomenon that drives surfactant molecules from

[¶]Benjamin Franklin, Philos. Trans. R. Soc. London 64, 445–460

[‖]Despite significant contributions to the field, Agnes Pockels did not receive formal recognition in her lifetime, highlighting the challenges faced by women in science during that era.

regions of low to high tension, thus influencing the fluid flow in complex ways (Basu and Gianchandani, 2007; Benouaguef et al., 2021; Bickel, 2019; Kitahata and Yoshinaga, 2018; Roché et al., 2014; Trittel et al., 2019). The dynamics of surfactant transport are complicated by several factors, including surface convection, and the diffusion of surfactants both at the interface and in the bulk. These mechanisms contribute to the redistribution of surfactants, thereby challenging simplistic analytical models that often rely on reductive assumptions.

Empirical observations, such as the findings of Benouaguef et al. (2021) using particle image velocimetry, reveal the complexity of soluto-capillary flows, underscoring the limitations of analytical approaches in capturing the intricacies of surfactant-driven fluid motion. The process of the lateral migration of surfactant molecules across the liquid-vapor interface displays the formation of a precursor film that alters surface tension in its path - an observation exemplifying the complex nature of surfactant dynamics (Afsar-Siddiqui et al., 2003). Such spreading is characterized by a power-law relationship, $L(t) \sim kt^n$, where k is the spreading coefficient, and $L(t)$ denotes the extent of spreading, indicating a transition in the dominant spreading mechanism as reflected by variations in the exponent's (n) value. The fundamental barrier in gaining experimental insights is the challenge in tracking surface properties without altering them. This presents a substantial obstacle in analyzing the underlying dynamics. It is due to these inherent challenges in isolating the myriad factors at play, surfactants are referred to as 'hidden variables' (Manikantan and Squires, 2020).

On the analytical side, significant strides have been made in elucidating surfactant transport through the contributions of Stone (1990), Bickel and Detcheverry (2022); Crowdy (2021); Crowdy et al. (2023); Gaver and Grotberg (1990), among others. In particular, Stone (1990) derived a simple yet robust convection-diffusion equation to describe the transport of surfactant along a deforming liquid-vapor interface (in section 6.4, we will describe this in greater details). Gaver and Grotberg (1990) investigated the time dependent flow behavior induced by the presence of contaminant on a thin film, and found that the initial distribution of surface tension, which directly depends on the surfactant concentration, dictates the dynamical system. Recent works of Crowdy (2021) showed that surfactant spreading can be effectively modeled

through the complex Burgers' equation. This work has been further expanded upon through the development of exact solutions (Bickel and Detcheverry, 2022; Crowdy et al., 2023). However, the specificity of these solutions constrains their applicability, limiting the broader understanding of the underlying physical principles (Temprano-Coleto and Stone, 2024).

To the best of the author's knowledge, there is a surprising absence in the MD literature concerning the lateral transport mechanism of surfactant molecules along a deforming liquid-vapor interface. This is a gap which *Chapter 6* aims to fill by modeling the transport of surfactants (SDS) on the liquid-vapor surface of a thin water film by employing non-equilibrium molecular dynamics simulations (NEMD). By transitioning from simplified Lennard-Jones particles to more intricate water-surfactant systems, we confront the challenge of accurately modeling the interactions within these molecules. This necessitates a careful approach to the force-fields employed, ensuring they capture the nuanced behaviors of real-world systems. To accommodate the complexity and scale of these interactions over extended periods, a coarse-grained modeling approach is employed. This method simplifies the detailed atomic interactions into more manageable representations, allowing for the simulation of long-term dynamical behaviors without sacrificing critical accuracy in depicting interfacial phenomena. The inspiration behind this study is deeply rooted in the complex and interconnected physical processes these systems exhibit, which are still not fully understood − neither at macroscopic scale, let alone at the molecular scale. Discussions that follow, give a concise overview of the historical development of our understanding of surfactants and their effects, progressing to a review of contemporary literature on transport mechanisms. An objective of this study is to establish the extent to which the continuum transport equation can model the redistribution of surfactant distributions on the surface, and their consequences.

2.7 Overview

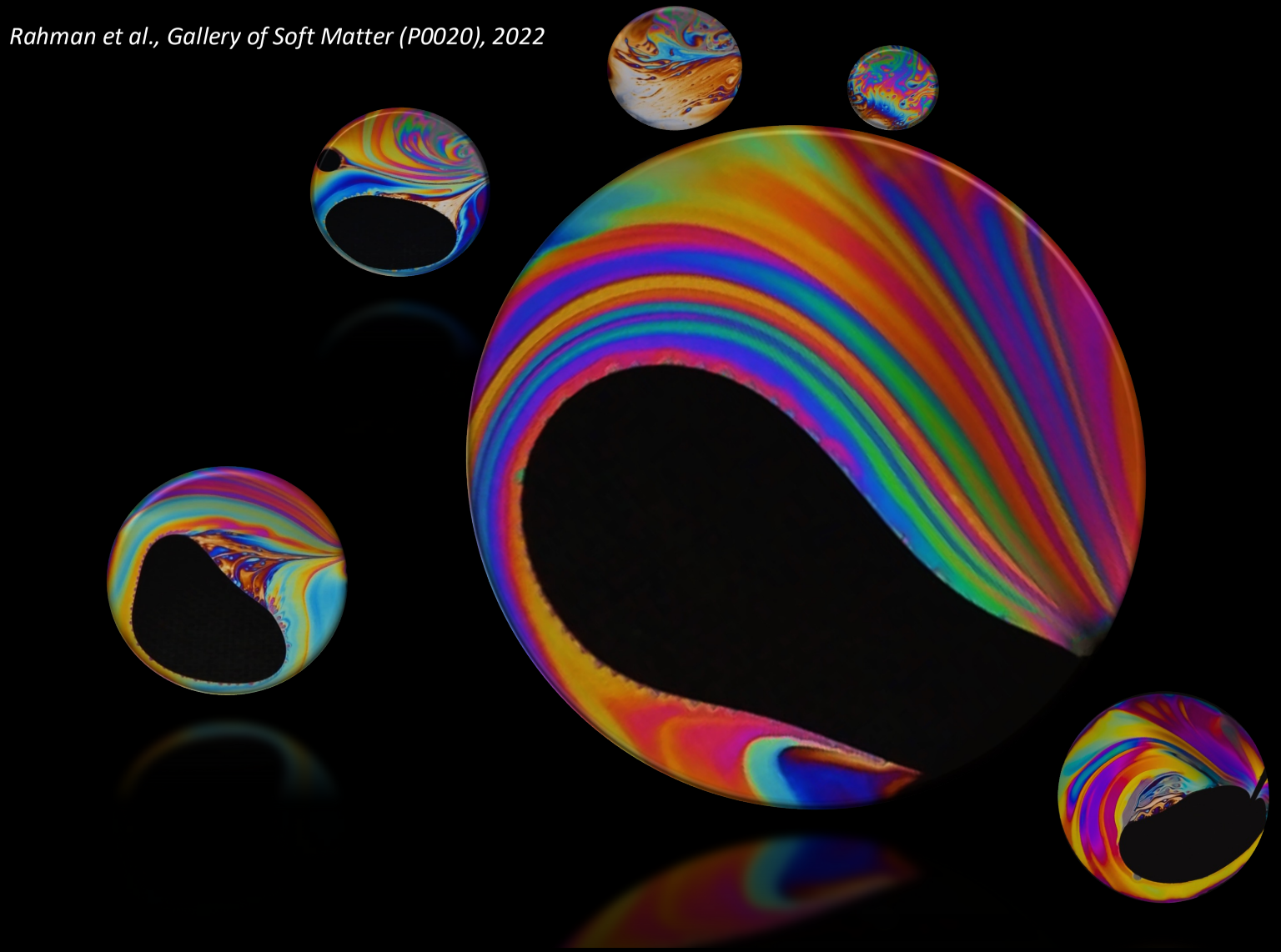
This chapter summarizes the critical importance and challenges associated with thin films, offering brief historical anecdotes of scientific advancements as well as outstanding questions that, if resolved, could potentially advance the field. An interim *Gallery*

of films and bubbles follows, featuring their vibrant display of colors. Although free from complex scientific terminology, they still evoke the rich, intertwined physical mechanisms that underpin these phenomena. In *Chapter 3* the mechanisms through which the surface tension of a liquid-vapor interface is modified with varying temperature is explored. A new perspective to the surface is coined, namely 'percolating stress-network' which might derive useful insights on the interface. *Chapter 4* portrays the life-span of a thin film - from the formation of nuclei, or the rupture sites, through the stages of their evolution leading to the ultimate collapse of the film. The work presented in this chapter reveals the existence of a window of fluid memory containing the footprints of a future rupture event. *Chapter 5* carefully isolates a single rupture event at its molecular origin, and compares the classical theory of rupture. Findings reveal why the celebrated Taylor-Culick theory of rupture fails at the nanoscale, necessary corrections are proposed. *Chapter 6* focuses on more pragmatic considerations. The role of surfactants in modifying the properties of thin films has been well recognized but not comprehensively understood. The transport of surfactant molecules along the deforming surfaces of thin films present a complex interplay of forces, often described by the continuum advection-diffusion model. However, transport phenomena below the continuum scale has been remained unexplored. Chapter 6 investigates the transport mechanism of surfactants on a thin water-film, and aims to bridge the gap between molecular-scale transport and the continuum model. Finally, *Chapter 7* concludes this thesis highlighting the key findings from this research, their potential contributions and possible improvements, along with few ideas for future works.

This page intentionally left blank.

Gallery: Lights and Colors

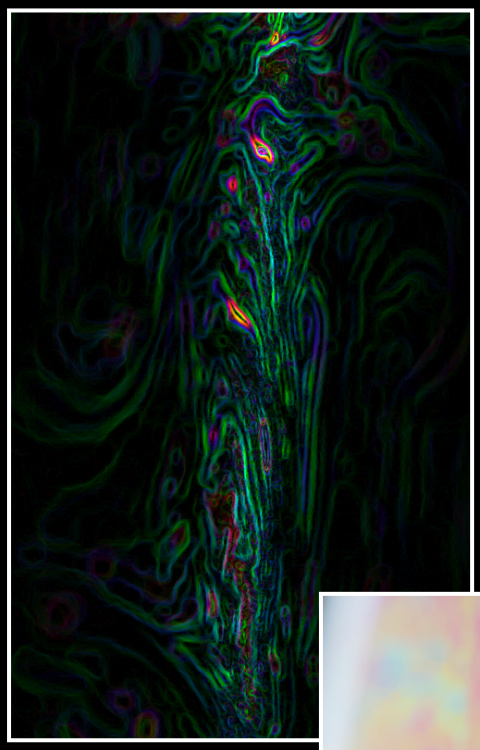
There is an art to science, and science in art; the two are not enemies, but different aspects of the whole.
-Isaac Asimov

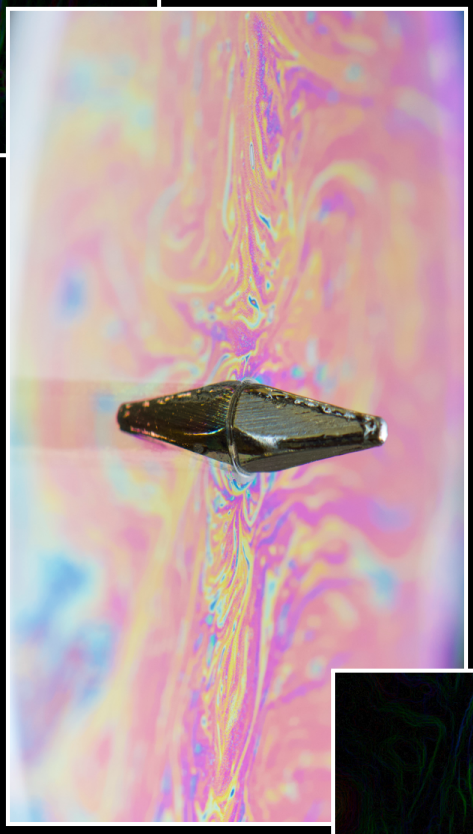


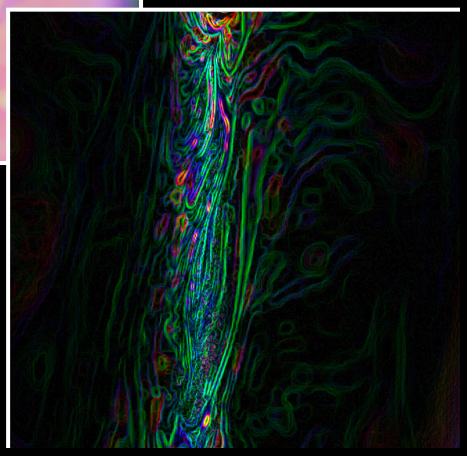
Rahman et al., Gallery of Soft Matter (P0020), 2022

G1

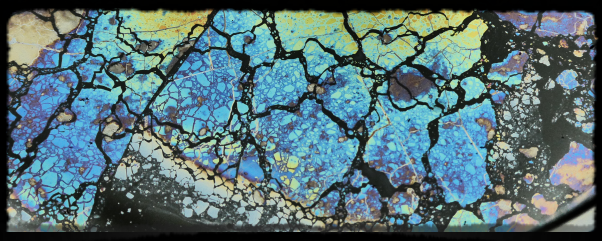
G2

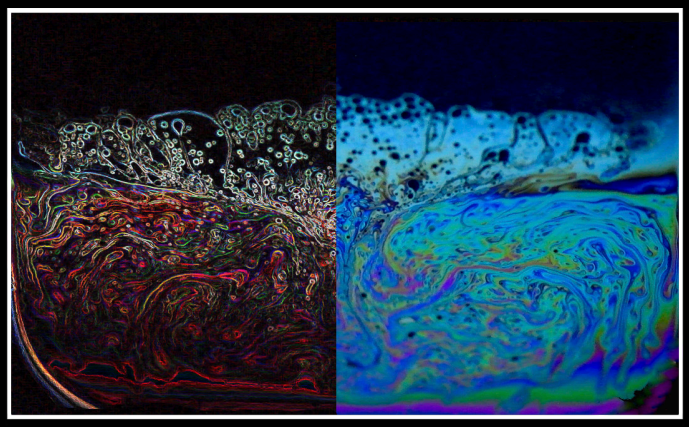


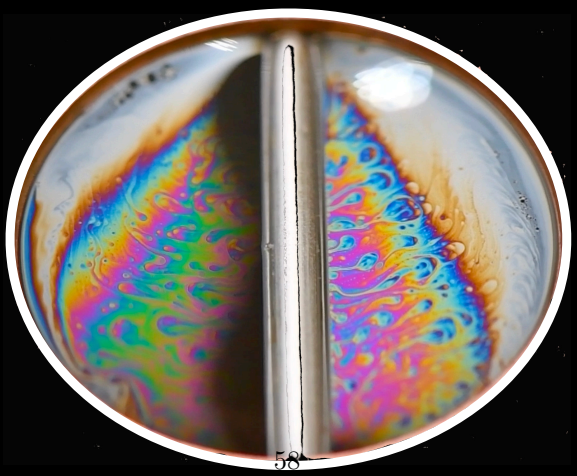




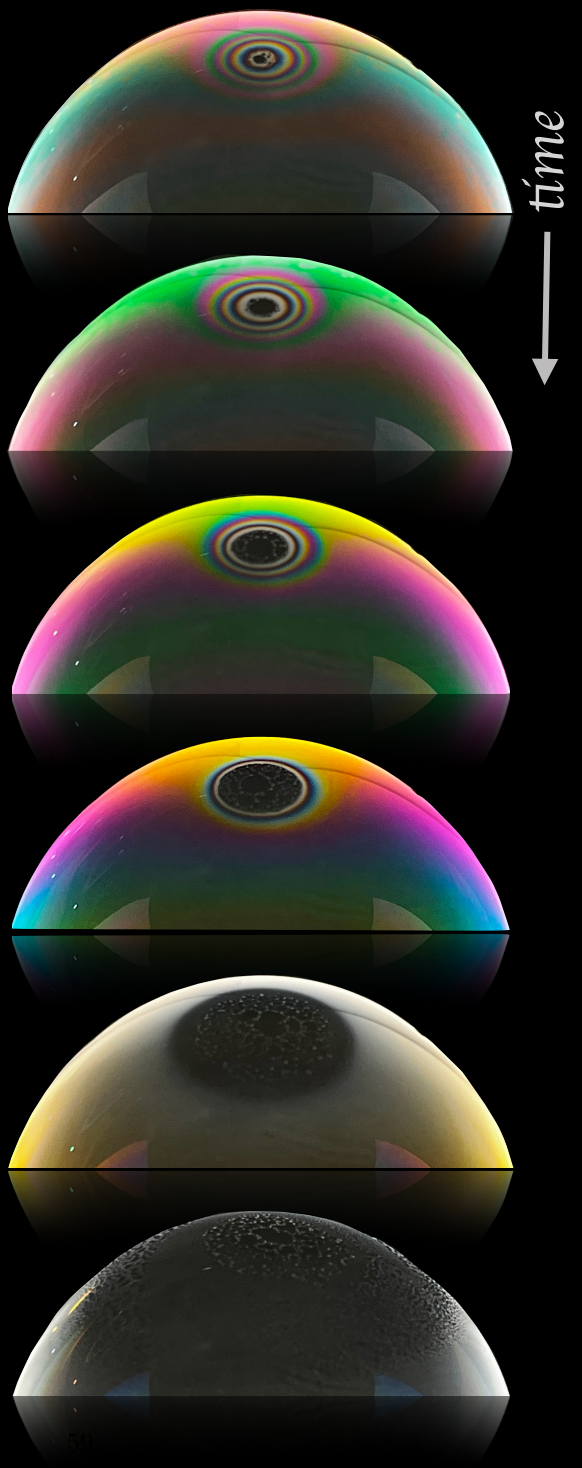
G3



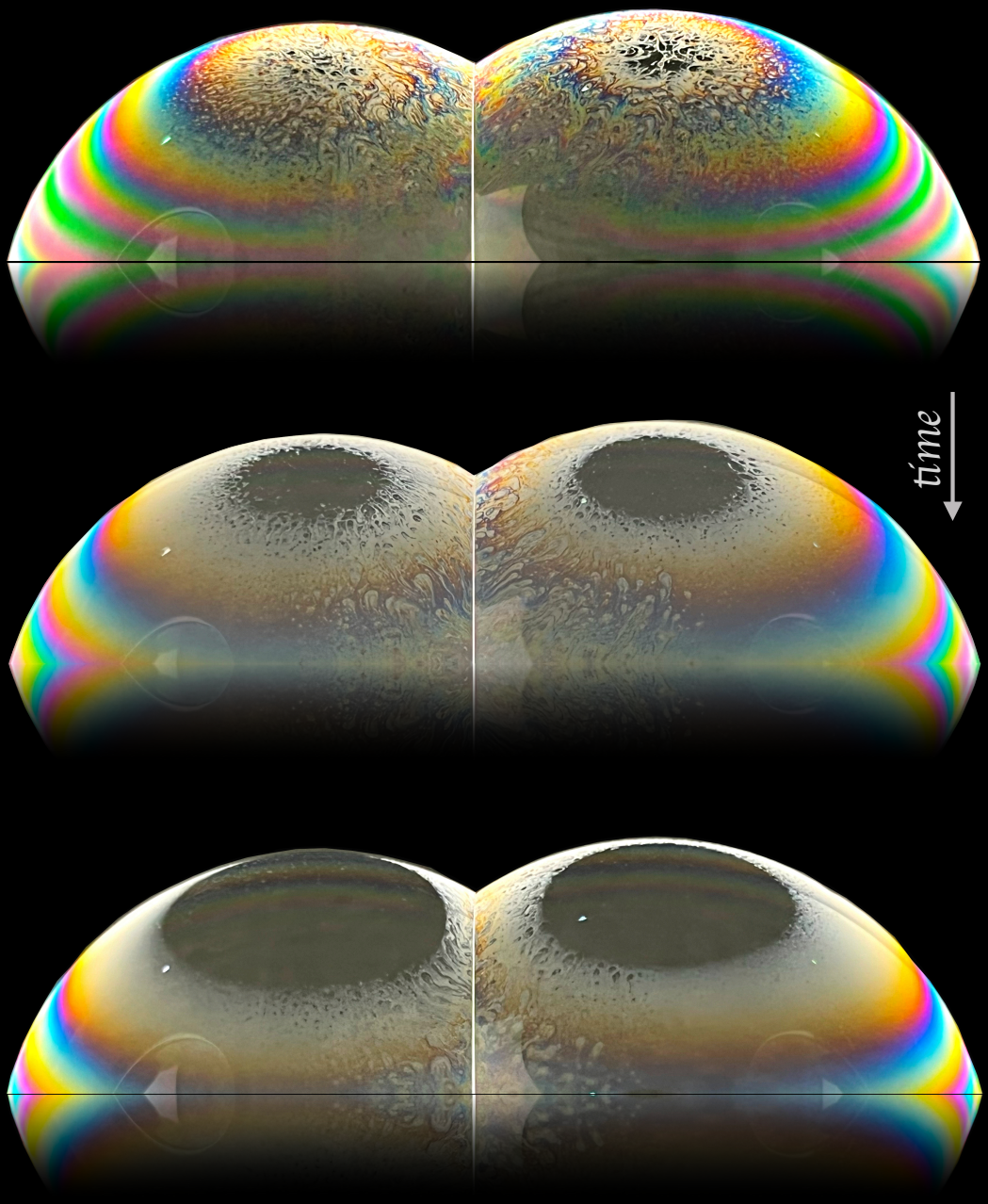




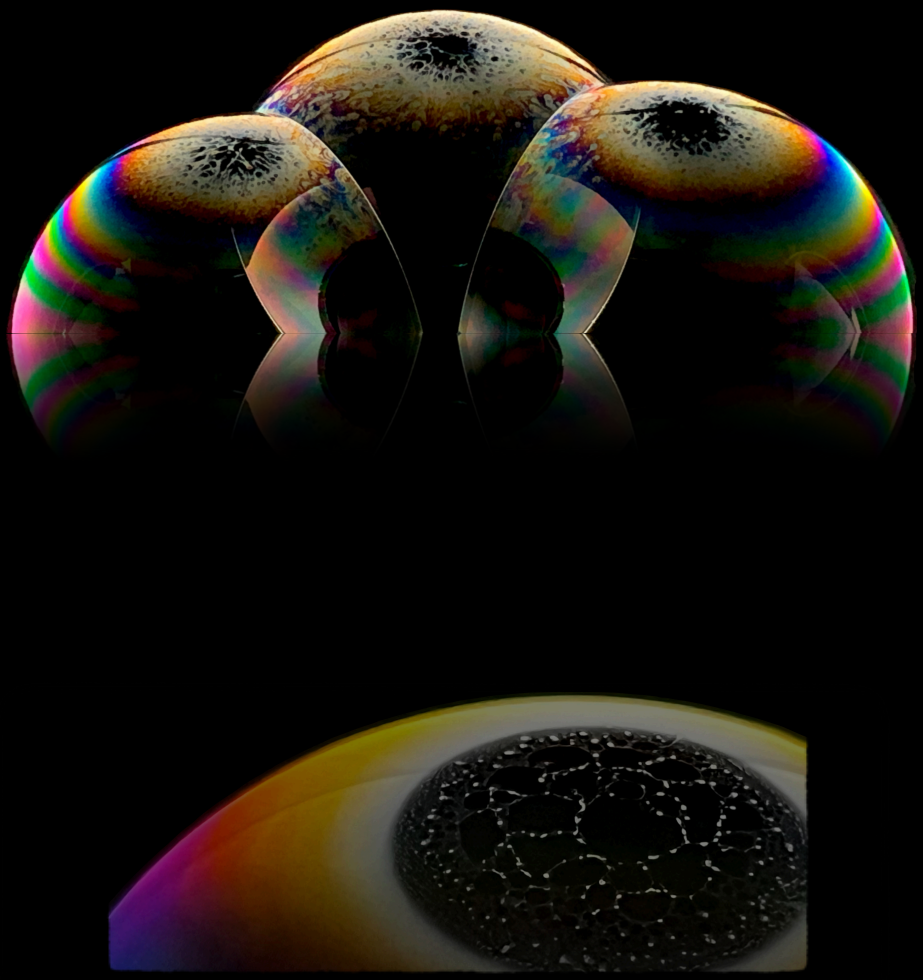
G4



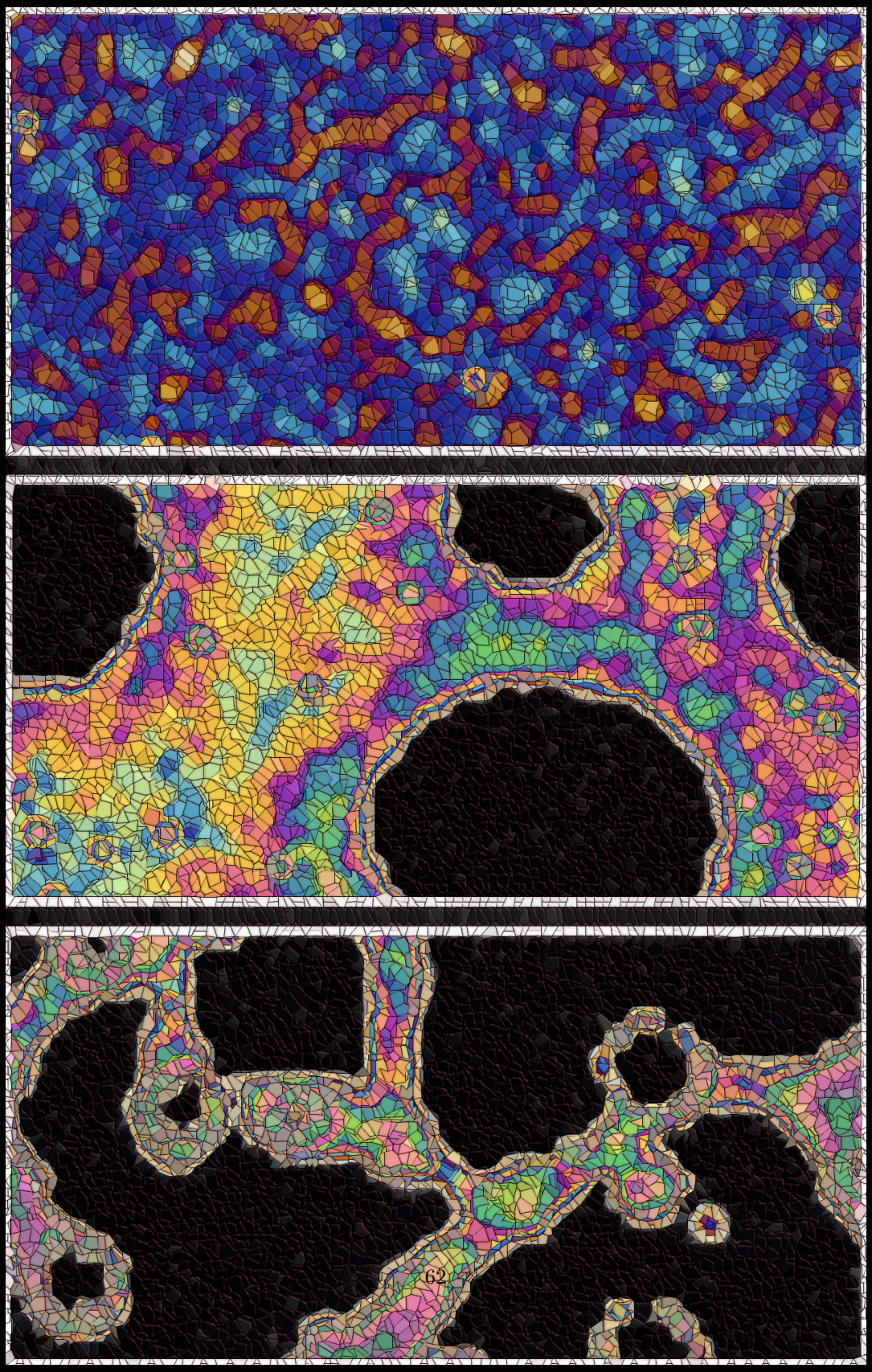
G5



G6



G7



Echoes of Imagery

**

Beyond the bounds of traditional metrics, the images of this *Gallery* weave a visual narrative of the subtle dance of physics within a whisper-thin veil of liquid††. The images G1-G6 are taken using rudimentary instruments, and imaging setup. The reason behind these 'artworks' is the appreciation of the intricate physics in the otherwise simple systems. However these have not been used to draw any of the conclusions outlined in this thesis. G7 is from molecular simulations, rendered and smoothed.

G1: A thin film in a metal ring is subjected to concentrated heating from below. The thermal singularity repels liquid away, the presence of surfactants and their continuous redistribution induces Marangoni convection. The competition drives the motion, and also the growth of a black film.

G2: A surfactant laden thin film is pierced through by a nail. The colorful display is due to interference patterns, surfactant renders the film stable enough to withstand the piercing.

G3: (Top) An island of thin films in an abandoned tea-cup. (Center) A rather violent flow field in a vertical liquid-screen, black film formation at top of the film. Left half with edge detection filter applied, right half - unfiltered. (Bottom) Marangoni regeneration in heated films. A wire is attached along the diameter of a ring, and then the ring is immersed in soapy-water. This forms thin films at both sides of the wire. Later, current is applied to heat the wire which induces thermo-capillary flow

**The motivation to include this gallery comes from Edward R. Smith, and Li Shen, who posses a true sense of art in science.

††These images are smoothed, enhanced, and filtered for aesthetic purposes, and should not be directly used for quantitative analysis.

in a soluto-capillary flow field.

G4: A bubble going through stages of its life (only upper half is captured). Interference patterns showing the spatial variations of thickness, and the expansion of rupture sites. The ring-like structures around these sites give evidence of surface undulations in the proximal region of the weakest part of the film, far from this region, surface undulations are rather less prominent.

G5: Two attached bubbles going through simultaneous rupture. One can identify, at the contact line, mass transfer from one to the other bubble.

G6: (Top) Three attached bubbles - all at at their early stages of rupture. (Bottom) Zoomed view of the growing nucleus, white dots-like fragmented liquid droplets are visible within the black region.

G7: Molecular dynamics simulations showing the life of a thin film - undulation, formation of voids and their expansion, and finally fragmentation.

Nature uses only the longest threads to weave her patterns, so that each small piece of her fabric reveals the organization of the entire tapestry.

Richard Feynman

3

Surface Structure: The Intrinsic Interface

The evolution of the liquid-vapor interface of a Lennard-Jones fluid is examined with molecular dynamics simulations using the intrinsic sampling method. Results suggest clear damping of the intrinsic profiles with increasing temperature. Investigating the surface stress distribution, linear variations of the space-filling nature (fractal dimension) of the stress-clusters are identified at the intrinsic surface with increasing surface tension, or equivalently, with decreasing temperature. A percolation analysis of these stress networks indicates that the stress field is more disjointed at higher temperatures. This leads to more fragile (or, poorly connected) interfaces which result in a reduction in surface tension*.

*A version of this chapter has been published as: Rahman, M.R., Shen, L., Ewen, J.P., Dini, D. and Smith, E.R., 2022. The Intrinsic Fragility of the Liquid–Vapor Interface: A Stress Network Perspective. Langmuir, 38(15), pp.4669-4679.

Codes to reproduce the data are publicly available at:
https://github.com/MuhammadRRahman/Intrinsic-Interface-and-Fractal-Dimension

3.1 Introduction

Attaining a molecular/atomic description of the interface is challenging due to the inhomogeneous nature of the interface and the difficulties in quantifying the surface forces. The non-uniformity of the particle number density across the interface gives rise to mathematical complexity in uniquely identifying the system and its thermodynamic properties (Malijevskỳ and Jackson, 2012). In the past years, numerous efforts have been made, both experimentally (Kuzmin and Romanov, 1994; Mitrinović et al., 2000) and by computer simulations (Höfling and Dietrich, 2015; Senapati and Berkowitz, 2001; Stephan et al., 2018; Willard and Chandler, 2010) to advance our understanding of the interface. A comprehensive review can be found in Ghoufi et al. (2016) and Ghoufi and Malfreyt (2019).

Most MD simulation studies in the literature focused on the average profiles of the interface where the thermal fluctuation effects obscure the identification of the intrinsic behaviors (Braga et al., 2018; Bresme et al., 2008; Willard and Chandler, 2010). The presence of thermal fluctuations − in the form of capillary waves − blurs the interfacial properties, and makes it extremely difficult to extract the true nature of the interface (Bresme et al., 2008). Therefore, it is necessary to decouple the effects of capillary wave from the surface layer in order to investigate the intrinsic nature of the interface - an idea first introduced by Buff et al. (1965). In their capillary wave theory, Buff et al. (1965) formalized the concept of the existence of an interface $\zeta(y, z, t)$ which acts as an instantaneous atomic border between the two phases. Sides et al. (1999) exploited this idea of decoupling the capillary-wave broadening from the intrinsic interface. However, to achieve a meaningful perspective of the intrinsic interface, adequate care must be taken in selecting the appropriate system size and the transverse resolution to avoid any blurring of the footprints of the intrinsic layer by the capillary wave fluctuations (Chacón et al., 2006). Following its development, the intrinsic sampling method has been applied to understand the interface layer in a number of studies, e.g., to investigate the intrinsic gap between water-oil surface (Bresme et al., 2008) and to define the thickness of an adsorbed liquid film on a substrate (Fernández et al., 2011).

Zooming into the meeting plane of the two co-existing phases, one obtains increasingly higher impact of fluctuations as the system temperature is raised. Given the dependency of the surface fluctuations on temperature, it is surprising that more attention has not been devoted to understand the effect of temperature variation on the intrinsic profiles of the liquid-vapor interface. Not only that temperature modifies the surface properties, often it becomes one of the key driving factors for a number of interfacial events, e.g., thermo-capillary flows (Jasnow and Vinals, 1996). This chapter examines the temperature effects on the intrinsic density and pressure profiles. Afterwards, the concept of fractal dimensions and percolating networks are applied to analyses the temperature dependency of the spatial correlation of the inter-atomic interactions at the surface layer.

3.2 Simulation Details

Open-source Flowmol MD code (Smith, 2013) was used to model the liquid-vapor interface of a Lennard-Jones (LJ) fluid at different temperatures.

$$V_{ij}(r) = 4\varepsilon_{ij}\left[\left(\frac{\sigma_{ij}}{r_{ij}}\right)^{12} - \left(\frac{\sigma_{ij}}{r_{ij}}\right)^{6}\right]$$

here, V_{ij} is the potential between particle i and j located at a distance r_{ij}, and free from electrostatic interactions. The dispersion energy is described by ε_{ij}, and σ_{ij} is the characteristic length scale. Periodic boundary conditions are applied in all three Cartesian directions. The initial simulation domain was a cubic box of dimensions $L_x = 120.64$, $L_y = 19.05$ and $L_z = 19.05$ in reduced LJ units, containing a total of $14,827$ particles. This corresponds to a cubic box of $\sim 40.8\,\text{nm} \times 6.45\,\text{nm} \times 6.45\,\text{nm}$. Unless otherwise specified, throughout this Chapter, all parameters are reported in reduced units. The middle 40% of the box was initialized with LJ particles in liquid phase and the remaining was designated as vapor. The initial state was created from a face-centred cubic (FCC) lattice with a starting density of $\rho = 1$, then molecules were randomly deleted until the pre-set liquid ($\rho = 0.5$) and vapor ($\rho = 0.005$) densities were obtained. Note, these initial units were somewhat arbitrary and used to set up the system only, a sufficient equilibration time was then allowed so the system

tended to the expected coexistence. The equilibration phase was run in the canonical (NVT) ensemble using a Nośe-Hoover thermostat, (Hoover, 1985; Nosé, 1984) for 50,000 time steps with $\Delta T = 0.005$. Periodic boundary condition was applied in all three Cartesian directions and the Verlet (1967) integrator was used to integrate the equations of motion. Appendix C gives a basic overview of the essential ingredients of Molecular Dynamics simulations.

For surface tension calculation, a small cutoff radius, r_c results in significant deviation from experimental data for argon (Nijmeijer et al., 1988), whereas, $r_c \geq 4$ (in reduced units) is found to give better agreement (Smith et al., 2016). Surface tension being one of the prime interests in this study, and as recommended by Ghoufi et al. (2016), $r_c = 4.5$ was used to improve accuracy. Further agreement with experimental data would require a more complex interaction potential, such as those which explicitly include three-body interactions. (Ghoufi et al., 2016) The final state of the initial NVT calculations was taken as an initial condition for production runs in the microcanonical (NVE) ensemble. For each reported case, three independent simulations were carried out to improve the statistics.

3.2.1 Intrinsic Interface

The intrinsic interface was fitted to the outermost layer of the liquid by cluster analysis with the Stillinger cut-off length (Stillinger Jr, 1963), $r_d = 1.5$ (in reduced units), and with the required criterion of each atom having more than three neighbors (Smith and Braga, 2020). Instead of assuming an average interaction contour, the functional form of the interface, $\xi(y, z, t)$ was refitted at every time step using the intrinsic sampling method, ISM, (Chacón and Tarazona, 2003) which approximates the liquid-vapor interface by means of a Fourier series representation as in Eq. (3.1).

$$\xi(y, z, t) = \sum_{\mathbf{k}<k_u} \hat{\xi}_{\mathbf{k}}(t) \, \exp(2\pi i \mathbf{k} \cdot \boldsymbol{r}_{\parallel}) \tag{3.1}$$

Here, $\boldsymbol{k}$ is the wave vector that corresponds to the periodic boundary conditions, i.e., $k = 2\pi(n_y/L_y, n_z/L_z)$ with $n_y, n_z = 0, \pm 1, \pm 2, ...,$ k_u is the modulus of the wave vector, and $\boldsymbol{r}_{\parallel}$ denotes the parallel surface components in y and z directions. The fitted

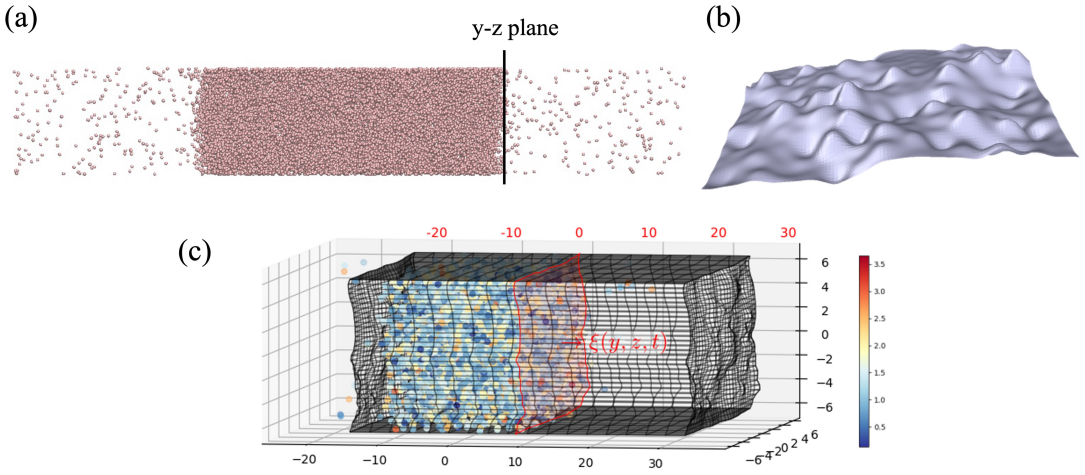


Figure 3.1: (a) Liquid-vapor coexistence (b) fitted liquid-vapor surface function ξ (yz plane) (c) mapped grids at the interface, $x = 0$ (mapped coordinates are in red at the top and un-mapped coordinates are in black at the bottom). The atoms are colored by their respective velocities, the bin-resolution is reduced here for visualization purpose. The mapping shifts every time the interface moves in the x direction.

coefficients, $\hat{\xi}_{\mathbf{k}}$ are expressed as time dependent functions because they are refitted to the surface each time the position of the surface atoms change (i.e. every time step). Fig. 3.1 (a) is representative of the coexisting system, where an intrinsic interface was fitted to the outermost liquid layer, the interface and the fluctuations are illustrated in Fig. 3.1 (b). All results presented hereafter correspond to the interface at the right side of the domain; $x > 0$ corresponds to the vapor side and $x < 0$ corresponds to the liquid side.

With the intrinsic interface to hand, the pressure tensor is obtained from surface fluxes, which can be shown to satisfy the mechanical equilibrium condition, i.e., the normal pressure is constant when moving through the interface (Smith, 2022). This form of pressure also includes a term for the movement of the intrinsic surface itself, which must be accounted for to ensure balance of the coarse-grained equations. The surfaces of a volume are flat in the y and z directions and follow the interface in the

x direction. The surface pressure can be written as the sum of three contributions,

$$\boldsymbol{P}_{\alpha}^{\text{Total}} = \boldsymbol{P}_{\alpha}^{\text{kin.}} + \boldsymbol{P}_{\alpha}^{\text{SM.}} + \boldsymbol{P}_{\alpha}^{\text{config.}} \tag{3.2}$$

where $\alpha \in \{x, y, z\}$ denotes the three directions where each is a vector $\boldsymbol{P}_{\alpha} = [P_{x\alpha}, P_{y\alpha}, P_{z\alpha}]^T$, with the kinetic contribution, $\boldsymbol{P}_{\alpha}^{\text{kin.}}$, which comes from the momentum transport of atoms crossing the interface (Berry, 1971), the configurational contribution, $\boldsymbol{P}_{\alpha}^{\text{config.}}$ that arises from the atomic (or molecular for molecular fluids) interaction (Walton et al., 1983) or external forces. For low temperature systems, kinetic energy of the fluid particles is low, hence configurational pressure is dominant (Shi et al., 2023). $\boldsymbol{P}_{\alpha}^{\text{SM.}}$ – is a term due to the surface movement in time. This pressure term arises when a dynamic frame of reference, which moves with the surface, is considered - for more detail please refer to (Smith, 2022). The procedure to fit the intrinsic interface, and the details relevant to the calculation of the pressure tensor can be found in Smith (2022); Smith and Braga (2020).

3.3 Interfacial Density profiles

The intrinsic density profile at temperature $T = 0.7$ is shown in Fig. 3.2 (a). Considerable oscillations are evident near the intrinsic surface layer extending at least five atomic diameters into the liquid phase (density is averaged over ± 5 time steps, and also in the y and z spatial directions). Although such layering is a universal behavior of the free surface (Chacón et al., 2001), if the reference frame were static, one would not obtain such strong layering for an LJ fluid. On the other hand, a moving frame of reference makes the layering evident. This layering directly determines the stress that would be measured, both on the interface itself and in the bulk fluid. In the next sections, we focus on the effects of such layering on the surface stress and thereby, on the surface tension.

As seen from Fig. 3.2 (a), the amplitude of the oscillation increases as the surface is approached from the liquid side, the highest peak is attained at the intrinsic surface and quickly dampens within a distance of less than half an atomic diameter into the vapor side. The first derivative of the density profile, $d\rho/dx$, further illustrates these

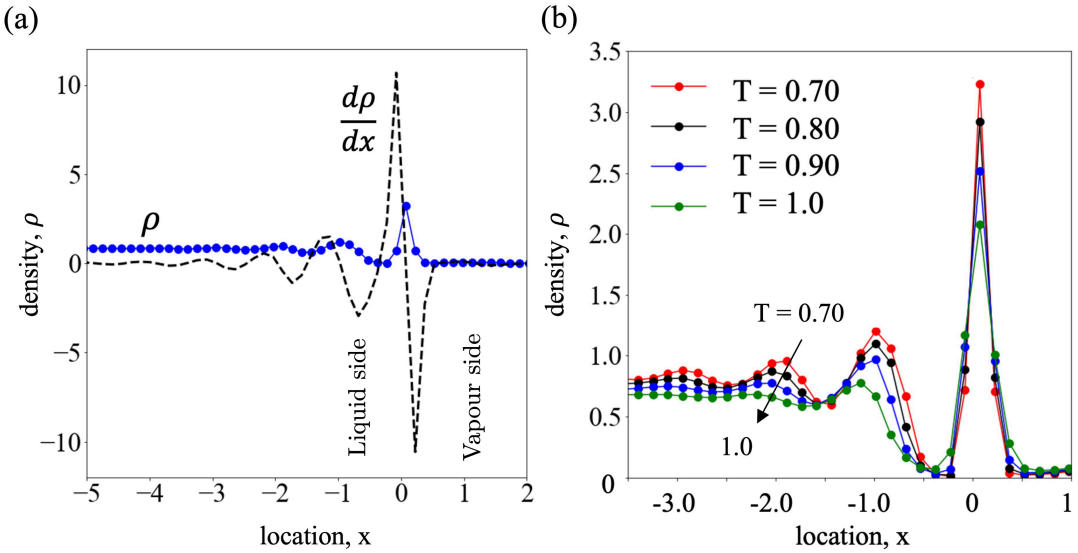


Figure 3.2: (a) Density profile (blue circles) and derivative of density (black dashed line) for $T = 0.70$ shows oscillations near the liquid-vapor interface (b) density profiles for a range of temperatures, oscillations are damped as temperature increases.

fluctuations and the zero-crossing highlights the position of the intrinsic layer. Such derivatives are also instructive of the interfacial widths, readers are referred to Sides et al. (1999) for further details. Fig. 3.2 (b), where the intrinsic density profiles are plotted for a range of temperatures, shows increased damping at higher temperatures. Evidently, the fluctuations only exist at the liquid side, and dampens quite abruptly in the vapor side right after the interface ($x > 0$), despite the existence of a small peak due to the adsorbed layer. The oscillations of the density profile at the liquid side for $x \in (-\infty, -1]$ can be approximated, as illustrated in Fig. 3.3 (a), by an exponential decay function of the form:

$$\rho(x) = \rho_{\text{bulk}} + e^{bx} \cos(\mathrm{f}\, x) \tag{3.3}$$

where, $\rho(x)$ denotes the local intrinsic density, ρ_{bulk} is the liquid density of the bulk phase far away from the interface, b is the damping coefficient, and f is the frequency of oscillation. Note that the negative sign of the exponent, i.e., the damping coef-

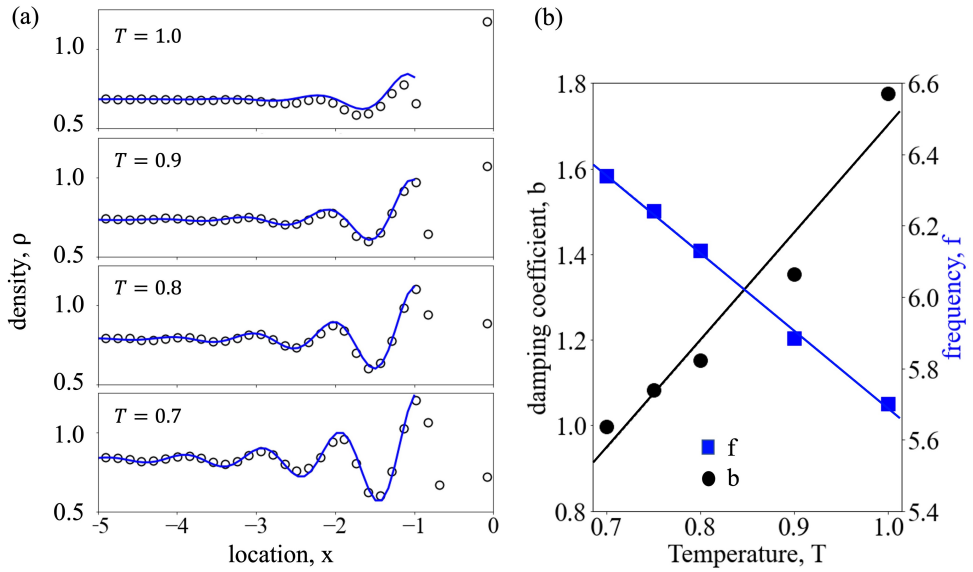


Figure 3.3: (a) Oscillation of the intrinsic density profiles: circles denote results from MD simulations, solid lines are exponential fitting, as in Eq. (3.3), to the density profiles at different temperatures, (b) the damping coefficient (left y axis, increases with temperature, whereas, the frequency of oscillation (right y axis) decreases. The solid lines are linear fits to the data.

ficient in Eq. (3.3) is discarded as the location, x in the liquid side is represented with negative numbers. The damping coefficient linearly increases, whereas the frequency of oscillation decreases as temperature is increased from $T = 0.70$ to 1.0, see Fig. 3.3 (b). Both the damping coefficient, b and the frequency of the oscillation, f show linear fits with temperature within the considered range, i.e., $b = 2.51\,T - 0.81$ with $R^2 = 0.95$ and $\mathrm{f} = -0.7\pi\,T + 2.5\pi$ with $R^2 = 0.99$. Thus the intrinsic density in Eq. (3.3) can be expressed as a function of location, bulk density of the liquid and the temperature, i.e.,

$$\rho(x) = \rho_{\text{bulk}} + e^{(2.51T-0.81)x}\cos\left[\pi(2.5 - 0.7T)x\right] \text{ for } x \in (-\infty, -1] \tag{3.4}$$

Whilst a liquid-vapor interface is not directly comparable to a solid-liquid interface, one should obtain similar damping for the same bulk liquid in contact with a solid wall (Evans et al., 1993).

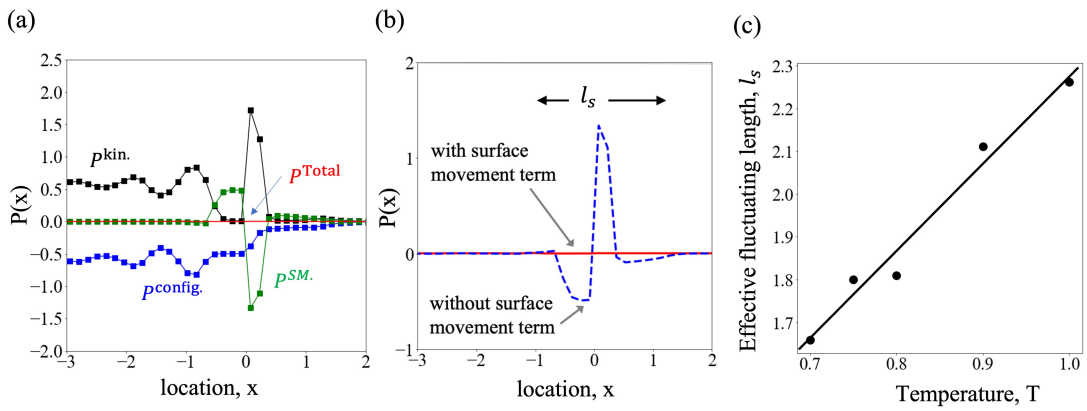


Figure 3.4: Pressure profiles at and near the surface layer for T= 0.70. (a) Components of the normal pressure: (blue line, blue square) configurational part, $P^{\text{config.}}$, (black line black square) kinetic part, $P^{\text{kin.}}$, (green line green square) contributions from surface movement, $P^{\text{SM.}}$, and (red line) the total normal pressure, P^{Total}. (b) Normal pressure without (blue line Dashed) and with (red line) the consideration of surface movement term, l_s denote the effective fluctuating length, over which the surface movements are visible. (c) Linear increase of the effective fluctuating length, l_s with temperature, the solid line is a linear fit to the data with a slope of 2.04, an intercept of 0.23, and $R^2 = 0.97$)

3.4 Interfacial Pressure Profiles

The oscillatory nature of the intrinsic profiles can be further realized from the pressure profiles. Both the normal and the tangential components of the pressure tensor can be decomposed into their constituent parts. Fig. 3.4 (a) shows these various components (averaged over time and yz plane) of normal pressure for $T = 0.70$. To track the movement of the interface and its temporal evolution at a resolution of atomic spacing, Smith and Braga (2020), and Smith (2022) discarded the otherwise applied concept of an average interaction contour and introduced an instantaneous frame of reference which evolves with the interface and hence describes the pressure tensor in a purely mechanical manner (also discussed in Chapter 2). The consideration of the surface movement contributes to an additional corrective term, $P^{\text{SM.}}$. This, when considered along with the configurational and the kinetic contributions of the normal pressure, as shown in Fig. 3.4 (a), exactly balances the momentum change to machine

precision.

The essence of the surface movement contribution is illustrated in Fig. 3.4 (b) where the normal pressure is plotted without and with the consideration of the pressure correction. Only when the surface movement effects are accounted for, the kinetic and the configurational components can precisely balance each other resulting in a perfectly flat profile for the normal pressure which signifies that the liquid-vapor interface is mechanically stable. It is apparent from Fig. 3.4 (b) that the pressure contribution due to surface movements fluctuates only over a length of few atomic diameters (where the dashed-line shows fluctuations), and remains constant elsewhere. This length is denoted as the *effective fluctuating length*, l_s (schematically shown in Fig. 3.4 b). In this study, a cut-off value $\epsilon = 0.05$ is used in order to numerically determine l_s from the fluctuations of $P(x)$. As shown in Fig. 3.4 (c), l_s increases linearly with the temperature. Despite that the interfacial thickness assumes approximately the size of an atom at a temperature away from the critical temperature (Lu and Hu, 2008), the effective fluctuating length demonstrates that the kinetic contribution spans over at least a few atomic diameters. This is reasonably justified in light of the fact that a higher temperature corresponds to greater surface movements and thereby, a (kinetically) thicker interface (Goujon et al., 2016).

The temperature effect on the intrinsic pressure profile has further been examined in Fig. 3.5. Though the shape of the normal pressure profile remains unaltered irrespective of temperature, the oscillations of the configurational and the kinetic parts, in Fig. 3.5 (a−d), are seen to smooth out as temperature increases. The normal and the tangential components of the pressure, along with $(P_N - P_T)$, are plotted in the Fig. 3.5 (e−h) for different temperatures. Interestingly, the tangential pressure profiles become less corrugated at higher temperatures, that is, the spatial oscillations or the expansion and contraction of the surface become less prominent. Such behavior can be ascribed to the more energetic interface at higher temperature making the interface tracking difficult. The oscillations are directly comparable to those in the intrinsic density profiles, as in Figs. 3.2 and 3.3. The equal and opposite of this kinetic component is the configurational pressure, as shown in Fig. 3.5 (a−d), which ensures equilibrium. The observations made in Fig. 3.4 (c) and Fig. 3.5 allow to conclude that

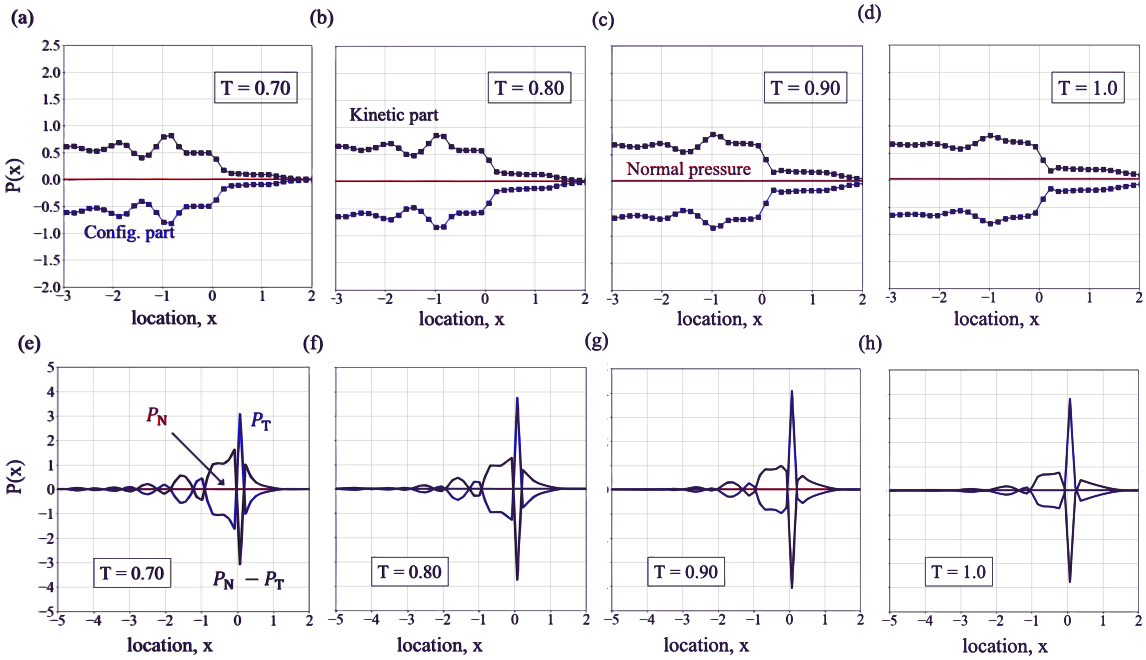


Figure 3.5: (a-d) Constituent parts of the normal component of pressure, i.e., the kinetic part and, the configurational part for (a) T= 0.70, (b) T= 0.80, (c) T= 0.90 and, (d) T= 1.0. (e-h) Variation of the tangential component of the pressure tensor and of $P_N - P_T$ near the interface for $T = 0.70$ to 1.0.

an increase in temperature dampens the oscillations of the intrinsic profiles, and at the same time, broadens the effective fluctuating length, l_s, over which surface movement effects are present.

The influence of the oscillations discussed, are confined to a small interfacial region. Far from the liquid-vapor interface, both the normal and the tangential pressure become equal and uniform. Hence, it is not surprising that only the region of a few atomic diameters from the interface (both in the liquid and the vapor sides) contributes to the surface tension. The term inside the integral of Eq. (2.6) is plotted (black solid line) in Fig. 3.6 (a) along with the cumulative integral, i.e, the surface tension, γ. The magnitude of the surface tension is seen to reach a plateau right after the peak, within an atomic diameter in the vapor-side. A careful examination of the intrinsic surface (i.e., $x = 0$) thus portrays its outright significance in determining

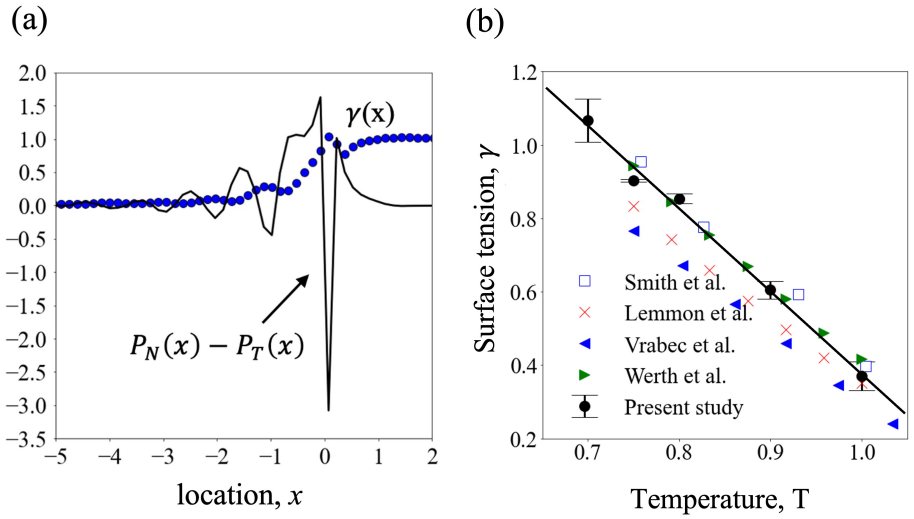


Figure 3.6: (a) Difference between the normal and the tangential pressure, $P_N - P_T$ (black line) near the interface. The cumulative integral of $P_N - P_T$, i.e., the surface tension, $\gamma(x) = \int_{-10}^{x} [P_N(x') - P_T(x')]\, dx'$ is shown by the filled circles (blue circle) where, the lower limit of integration is kept fixed at $x = -10$ and the upper limit is gradually increased up to $x = 2$. (b) Surface tension from present modeling (black circle) shows good agreement with results from previous experiments and simulations. The error bars denote the standard deviation of surface tension as measured from three separate ensembles. The solid line is a linear fit (with slope $= -2.26$, intercept $= 2.63$ and $R^2 = 0.99$) to the surface tension obtained from the present study.

the surface properties, as seen in Fig. 3.6 (a), where the large negative peak of the pressure difference at $x = 0$ contributes significantly to the integral of Eq. (2.6). Fig. 3.6 (b) compares the surface tension evaluated at different temperatures with available experimental data for liquid argon (Lemmon, 1998), results from molecular simulations with truncated and shifted potential with a cut-off radius of 2.5 (Goujon et al., 2014; Vrabec et al., 2006), and 4.0 (Smith et al., 2016), and truncated potential with long range corrections and cut-off radius of 3.0 (Werth et al., 2013) − as seen in the figure, the comparison suggests good agreement.

3.5 Surface Stress and Fractal Dimension

The preceding sections discuss the temperature effects on the intrinsic profiles, and on the corresponding values of the surface tension. How such alterations take place, however, remain unclear. To investigate this, and because the configurational stresses are the sole contributors towards the surface tension, the distribution of these stresses are examined, ignoring the kinetic components, at the intrinsic surface layer ($x = 0$); i.e.,

$$P^{\text{config.}}(x = 0) = \frac{1}{2}\left[P_{\text{yy}}^{\text{config.}}(x = 0) + P_{\text{zz}}^{\text{config.}}(x = 0)\right].$$

Fig. 3.7(a) shows an instantaneous configurational stress distribution map at the interface. The filled black squares correspond to the atomic locations which the intrinsic interface is fitted to, at that particular instant. In Fig. 3.7(b), only stresses that contribute to the tension of the surface (negative stresses) are shown, where a cluster spreading over the surface becomes apparent. These 'non-trivial' networks and their variation with temperature are analyzed by means of fractal analysis.

Fractal dimension is a measure of the complexity or roughness of a geometric shape that does not fit neatly into traditional, smooth dimensions like 1D (a line), 2D (a rectangle), or 3D (a box). For instance, a straight line has a fractal dimension of 1.0, but if the line becomes wrinkled or space-filling, the dimension can be described by non-integers that may vary between 1 and 2, reflecting its increased complexity, the dimension is still lower than 2.0 as it is not two-dimensional, but higher than 1.0. A classic example is the *Koch snowflake*, a curve constructed by adding smaller triangular bumps along each side of an equilateral triangle. As more bumps are added (repeating unit), the shape becomes increasingly complex, and its fractal dimension approaches to 1.26. Another example would be the fractal dimension of the coastline of Great Britain, which is 1.25. Where traditional Euclidean dimensions do not capture the shapes and complexities in natural structures like coastlines, clouds, mountain ranges etc., the fractal dimension helps quantifying these complexities. In following section, we apply this idea in quantifying the space-filling nature of the stress network formed at the liquid-vapor interface.

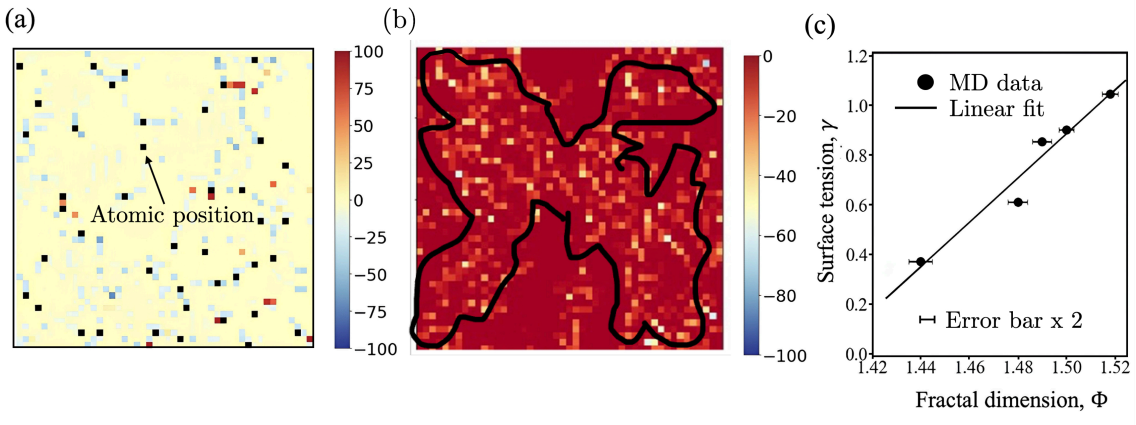


Figure 3.7: Instantaneous stress map at the liquid-vapor interface for T = 0.80. (a) Color map of the configurational stress distribution with atomic positions overlaid (filled black squares). (b) Only negative configurational stresses, outline showing the stress-network. (c) Surface tension as a function of the fractal dimension of stress network at the surface layer over the range of temperatures considered in this study, error bars (with a magnification factor of 2 for visualization purpose) denote standard error of the mean of fractal dimension, SEM, the solid line is a linear fit with $R^2 = 0.95$.

To quantify the temperature dependency of the structural complexity of the stress networks, their fractal dimensions, Φ are measured. This dimension is often used to quantify the space filling nature, heterogeneity or self-similarity of surfaces, clusters etc. (Avnir et al., 1984; Chen et al., 2015; Jelinek et al., 2006; Shen et al., 2020) Φ is calculated through the Minkowski dimension (Hassan et al., 2012; Kempkes et al., 2019), which is often referred to as the box-counting dimension, whereby, for non-overlapping N boxes with sides ς (the methodology to obtain Φ is further elaborated in Appendix C.2),

$$\Phi = \lim_{\varsigma \to 0} \frac{\log N(\varsigma)}{\log(1/\varsigma)}. \tag{3.5}$$

The algorithm employed to calculate Φ consists of converting the network maps (as in Fig. 3.7 b) into binary images such that the stress networks are depicted by black pixels on white background. For a given grid side, ς the number of grids, $N(\varsigma)$ required to fill the projected surface area of the aggregate is counted and the grid is made increasingly finer at each subsequent iteration. The fractal dimension, Φ is then obtained from the slope of $\log(N)$ vs $\log(\varsigma)$.

With the variation of temperature, we have observed consistent behaviour of the fractal dimension of the network comprised of the negative configurational stresses that lie within $\left[P_{\text{n,m}}^{\text{config.}} - \sigma, P_{\text{n,m}}^{\text{config.}}\right]$, where $P_{\text{n,m}}^{\text{config.}}$ denotes the mean of all the negative configurational stresses, and σ denotes the standard deviation. The fractal dimensions thus obtained are compared against the corresponding surface tensions in Fig. 3.7 (c). For the temperature range considered here, Φ is seen to linearly correspond to the surface tension as $\gamma = 9.86\,\Phi\ - 13.86$ which is shown by the solid line. This reflects the greater space filling nature (Jelinek et al., 2006) of the (surface) stress network at a lower temperature. At the same time, the fractal dimension of the stress clusters only at the outermost atomic layer proves to be predictive of the surface tension.

In hydrodynamics, the surface tension, γ is often modeled as an equation of state in terms of temperature, surfactant concentration etc. This seemingly mechanistic approach does not capture the subtleties of the mutual interactions between the various effects nor does it directly model the fundamental thermodynamic nature of

surface tension, that is, the free energy it would cost to form an interface. On the other hand, a localized surface fractal stress approach to surface tension via the calculation of localized fractal dimensions of the interface stress distribution would improve on both of these issues. Firstly, in a system where thermo- and soluto-Marangoni effects are in play, the localized fractal stress would take into account both of these two effects and their interactions with each other without any loss of generality. Secondly, the localized fractal stress can provide a standardized platform upon which all possible effects on surface tension (whether local or global) can be examined in an uniform and consistent way. In this sense, a higher localized fractal stress can be directly interpreted as a higher energy cost required to form the interface in that region, thereby resulting in a higher localized surface tension. A complete hydrodynamic description of this interesting problem is not pursued in this study, but numerous applications of this approach is anticipated in modeling of nano-fluidic interfacial phenomena where local variation of surface tension is frequent.

3.6 Percolating Stress Clusters at the Surface

The accurate identification of the intrinsic surface layer allows to further the analysis of the atomic interaction network by applying the concept of percolation (Dapp et al., 2012; de Souza and Harrowell, 2009; Heyes and Melrose, 1988; Pathak et al., 2017; Sega et al., 2014; Stauffer and Aharony, 2018). This method examines the 'connectedness' of the different sites (or cells) on the interface that experience stress lower than a threshold. For a critical stress, a connected network of sites or a spanning cluster is formed that spans from left to right and from top to bottom of the lattice. If such spanning clusters form in at least 50 percent of the configurations, a system is described as a percolating system (Seaton and Glandt, 1987; Zarragoicoechea et al., 2005) and the corresponding stress is known as the percolating threshold (Bug et al., 1985; Hasmy et al., 2021; Heyes and Melrose, 1988, 1990, 1989). Here, configuration means the instantaneous behavior of the system captured at a single time step. The stress percolating threshold at the intrinsic interface is determined to assess the temperature effect.

To quantify the threshold, percolation is considered in both directions (left-to-right

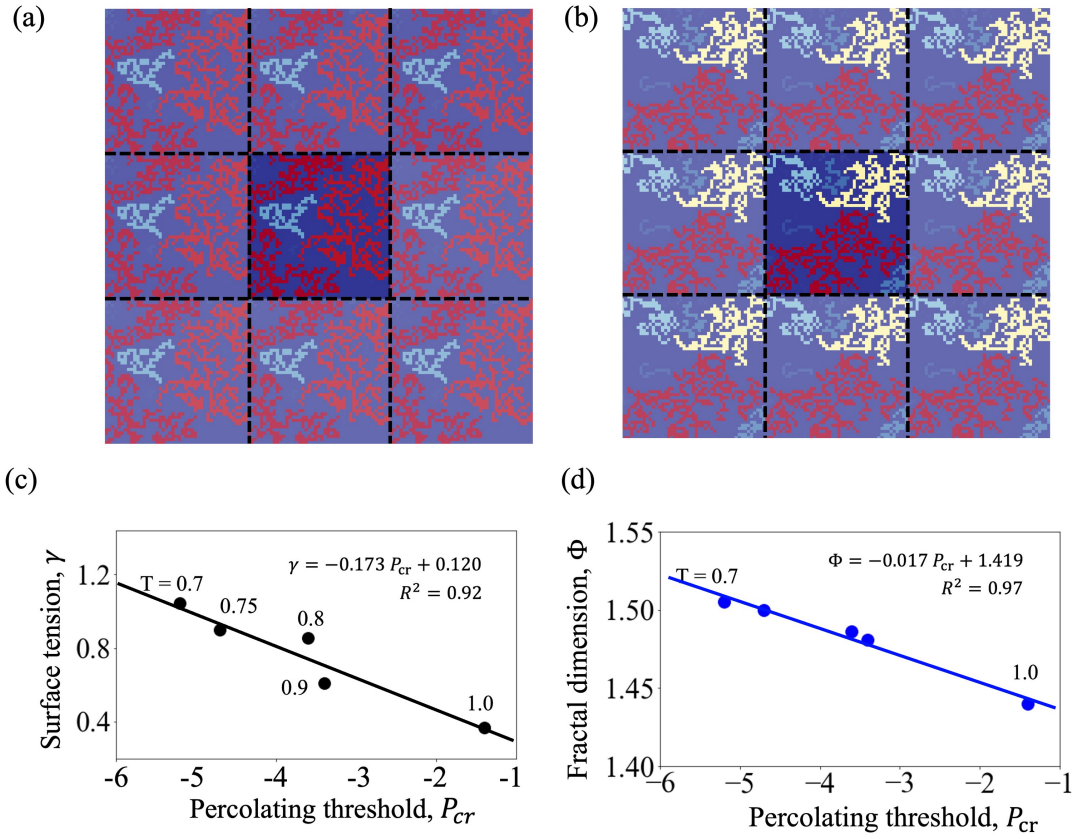


Figure 3.8: Percolation network, with periodic images shown faintly, at a random instant at temperature (a) T = 0.8 and, (b) T = 1.0. The largest cluster is colored red. Panel (a) shows a spanning cluster, whereas, in panel (b) no cluster is spanning throughout the surface for the same stress threshold. (c) Surface tension, and (d) fractal dimension as functions of the percolation threshold over the range of temperatures considered in this study, lines are linear fits.

and top-to-bottom) with the application of next-nearest neighbors algorithm. Fig. 3.8 (a) and (b) show two randomly selected instances, respectively for $T = 0.8$ and 1.0, where spanning clusters form for the case of $T = 0.8$, but no such cluster is seen for $T = 1.0$. Such networks can be interpreted as a manifestation of the stress heterogeneity at the surface, which essentially increases with temperature resulting in a lower surface tension. Indeed, at lower temperature, the majority of the surface experiences higher negative stress, and thereby a spanning network can form at a relatively larger

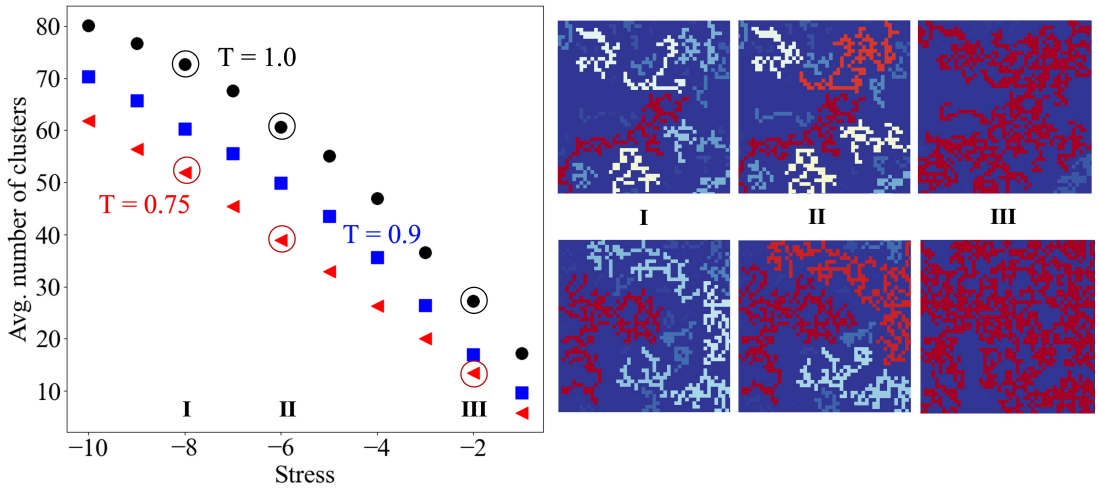


Figure 3.9: Average number of clusters at different stresses for $T = 0.75$ (red triangles), 0.9 (blue squares) and 1.0 (black circles). The top panel in the right hand side corresponds to three instantaneous networks formed with stresses I $:(-\infty, -8]$, II $:(-\infty, -6]$ and III $:(-\infty, -2]$ for $T = 1.0$. The bottom panel shows similar networks but for $T = 0.75$. The average number of clusters associated with I, II and III are circled in the left panel.

(negative) stress threshold. On the contrary, as temperature increases, the heterogeneity in stress distribution increases too, and hence the formation of a spanning network requires the inclusion of smaller clusters. Fig. 3.8 (c) illustrates this, where the surface tension is plotted as a (linear) function of the percolating threshold. A lower value of the surface tension (which corresponds to a higher temperature) is seen to be associated with a lower (negative) percolating threshold, whereas, a higher surface tension (lower temperature) is related to a larger magnitude of the threshold. Similar functional dependency between the percolating threshold and the fractal dimension of the stress networks can be seen in Fig. 3.8 (d), which further echos the higher space filling nature of the surface clusters with lower stress heterogeneity at a lower temperature.

Not only the stress networks at distinct temperatures differ at the percolating threshold, but their ability of cluster formation also varies at any stress. In Fig. 3.9, the average number of clusters are plotted for a range of stresses. It is evident that

for any particular stress, the (average) number of clusters at a lower temperature is less than that at a higher temperature, meaning that the low temperature clusters are larger and less heterogeneous, in terms of stress, than their high temperature counterparts. For instance, the top panel in the right hand side of Fig. 3.9 shows three instantaneous networks for (negative) stresses with magnitudes greater than $8, 6$ and 2, with the largest clusters colored in red. It is seen that the clusters grow in size as the field becomes more inclusive of stresses from panel I to III. Similar growth of the cluster size is seen for a lower temperature surface, i.e., for $T = 0.75$ as in the bottom panel. However, what differs between the networks at the two temperatures of interest here is: for identical range of stresses, it is more probable to obtain a larger cluster for a lower temperature surface.

From a thermodynamic point of view, a liquid-vapor interface at a higher temperature is (thermally) more energetic (Palmer, 1976) and thereby, favors a broader interface and weaker spatial correlation between atoms with larger nearest-neighbors distances causing a lower surface tension (Bhanvase and Barai, 2021). This, however, is challenging to perceive via a mechanical route - the inherent difficulty lying in separating the actual surface layer from the capillary fluctuations (Sega et al., 2014). Such complication is circumvented in this study by detecting the interface using the intrinsic sampling method and collecting stresses in a reference frame moving with the surface which establishes the ground for an authentic surface-network analysis. Through this route, a thermodynamically weaker surface (due to the weaker spatial correlation between atoms) is mechanically represented, by the lower 'connectivity' (Alvarado et al., 2017; Burnley, 2013) or higher heterogeneity of the stress networks. Stated differently, a high temperature surface (of which, surface tension is lower) can be mechanically described as a surface that is loosely inter-connected by disjointed networks of stresses. Although the sensitivity of the analysis is limited by the probabilistic nature of the quantities investigated, the sole analysis of the sharpest atomic description of the intrinsic interface proves to be useful to unravel the variation of surface properties with temperature.

Whereas the intriguing notion of interpreting surface properties through surface coverage remains challenging (Menger and Rizvi, 2011; Mu et al., 2006), the stress

network approach presented in this chapter is quite straight forward. Simplification of the interface by modeling an LJ fluid is a key limitation of this study, but the approaches developed here could be extended to molecular fluids in future work.

3.7 Summary

By simulating the liquid-vapor interface of an LJ fluid, this chapter presents a mechanical interpretation of surface tension and its variation with temperature. Intrinsic sampling method is used to define a moving frame of reference and an equation for the interfacial density, $\rho = \rho(x, T)$ for $T \in [0.7, 1.0]$ and $x \in (-\infty, -1]$ is presented. Stress-clusters at the intrinsic surface are identified, and their non-uniform spatial correlations are analyzed. The atomic interactions at the intrinsic surface layer can be thought of as a network of stresses holding the surface altogether. At an elevated temperature, the network becomes more disjointed and thus less stable.

Both the fractal dimension and the percolating threshold of the stress network can be correlated with the surface tension. These observations suggest that the pattern formation and the connectivity of the stress networks at the intrinsic interface are good indicators of surface tension. Importantly, the analysis of the stress-network only at the outermost atomic layer suffices to provide a consistent prediction over a range of temperatures. The surface tension acquired from the simulation agrees well with previous MD simulations using different methods and experimental data for liquid argon, which advocates for the extrapolation of the findings of this study to liquid-vapor interfaces of molecular systems of interest.

This page intentionally left blank.

The task is, not so much to see what no one has yet seen; but to think what nobody has yet thought, about that which everybody sees.

Erwin Schrödinger

4

Thin Film Rupture: Formation to Fragmentation

THIN FILMS, BUBBLES AND MEMBRANES are central to numerous natural and engineering processes. Yet, the characterization and an adequate understanding of their rupture is limited by the scarcity of atomic detail. This chapter presents the complete life-cycle of freely suspended films using non-equilibrium molecular dynamics simulations of a simple atomic fluid free of surfactants and surface impurities, thus isolating the fundamental rupture mechanisms. A short-term 'memory' is identified by rewinding in time from a rupture event, extracting deterministic behaviors from apparent stochasticity. A comprehensive investigation of the key rupture-stages including both unrestrained and frustrated propagation is made. Furthermore, the highly resolved time window reveals that the different modes of the morphological development, typically characterized as nucleation and spinodal rupture, evolve seamlessly with time from one into the other*.

*A version of this chapter has been published as Rahman, M.R. et al., Life and Death of a Thin Liquid Film, Communication Physics, Nature, 2024.
Codes to reproduce the data are publicly available at:
https://github.com/MuhammadRRahman/Thin-Film-Rupture-NEMD.

4.1 Introduction

Isaac Asimov's *Foundation* series introduced the concept of *psychohistory* - where historical trends enable statistical forecasts of the overall trajectories of the civilization while not predicting individual or transient events. In terms of rupture and nucleation dynamics, this parallels the notion of being microscopically stochastic yet macroscopically deterministic − an important distinction as one works through a complete description of the multi-scale rupture process of a thin liquid film, as described in this chapter.

For the break up thin films, local fluctuations in film density and thermal noise have non-negligible impact (Morariu et al., 2003; Sharma et al., 2002), and depending on the scale of the problem they may stabilize or de-stabilize the film (Israelachvili, 2022). By manipulating the ratio of hydrodynamic to capillary stresses in polymer solution films, Chatzigiannakis and Vermant (2020) demonstrated the increasing dominance of (stochastic) thickness fluctuations over the (deterministic) hydrodynamic forces. The impact of these atomic scale local fluctuations leading to the ultimate failure of a thin film constitute the key focus of this chapter. A homogeneous system composed of pure Lennard-Jones particles is chosen - thereby, focusing on the fundamental physical response of the film. These films, while relevant to the rupture of surfactant-free metallic films (Anderson et al., 2010; Schebarchov et al., 2013), liquid crystals (Nguyen et al., 2014a), emulsions and membrane (Knutton, 1979), and for films in micro-gravity environment (Langevin, 2017), also enhances the general understanding of the importance of atomic-scale local fluctuations in rupture mechanism.

Despite the morphological similarities with surfactant laden and supported films, free standing pure films exhibit fundamental differences. Consequently, the insights obtained, while illuminating, may not be directly applicable to the former cases due to the necessity of considering surfactant properties, contact line dynamics, gradient-driven advection, and diffusion (we will revisit some of these in Chapter 6). The intricate coupling among these processes has rendered their direct measurements elu-

sive. Furthermore, any effort to trace contaminants invariably modifies their properties, thereby effecting the system's dynamics (Manikantan and Squires, 2020). In contrast, with direct access to individual molecules and their immediate properties, the molecular dynamics investigation of pure films establishes a reference-point for studies addressing more complex and specific scenarios.

The central topic of the current investigation concerns the complete life-span of thin (black) films, and their rupture mechanism. By unveiling the fundamental aspects and the behavior of thin films at the smallest of scales and mapping the mechanisms responsible for the evolution of films across space-time coordinates, this study provides, for the first time, a simplified, yet fundamental view of the evolution of thin-film dynamics. This is achieved by tracing back and explaining the links between inception and fragmentation phases, and by identifying the structural similarities emerging at different scales. The subsequent sections of this chapter are structured as follows: the discussions begin by identifying the shared characteristics among various modes of rupture, and by unifying them. Following this, a time-sequencing behavior of the film is demonstrated in the moments leading up to its rupture. This deterministic aspect within the typically stochastic rupture process underscores the general principle that the interplay between stochastic micro-scale events and deterministic macro-scale outcomes is essentially a common thread across diverse fields of study. Finally, detailed illustrations of the nucleation event, the late stage frustrated propagation leading to coalescence are provided. The latter gives fresh insights on factors responsible for slower propagation and, hence, delayed coalescence. To avoid any potential ambiguity, it should be emphasized at this point that the term 'nucleation' in this chapter exclusively refers to the atomistic process of hole formation in the freely suspended films.

4.2 Simulation Details:

The model films studied here are composed of single component Lennard-Jones (LJ) particles, i.e.,

$$V_{ij}(r) = 4\varepsilon_{ij}\left[\left(\frac{\sigma_{ij}}{r_{ij}}\right)^{12} - \left(\frac{\sigma_{ij}}{r_{ij}}\right)^{6}\right]$$

here, V_{ij} is the potential between particle i and j located at a distance r_{ij}, and free from electrostatic interactions. The dispersion energy is described by ε_{ij}, and σ_{ij} is the characteristic length scale. Periodic boundary conditions are applied in all three Cartesian directions. Simulations were carried out employing the extensively validated and verified open-source Flowmol MD code (Smith, 2013).

The initial simulation domain was represented by a cubic box with dimensions $L_x = 76.19$ and $L_y = L_z = 609.56$ in LJ units, translating to film dimensions approximately 207 nm wide and with a depth (h_0) of less than 5 nm. In order to reduce the computational cost in simulating the relatively large systems, a cut-off radius, $r_c = 2.5$ is used which has been proved to be sufficient in previous film rupture studies (Koplik and Banavar, 2000; Nguyen et al., 2014b). Throughout this chapter, all measurements and quantities are expressed in LJ units. The central 20% of the simulation box along the x axis was assigned as the liquid phase, with a targeted density of $\rho \approx 0.7$, while the remaining region was designated as the vapor phase with a lower density of $\rho \approx 0.01$. Note, unless otherwise stated, all parameters are reported in Lennard-Jones units, i.e., length in σ where $\sigma = 0.34\,\text{nm}$ A cohesive central liquid film, consisting of around $\sim 0.4 - 1.8$ million identical atoms, coexists harmoniously with the surrounding vapor phase at an equilibrium state. The system was allowed to equilibrate (at $T = 0.78 \pm 0.03$) to a stable liquid-vapor coexistence state. This equilibration was conducted in the canonical ensemble (NVT), utilizing a Nośe-Hoover thermostat, over a span of 50,000 time steps with a timestep size of $\Delta t = 0.005$. The equilibrium state served as the starting point for subsequent production runs in the microcanonical (NVE) ensemble. This phase proceeds without the intervention of any thermostat or other external control mechanisms, thereby enabling the natural evolution of the system, and the emergence of nanoscale fluctuations intrinsic to the phenomena of interest (Kadau et al., 2004; Nguyen et al., 2014b; Sprittles et al., 2023; Zhang et al., 2019). In addition to a system's ability to evolve freely from external thermostat interference in the micro-canonical ensembles (Hammonds and Heyes, 2020), this choice is further motivated by several factors. One of the most efficient thermostats, i.e., the Nose-Hoover thermostat, has been shown to alter mean square displacement and potentially disrupt time-dependent correlations in fluids (Frenkel

and Smit, 2023). In light of the uncertainties surrounding the impact of thermostats on transport properties (Dysthe et al., 1999), the choice of the NVE ensemble ensures that energy transformations occur naturally, thereby providing a more accurate depiction of the system's dynamics without artificial adjustments (Allen and Tildesley, 2017; Rapaport, 2004). To explore films with different thicknesses, the dimension in the x direction was systematically varied.

4.2.1 Restart Simulations:

System states, $\Gamma(t)$, were saved at regular intervals, creating restart points denoted as time t_0. For restarting a simulation the restart state $\Gamma(t_0)$ served as the initial condition. This ensured that multiple independent simulations restarted at t_0 from an identical initial state with a different trajectory due to the divergence of trajectories in phase space. In this rewind exercise, the simulations were restarted with the application of a small random nudge to all the particle velocities. To perturb the particle velocities, $\boldsymbol{v}_i$ for all particles, i were nudged as $\boldsymbol{v}_i(t_n) = \boldsymbol{v}_i(t_0) + \Delta\boldsymbol{v}_i$ to create any of n nudged trajectories, where $\Delta\boldsymbol{v}_i = C\boldsymbol{\zeta}_i$, with $C = 10^{-8}$ – a infinitesimally small floating point number, however sufficient to nudge as the contribution accumulate over time and diverge the phase-space trajectory, and $\boldsymbol{\zeta}_i$ is a random number. It was ensured that the cumulative sum of these perturbations remained zero, i.e., $\sum_{i=1}^{N}(\Delta v_i) = 0$, precluding the introduction of any net momentum into the system.

4.2.2 Synthetic Nucleation

To initiate synthetic nucleation, an external force was applied, as in Eq. (4.1), to mimic the popular experimental film-puncturing procedure (Bird et al., 2010; Oratis et al., 2020; Savva and Bush, 2009).

$$F_{\text{ext.}} = \begin{cases} F\left(1 + \mathrm{e}^{-1/r^2}\right) & r \leq R_0 \\ 0 & \text{otherwise,} \end{cases} \tag{4.1}$$

where, R_0 is the initial radius of the hole. The forcing time was only a few hundred time-steps to confirm that a stable hole is created, and R_0 was kept sufficiently small of the order of the film thickness. Investigations reported in Chapter 5 demonstrate that

this synthetic nucleation process does not impact the growth dynamics of the nuclei. Note, this synthetic hole making technique is applied only when investigating the Taylor-Culick retraction theory (Chapter 5), and for the sections detailing frustrated growth in section 4.7.

4.3 Overview of the Life Span of a Film

The rupture process is long preceded by the drainage and subsequent thinning of the metastable film. Thinning is driven by capillary suction, which is followed by the development of an instability leading to rupture. Such an instability is caused by the heterogeneity in film thickness, or due to the gradients in surface concentration (de Gennes, 2001; Saulnier et al., 2014). Fig. 4.1 summarizes the full life-time of a film: starting from hydrodynamic thinning at micron thickness (region 1 in Fig. 4.1) and fluctuations dominated thinning at nanoscale (region 2), followed by a piercing stage when surface fluctuations grow more rapidly at some sites (or, locations) compared to others leading to nucleation (region 3). Depending on the initial film thickness, however, the rupture process may follow one of the several modes of nucleation; and although a stochastic process, a finite window of memory is observed - these we discuss in the next two sections. Once the film is punctured, a short term exponential growth regime emerges (region 4) when the nucleus attains a circular shape and eventually enters the linear growth regime (region 5). This linear growth, referred to as the Taylor-Culick retraction, has been extensively investigated in the literature, both numerically and by experiment. It was observed that by appropriately resolving the surface forces, curvature effects, and the momentum of the accumulated liquid mass, the Taylor-Culick framework, which was originally proposed (Culick, 1960; Taylor and Michael, 1973) and examined (McEntee and Mysels, 1969) for soap films and films with surfactants, is highly effective at describing the retraction of atomic-scale pure unbounded films (Chapter 5). Depending on the modes of nucleation and the film thickness, multiple rupture sites may nucleate and continue to grow. This growth is later affected by the presence and growth of neighboring nuclei, and a frustrated growth regime emerges leading to delayed coalescence and coarsening. These stages will be discussed separately in sections to follow.

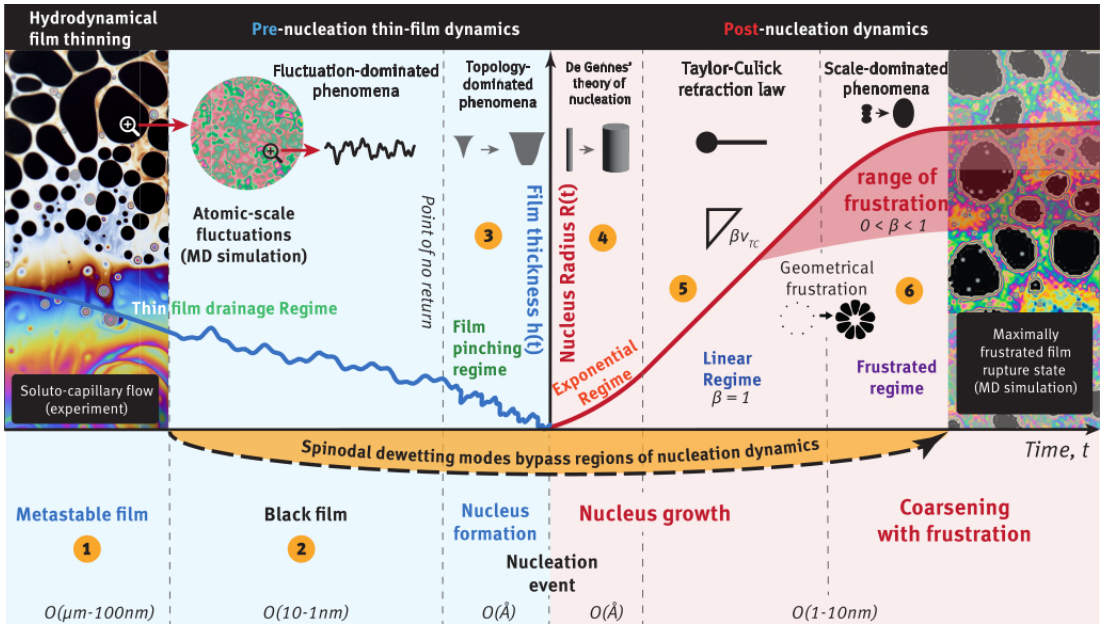


Figure 4.1: Portrait of the life-span of a thin-film. The left half of the schematic, regions 1-3, shows thinning in stages before nucleation, the y-axis represents film thickness (not to scale). The far-left (region-1) snapshot shows (experimental) hydrodynamic thinning in a micron-thickness metastable films which leads to the formation of nanoscopic black films. Remaining parts of the schematic summarizes molecular dynamics observations which are inaccessible by experimental investigation: (region-2) fluctuation dominated thinning of black films, (region-3) as rupture becomes imminent, thinning is accelerated and leads to film pinching and eventually to nucleation when $h = 0$. The just-nucleated site now starts expanding. Subsequent growth of the ruptured site is presented in the right half of the figure (shaded in faint red, regions 4-6) with the y-axis now representing the radius of the rupture site. (region-4) Initially growth is exponential which soon attains (region-5) linear growth. As more sites rupture across the film, their presence and growths frustrate the growth of any individual site as in (region-6) which later follows coalescence and coarsening - the far right snapshot from MD simulations shows a typical state of the (black) film at this stage with expanding holes in it. The spinodal rupture is fast-forwarded from 1 to 6, even at the MD scale, (almost) bypassing the intermediate stages.

4.4 Modes of Rupture

Spinodal rupture vs. Nucleation: In a freely suspended film (and also those on a substrate), *spinodal disintegration* (Becker et al., 2003; Higgins and Jones, 2000;

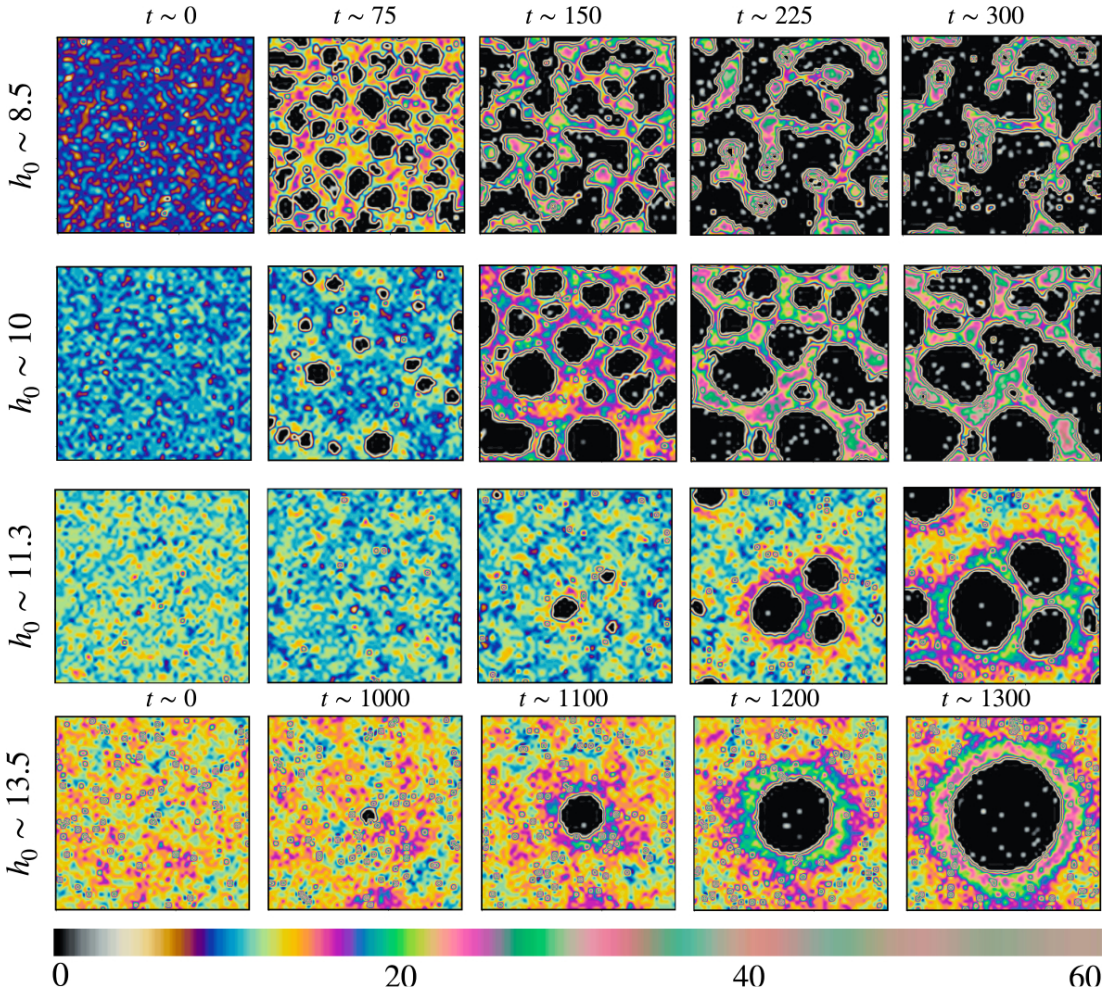


Figure 4.2: Spontaneous rupture of films of different initial thicknesses, $h_0 = 8.5, 10, 11.3$ and 13.5 in LJ units. Color maps represent the local thickness. The presence of surface modulations are seen in the unruptured states of the films.

Thiele et al., 2001; Vrij, 1966a; Xie et al., 1998) refers to its solely thermodynamic and rapidly spontaneous disintegration under the influence of molecular interactions. For films with surface impurities or defects, energy barrier that the film needs to overcome in order to nucleate is (locally) lowered resulting in *heterogeneous nucleation* randomly distributed over the film. In cases where surface defects and contaminants are absent, as in the present study, nucleation-like events can still occur as a result of (thermal) fluctuations. As such, the occurrence of surface instability is primar-

ily connected to linearly unstable films, and nucleation at defects is often linked to metastable films; Thiele et al. (2001), yet showed instability dominated and nucleation dominated sub-ranges within the linearly unstable range.

Present results give evidence of the co-existence of spinodal and the nucleation modes of rupture in freely suspended thin films. Fig. 4.2 shows snapshots of the film thickness at different times for varying initial thickness, h_0. The thinnest film ($h_0 \sim 8.5$, top row) displays transition from 'vapor-in-liquid' to bi-continuous to 'liquid-in-vapor' state commonly seen in spinodal process (Bestehorn and Neuffer, 2001). The irregular shapes and sizes of the nuclei arise not only from early coalescence but also from the interactions between, and coalescence of, neighboring nuclei. As the film thickness increases (from top to bottom panels), the nuclei become more circular, and regularly shaped − a typical characteristic assigned to nucleation (Reiter, 1994; Stange et al., 1997; Thiele et al., 1998). These observations agree with the experimental investigation with polystyrene films on silicon substrates by Xie et al. (1998) who proposed a crossover thickness from spinodal to nucleation dominated processes.

The coexistence of both of the modes discussed above was also observed for evaporating structural protein films (Thiele et al., 1998), for liquid metals (Bischof et al., 1996; Herminghaus et al., 1998; Nguyen et al., 2014a), and for polymer films (Jacobs et al., 1998; Seemann et al., 2001; Xie et al., 1998). However, these studies were based on liquid films on solid substrates, and to the best of the author's knowledge, the rupture of freely suspended single component films has not been systematically investigated until now. In the current study, the observations of rupture for various thicknesses agree qualitatively with the commonly observed patterns found for spinodal rupture and nucleation; but most importantly, these are found to initiate spontaneously without the presence of surface impurities or external perturbations. It is clear from the present free film model that the 'nucleation' observed in this study must arise from highly localized thermal fluctuations, in contrast to any substrate defect as in Thiele et al. (1998) and elsewhere.

The identification of the predominant mechanism and their potential overlapping

has been a focal point of research for years (Nguyen et al., 2014a; Thiele et al., 1998, 2001). A critical and intuitive determinant is the modality of the hole size distributions (Thiele et al., 1998). In the present study, we observe that thicker films displays unimodality, typically assigned to nucleation, whereas, relatively thinner films predominantly exhibits bimodal distribution, indicative of the existence of two distinct hole formation mechanisms (Bischof et al., 1996; Thiele et al., 1998; Xie et al., 1998). These observations, detailed in the Appendix A (figure A.7 showing size distributions for films with $h_0 \sim 11$ vs. 9.5, and associated discussions), underscore the nuanced interplay between film thickness and rupture behavior.

Upon nucleation within a comparatively thicker film, an individual nucleus undergoes expansion at the Taylor-Culick speed, creating a rim (where the liquid accumulates) encircling it (Rahman et al., 2023). This rim serves as a deterrent to the growth and coalescence of approaching neighbor nuclei, and thereby delays coalescence (which we discuss later in further detail). When an individual nucleus finds it energetically more favorable to amalgamate than to continue to grow, coalescence takes place. In contrast, the dynamics differ for spinodal rupture where nucleation occurs 'almost' simultaneously at multiple sites, creating a uniform distribution across the film. Consequently, the nuclei face spatial constraints, hindering their expansion. Additionally, spinodal rupture typically takes place in relatively thinner films with higher nuclei growth rates, facilitating easy expulsion of the liquid bridge trapped between neighboring nuclei resulting in an earlier coalescence stage.

Notably, these observations highlight that the overlapping of, and the transition between these modes can occur solely based on the thickness of the film and on the spread of the surface instability, indicating the critical role played by the film thickness in determining the dominant mechanism. This, therefore, expands the remit of the present results potentially to other substrate-free situations. In addition, it can be inferred that any apparent dissimilarity in the rupture patterns of two films of different h_0 must arise from the spatio-temporal distribution of the nucleation events. If these differences are removed, one obtains similar evolution across scales - from growth to fragmentation (see section A.1 for further details). This is also reminiscent of the work of Nguyen et al. (2014a), who studied the early stages of rupture in

nanometer-thick liquid-metal films. Their molecular dynamics simulations reveal that spinodal instability and nucleation mechanisms simultaneously occur within these films, indicating that these macroscopically different processes originate from a shared molecular basis.

4.5 Memory of Rupture

The probabilistic nature of film rupture process prohibits any precise prediction of the time and location of a nucleation-event, especially for a defect free surface. Perhaps surprisingly, this study uncovers a short-term window before the nucleation event where it becomes deterministic - even with a perturbation applied to the trajectories. And this sets the scene for the discussion on the state of macroscopically deterministic, microscopically stochastic (MDMS) events. For the nucleation of thin liquid films, this is the state where the first hole will nucleate in a specific bounded region Ω of space, almost surely, regardless of the number of times the scenario is repeated whereby each individual repetition produces a slight alternation of the trajectory of film evolution. In Fig. 4.3, Ω is schematically represented by the circular nucleation spot. Moreover there exists a brief time-window, Σ, shown in Fig. 4.3 as the rupture memory region, within which we can rewind the film state and still achieve nucleation in Ω. Together, the region defined by $\Omega \times \Sigma$ forms the spatio-temporal boundary for the MDMS characteristics of a film approaching its first nucleation.

To explore this temporal duration of impending rupture events, we systematically preserved the system's state at regular intervals and subsequently resumed the simulation from those instances onward. Repetition of these computer experiments, with different phase-space trajectories, highlights the inherent weak extent of 'memory' in the film-rupture process. This means that, under identical initial conditions, the time and location of rupture exhibit variability in independent simulations, except for an exceptionally narrow time interval during which the film displays deterministic behavior. Fig. 4.3 elucidates this dynamics. The top plot illustrates density fluctuations over time, with filled red symbols representing the local density at the center of a rupture site that nucleates at $t \sim 580$. The cyan curves portray local density at all other film positions, showcasing temporal fluctuations through the curve bandwidth.

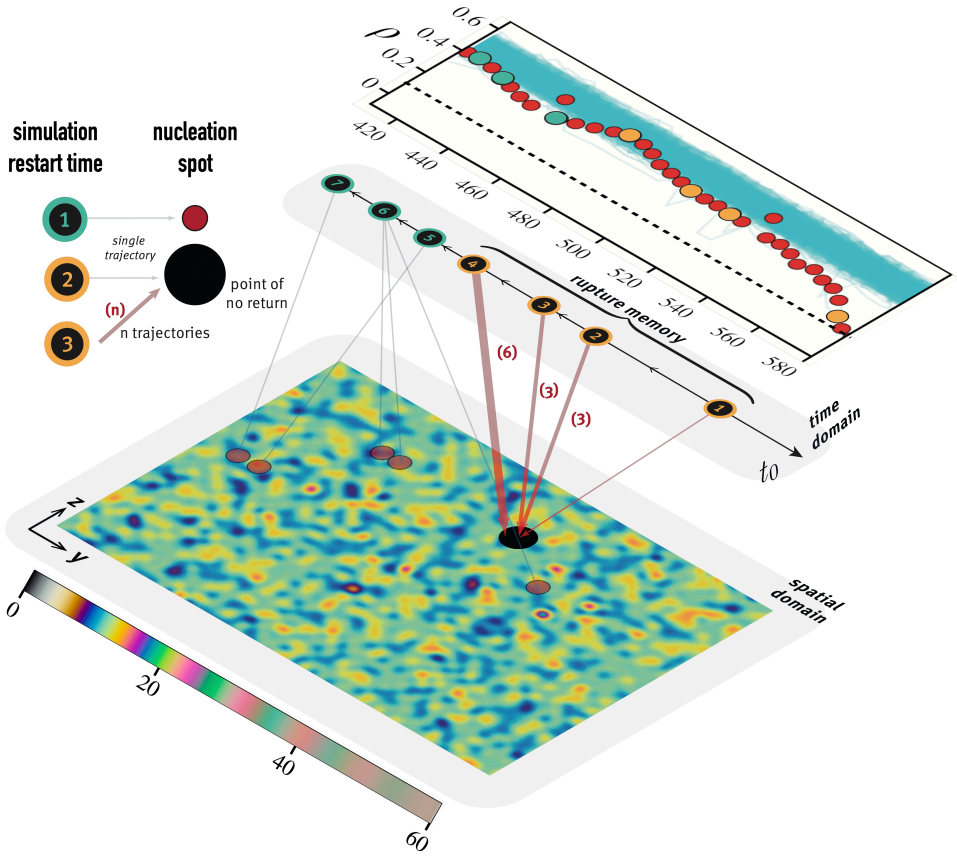


Figure 4.3: Memory of rupture: (top) temporal variation of the thickness-averaged local density. The circles corresponds to density of a location where nucleation occurs at $t \sim 580$, whereas, the cyan curves shows local density at other locations on the film which do not nucleate within the time plotted here. Several independent simulation were restarted at time $t = 418, 449, 481, 504, 520, 571$ - these time instances are marked by the circles on the time axis, and the corresponding density of the ruptured site at those time instants are marked by blue and orange circles. On the snapshot of the film at the bottom, the position of nucleation for every case is depicted either by a black circle if the location of nucleation remains the same as of the original case, or red if the film nucleates at a different location. Similarly, red lines connect nuclei when films nucleate at the same spot as the mother film, and blue lines connect otherwise. (n) shows number of independent simulations (also represented by thickness of the connecting lines), omitted if $n = 1$.

Throughout this extensive time span, despite the density of the rupture site closely following the lower boundary of the density spectrum, no abnormal deviations relative to other density profiles occur. Hence, assigning a critical lower density threshold would be inaccurate. This is supported by the observation of the density profiles at certain regions that do indeed experience significant density reduction (see the cyan density profile that approaches $\rho < 0.2$ at $t \sim 520$), they do not culminate in rupture/nucleation events.

The time instances denoted by the orange or blue circles on the density plot (and, also on the time-axis encircling the black circles) mark the moments when independent simulations were re-started. These instances are reproduced, alongside the time axis, in the lower panel, where the $y-z$ coordinates of the film are depicted, pinpointing nucleation sites represented by filled circles. Connection lines link each restart time to its corresponding nucleation location. The larger black circle designates the nucleation site of the original trajectory ($t_n \sim 580$, as displayed in the top panel's). Notably, in a simulation recommenced from an earlier state, i.e., $t_0 \sim 520$, the film still nucleated at the same spot. This consistent location remained unaltered until $t_0 > 481$. The case (re)started from $t_0 \sim 481$ is particularly important as one can identify a rise in the local density which implies that a relatively thicker area on the film can be more prone to rupture than a thinner area. To corroborate this observation, multiple independent simulations were conducted around $t_0 \sim 481$. Even when introducing minor perturbations to the initial trajectory, the film consistently underwent nucleation at the identical site. Restarting the simulation from a state earlier than ~ 480 introduced a distinct behavior, where the film undergoes nucleation at random and diverse locations and times. These stochastic nucleation sites are depicted as faint red circles in the figure, linked by blue lines to corresponding restart times. Among these latter cases, when restarting from the state at $t_0 \sim 449$, one of the cases coincidentally nucleated at the same location as the original simulation, which we regard as an incidental occurrence. A similar rewind is conducted for another case for which $t_n \sim 450$, (see section A.2), the film is observed to nucleate at a different location and at a different time, but exhibits similar characteristics with a different spatio-temporal boundary - suggesting reduced, if not complete absence of,

stochasticity (Chatzigiannakis and Vermant, 2020) within the memory-window.

MD simulations inherently incorporate an apparent stochastic element. Yet, this study reveals a striking observation: holes consistently form at the same locations across simulations. This unexpected spatial consistency in hole formation, despite different phase-space trajectories and apparent stochasticity, complements and extends the insights from prior studies (Sprittles et al., 2023; Zhao et al., 2022).

As illustrated above, local density alone cannot define the likelihood of rupture. The local energetic profiles at the nucleation site can be approximated in the following manner (Durán-Olivencia et al., 2019; Vrij, 1966a). The free energy increase, U for a film of medium 2 (liquid phase), between two media 1 and 3 (vapor phases above and below the film) is given by Vrij (1966a):

$$U(h) =$$

$$\int_{y_0}^{y_f}\int_{x_0}^{x_f}\left(\frac{\gamma}{2}\left[\left(\frac{\partial z_{12}}{\partial x}\right)^2+\left(\frac{\partial z_{12}}{\partial y}\right)^2+\left(\frac{\partial z_{23}}{\partial x}\right)^2+\left(\frac{\partial z_{23}}{\partial y}\right)^2\right]+\frac{1}{2}\frac{d^2V}{dh^2}\left(z_{12}-z_{23}\right)^2\right)dxdy \tag{4.2}$$

here, $h-h_0=z_{12}-z_{23}$, with h being the film thickness, and h_0 the mean thickness. $V(h)$ is the free energy per unit area given by $-\mathcal{H}/(12\pi h^2)$, where, $\mathcal{H}$ is the Hamaker constant, hence, $d^2V/dh^2=-\mathcal{H}/2\pi h^4$. Realizing that[†]

$$\left(\frac{\partial h}{\partial x}\right)^2\approx\left(\frac{\partial z_{12}}{\partial x}\right)^2+\left(\frac{\partial z_{23}}{\partial x}\right)^2$$

[†]

$$z_{12}-z_{23}=h-h_0$$
$$\Rightarrow\left(\frac{\partial z_{12}}{\partial x}-\frac{\partial z_{23}}{\partial x}\right)^2=\left(\frac{\partial h}{\partial x}\right)^2$$
$$\Rightarrow\left(\frac{\partial z_{12}}{\partial x}\right)^2+\left(\frac{\partial z_{23}}{\partial x}\right)^2-2\frac{\partial z_{12}}{\partial x}\frac{\partial z_{23}}{\partial x}=\left(\frac{\partial h}{\partial x}\right)^2$$

Ignoring the final term in the LHS,

$$\Rightarrow\left(\frac{\partial z_{12}}{\partial x}\right)^2+\left(\frac{\partial z_{23}}{\partial x}\right)^2\approx\left(\frac{\partial h}{\partial x}\right)^2$$

$$\left(\frac{\partial h}{\partial y}\right)^2 \approx \left(\frac{\partial z_{12}}{\partial y}\right)^2 + \left(\frac{\partial z_{23}}{\partial y}\right)^2$$

Eq. (4.2) becomes:

$$U(h) = \int_{y_0}^{y_f} \int_{x_0}^{x_f} \left[\frac{\gamma}{2}\left(\left(\frac{\partial h}{\partial x}\right)^2 + \left(\frac{\partial h}{\partial y}\right)^2\right) - \frac{\mathcal{H}}{4\pi h^4}(h-h_0)^2\right] dxdy \tag{4.3}$$

$$U = \int\int \left(\frac{\gamma}{2}\left|\nabla h\right|^2 - \frac{\mathcal{H}}{4\pi h^4}(h-h_0)^2\right) dx\, dy \tag{4.4}$$

Here, $\gamma \sim 0.5$ (Rahman et al., 2023) in reduced units. The Hamaker constant, $\mathcal{H}$ may vary depending on whether the film is supported or freely suspended, on film material, and also both on temperature and film thickness (Bhatt et al., 2002). However, the focus of this work is not on the absolute value of U, rather to examine if variation of U is indicative of rupture. Therefore, and without any loss of generality, the typical value (Israelachvili, 2011) of $\mathcal{H} \sim 10^{-19}\, J$ is adopted.

Figure 4.4 examines the thickness fluctuations and the energy landscape of a film. Panel (a) shows the variance of thickness fluctuations at site $\mathcal{R}(x, y)$ and its near-neighbors, i.e., $x \pm 3, y \pm 3$ over time. The fluctuations in thickness is evident, spikes corresponding to the nucleation events. In case of the parent simulation (which commenced at $t \sim 401$, black symbol), $\mathcal{R}(x, y)$ nucleated at $t_n \sim 571$ (empty black circle). Restarting at an earlier time also results in rupture (same point in space, different point in time) but only until $t > t_s$. If, instead $t < t_s$, denoted by the dotted vertical line, $\mathcal{R}(x, y)$ does not rupture, and nucleation occurs elsewhere (silver and gray lines, $t_n > 600$, not shown in plot) indicating an erasure of the memory of rupture.

Panel (b) shows the energetic evolution of site $\mathcal{R}(x, y)$, with $U(\mathcal{R})$ representing the local energy at site $\mathcal{R}$, As the system evolves beyond t_n the energy curves, it becomes apparent that at $t = t_s$, corresponding to the boundary of the memory window, or equivalently the saddle point that marks the edge of the attractor basin for nucleation at that point, a critical dynamical transition occurs. Within the attractor time window where rupture is destined to occur, rewinding the clock and restarting the simulation with a perturbation of the molecular trajectories leads to rupture at an earlier time but at the same place. This might suggest that the disturbance so

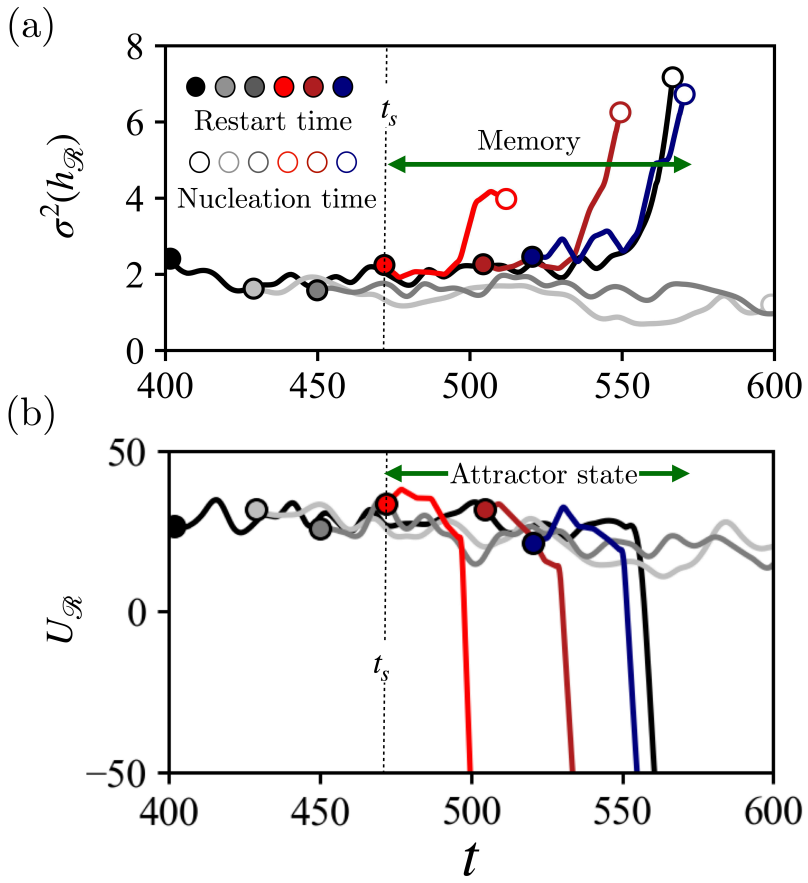


Figure 4.4: (a) Time evolution of the variance, $\sigma^2(h_{\mathcal{R}})$ of the local thickness at a site on the film, $\mathcal{R}(x, y)$ which originally nucleates at $t \sim 571$ (black line). Restarting the same simulation at earlier points, while within the memory window, results in nucleation at the same spatial location but at different points in time. Restarting earlier than t_s results in nucleation at different points both in space and time. (b) Energetic evolution of $\mathcal{R}(x, y)$ for the same cases as in panel a. In both panels, filled symbols denote the start time of the simulation, whereas, empty symbol denote time of nucleation.

caused initiates a more rapid exploration of phase space of the inherent pre-rupture structure, and a more optimal following of the path which leads eventually to the rupture event itself.

For simulations commencing left to t_s, the pathway to rupture is governed by

stochasticity; but those commencing right to it, the system appears to be already in a state of latent nucleation potential, or within a basin of attraction. As such an impending rupture event becomes deterministic. This suggests a configurational state of the molecular dynamics that relies on the intrinsic structure of the film, a notion not present in the context of fluctuating hydrodynamics, yet essential for capturing the deterministic behavior of rupture events. Notably, the gray curve (case restarted at $t \sim 450 < t_s$) exhibits a period when U is sufficiently lower, still the site does not rupture - possibly due to the absence of the right amount of fluctuations required, as such it kicks back above the threshold and does not rupture, at least within the simulation time window. The saddle point marks the onset of the memory window, signifying the transition from stochastic to deterministic rupture. The local energetics with fluctuating hydrodynamics have been very successful in predicting the onset of thermal rupture, the readers are referred to recent works of Dhaliwal et al. (2024); Sprittles et al. (2023), and the references therein. Although the deterministic rupture in the memory window did not seem to be trivially predictable by these local energies, the existence of a saddle point and a surrounding basin of attraction in the energy landscape might be valid starting point to understand rupture memory, perhaps requiring a non-linear stochastic model.

Another plausible interpretation[‡] of the probabilistic to the deterministic transition can be framed in terms of Stillinger's inherent structure theory of dynamical evolution in liquids, which has been widely applied to many aspects of liquid dynamical phenomena at the molecular level (Bagchi, 2013; Ball, 2014; Nusse et al., 1994; Stillinger and Weber, 1982). In this theory it is proposed there is a so-called 'basin of attraction' formed from all those equilibrium molecular configurations - which when quenched, instantaneously collapse into the *same* underlying or 'inherent' structure, some of which we have seen are precursors to nucleus formation. Therefore, the trajectories (re)started from different points in time, despite their microscopic randomness, are perhaps still attached to the same inherent structure and results in the same outcome. If one goes too far back in time, slight differences in the trajectory associated with the restart may cause the system to evolve in a way where it becomes associated with

[‡]The idea of relating rupture to a liquid's inherent structure originated from a series of illuminating conversations with Prof. David M. Heyes. See Fig. A.4 for a seabed analogy.

or 'captured' by another inherent structure which may not lead to a nucleus (unlike the situation before the rewind). In the present context, certain inherent structures can be viewed as acting as 'gateways' to hole formation.

4.6 Formation of a Nucleus

Fig. 4.5 (a), shows the temporal evolution of the local thickness at the center of a rupture site over non-dimensional time, $\tilde{t} = (t - t_n)/\tau_i$, where t_n is the time of nucleation, τ_i is the inertial time scale, and defined as $\tau_i = \rho h_0^3/2\gamma$. The film gradually thins over time, and once its thickness reaches ~ 10, the rate of thinning is accelerated leading to the formation of a nucleus - as seen in the shaded region of the figure. The highly resolved space-time in present simulations allow to trace back to the immediate proximity of a nucleation event to capture the formation phase of the hole (i.e., nucleus). The radial averaged local density profile of the center of a nucleus is reconstructed in Fig. 4.5 (b and c) where the initiation of local thinning is evident ahead of the rupture, i.e., at $t_{n-2\delta t}$, where $\delta t = 25$.

Upon the film's substantial perforation and the subsequent formation of a rim encircling the nucleus, expansion ensues through exponential, and linear growth rates. Regardless of the time of nucleation (and hence the initial thickness of the film), spontaneous rupture process is preceded by localized thinning, and all rupture sites inevitably undergo the fluctuations dominated thinning phase - which is noticeably accelerated as the film approaches the nucleation event (schematically shown in region 3 of Fig. 4.1).

The time of the first nucleation event, denoted as t_n, exhibits pronounced sensitivity to the film thickness, h_0. This relationship is seen in Fig. 4.5 (d), which clearly illustrates that t_n increases approximately with the third power of h_0, within the simulation statistics. Ruckenstein and Jain (1974) studied the rupture of the pure thin film free from surface active agents, and argued that the out-of-phase fluctuations at the upper and lower surfaces lead to the most rapid rupture. Considering the out-of-phase perturbations, the rupture time, τ can be related to the initial film thickness as (Moreno-Boza et al., 2020; Ruckenstein and Jain, 1974): $\tau \approx \frac{6\pi\mu\bar{h}^3}{\mathcal{H}}$, here, $\mathcal{H}$ is the Hamaker constant, and $\bar{h}$ is the average film thickness. It is problematic to measure

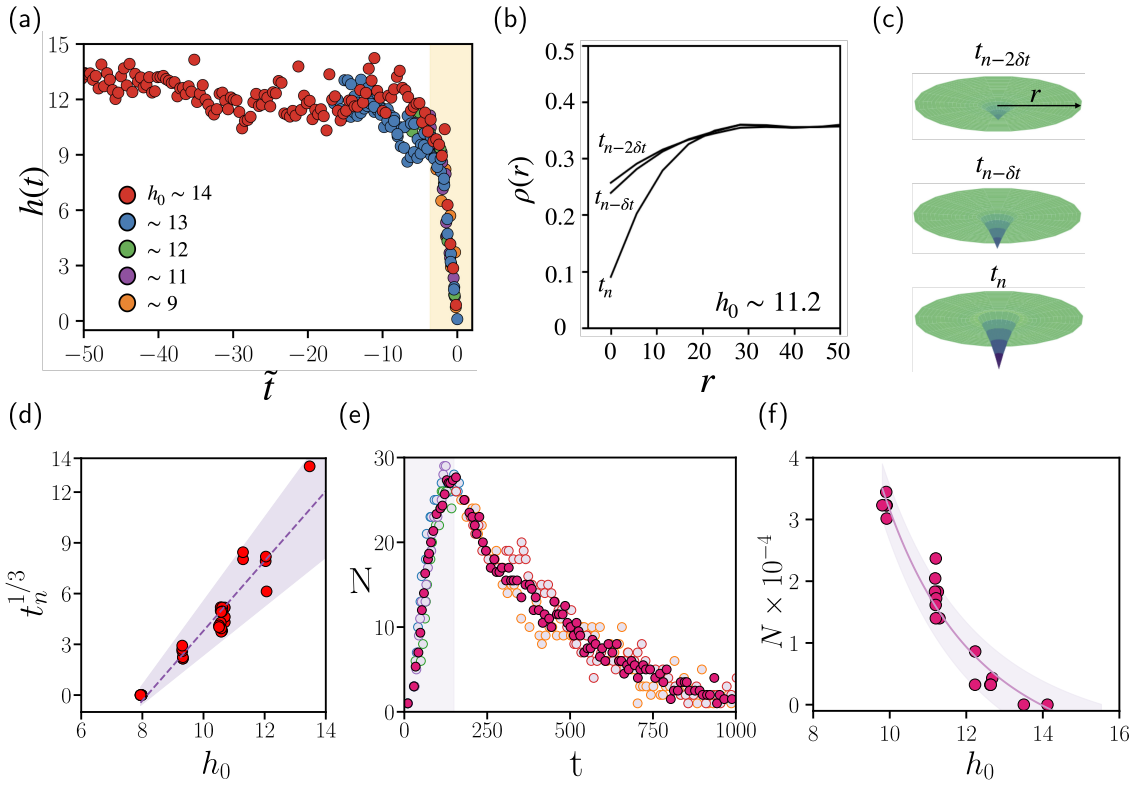


Figure 4.5: Temporal variation of the thickness of the center of a nucleus that forms at time, $\tilde{t} = 0$, where, $\tilde{t} = (t - t_n)/\tau_i$ with t_n the time of nucleation, and τ_i the inertial time scale. (b) radial (and thickness) averaged density profile around a nucleus at times closer to its nucleation for a film with $h_0 \sim 11.2$, $r = 0$ is the center of the nucleus, and $\delta t = 25$ units of MD time. (c) A full revolution of the density profiles around the axis through the nucleus-center at t = $t_{n-2\delta}$, $t_{n-\delta}$ and t_n. (d) t_n varies with the third power of the film thickness, h_0. Multiple independent simulations were carried out for each thickness. Symbols denote individual simulations, and the dashed line shows fitting to the data according to $t_n \propto h_0^3$. (e) Number of nuclei, N formed on a film of thickness, $h_0 \sim 10$ over time. Beyond the shaded region, coalescence starts (shaded region) and N starts decreasing. Faint circles show data of individual simulations, filled solid circles denote averaged data. (f) Areal density of nuclei (per MD unit area) as a function of h_0. Multiple independent simulations were conducted for each thickness. The line shows a $N \propto h_0^{-4}$ fit to the data.

an accurate Hamaker constant for thin films, and the possible dependence of this constant on the film thickness cannot be ruled out, which leads to uncertainties in the prediction of the rupture time, as does the approximation of uniform film thickness.

Figure 4.5 (e) shows the temporal evolution of the number of nuclei on a film of thickness, $h_0 \sim 10$ for three independent simulations. It is evident that for thinner films, nucleation occurs at multiple sites within a relatively short time period, and the film quickly enters the coalescence regime, and the nuclei start to merge into bigger nuclei. Figure 4.5 (f) shows how the areal density (maximum number of nuclei divided by the lateral area of the film) of the nuclei decreases with increasing film thickness, just as was carried out in a study of liquid crystal films (Nguyen et al., 2014a). The solid line denotes a fit to the data according to the scaling law, i.e., $\rho_N \sim h_0^{-4}$, proposed in earlier theoretical and experimental studies (Reiter, 1992; Sharma and Reiter, 1996). Note here, these spontaneous rupture sites (and the thinnest parts in the film) emerged at varied locations across the film, and did not cluster only around the film edge as reported in a recent experimental study on colloidal films (Shah et al., 2023).

Fig. 4.6 (a) illustrates the initial exponential growth of a nucleus on a film of thickness, $h_0 \sim 14$ - one may not obtain such growth behavior unless the flow field is radially resolved (Brenner and Gueyffier, 1999). To confirm the short time dynamics, multiple (10) independent simulations were run for a shorter time window with higher resolution in time. Once a hole is formed, its growth dynamics is governed by the balance between the surface force, and the momentum of the liquid mass that accumulates around it forming a rim-like structure (Culick, 1960; Taylor, 1959). However, the film downstream the rim remains largely undisturbed (Culick, 1960; Redon et al., 1991; Taylor, 1959). This is shown in the radial averaged velocity field of an expanding hole in Fig. 4.6 (b). In presence of multiple rupture sites, classical theories for growth dynamics are locally applicable; however, growth is highly effected by coarsening-induced frustration. While hydrodynamics might intuitively lead to the movement of the different features of the film, the absence of external forces, or surface tension gradients due to surfactants renders global displacement of holes improbable within the studied length and time scales. Exceptionally, as illustrated in Figure

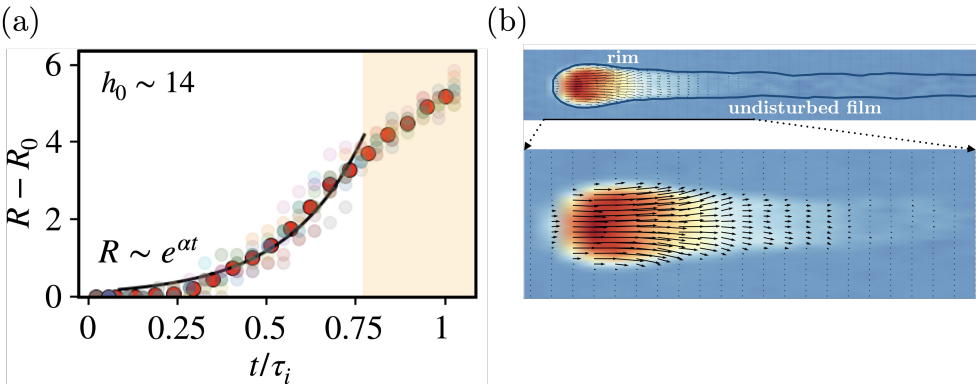


Figure 4.6: (a) A nucleus grows exponentially at the very early stage which is later followed by linear growth. The faint symbols are data from 10 independent simulations, and the solid red symbols denote data averaged over the individual simulations. R_0 denotes initial radius at time, t_0, and τ_i is the inertial time. (b) Velocity vectors and color map show fluid motion within, and in the close proximity of the rim of a growing hole. Downstream of the rim, the film remains mostly stationary.

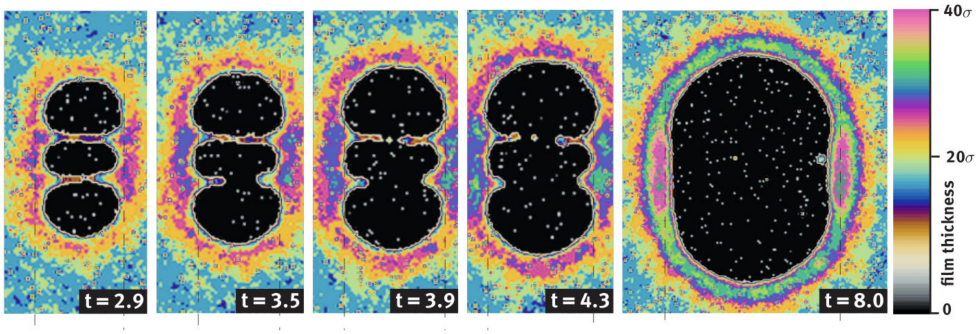


Figure 4.7: Coalescence of frustrated nuclei, reminiscent of the experimental study of Dolganov et al. (2020) using free-standing smectic films.

A.5 (b), a larger nucleus can displace a smaller one, subtly indicating that hydrodynamic effects, though minor, are accounted for in the molecular dynamics simulations.

4.7 Frustration and Coalescence

While the growth of an isolated nucleus is well understood through the seminal works of Taylor and Culick (Culick, 1960; Taylor, 1959) and subsequent detailed studies (Frankel and Mysels, 1969; Keller, 1983; McEntee and Mysels, 1969; Savva and Bush, 2009), a more commonplace observation is of a film with multiple rupture sites raising a natural question as to how these sites grow and interact. The absence of neighbors, or equivalently the consideration of infinite liquid films in previous studies (Savva and Bush, 2009; Sünderhauf et al., 2002) prohibited the observation of any interaction between propagating rupture sites, and was only realized when the edge effect was accounted for (Deka and Pierson, 2020b). If one considers two neighboring nuclei on a film, these may exhibit three distinct types of behavior in stages: (i) individual uninterrupted growth until when the nuclei come to close proximity of each other, (ii) disturbed growth due to the presence of the neighbor leading to (iii) delayed coalescence. The first stage is predominantly governed by surface tension dynamics. At the second stage, surface tension favors the growth of the nuclei, but coarsening of the bridge between the neighbors retards growth. The third stage requires drainage of the liquid bridge, followed by subsequent thinning and rupture.

The thickness of this liquid bridge between two neighboring nuclei is notably greater if the nuclei have undergone sufficient growth over time before coming close to each other. This arises because the liquid particles from the nuclei accumulate in the surrounding rim, forming a barrier that impedes merging. (Refer to the A.3 for a scenario where a larger nucleus opts to displace a relatively smaller nucleus rather than coalescing with it.) However, there are situations where nuclei have expanded extensively and multiplied to the extent that they encounter space limitations, compelling coalescence as the sole energetically favorable course of action to continue to evolve. This phenomenon is illustrated in Figure 4.7, results from molecular dynamics simulations depict the temporal evolution of three artificially generated nuclei, capturing their initial growth, coalescence, and subsequent expansion beyond coalescence.

Fig. 4.8 (a) shows the time-evolution of the radii of three synthetic nuclei (by 'synthetic' we mean non-spontaneous nucleus which was induced by applying an expo-

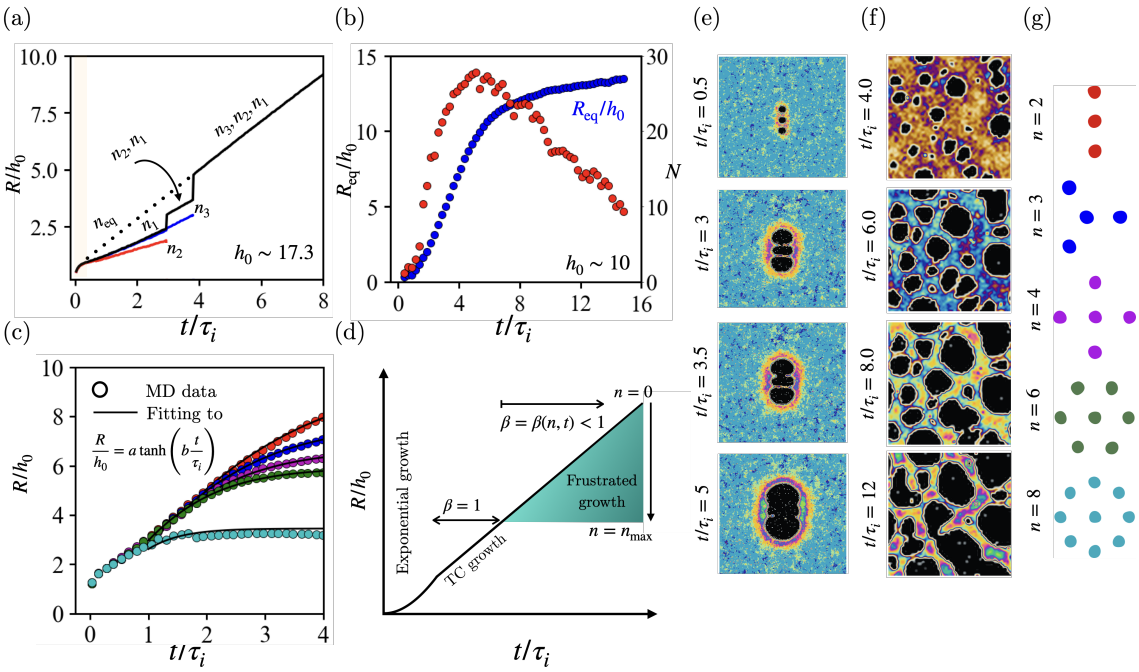


Figure 4.8: (a & e) Growth of three synthetic nuclei (n_1, n_2, n_3) on a film of thickness, $h_0 \sim 17.3$. Snapshots at different instants are shown in panel (e). After a brief period of initial transients (Rahman et al., 2023), each nucleus undergoes a phase of linear growth. While all nuclei initially expand at the same rate, the central nucleus experiences hindered growth due to interactions with the adjacent side nuclei, resulting in deceleration (red line). In contrast, the two side nuclei continue their growth at a consistent pace (black: n_1, blue: n_3). At $t/\tau_i \sim 3$, n_2 coalesces with n_1, continuing its growth as $n_{c,1,2}$, while n_3 maintains separate growth rate until its coalescence at $t/\tau \sim 4$. The newly merged nucleus ($n_{c,1,2,3}$) then resumes unrestrained growth. The dashed line represents the growth trajectory of an equivalent nucleus from the initiation of the linear regime. (b & f) Growth of the equivalent nucleus (blue circles, left y-axis) in a film of thickness $h_0 \sim 10$, where multiple holes spontaneously nucleate - as shown in panel (f). Red circles in (b) represent the number of nuclei, N (right y-axis). (c & g) Effect of the number of neighbors (n) on the growth of an expanding central nucleus surrounded by n neighbor nuclei as shown in panel (g), solid lines in (c) denote fitting to the data. (d) Schematic representation of neighbor-effect on the growth of a nucleus. Every case was independently run for at least three times with standard deviation less than 3%.

nential force − mimicking the poking of a film in experimental studies (Bird et al., 2010; Savva and Bush, 2009) − in an otherwise stable film, see: methodology) before and beyond coalescence (few representative snapshots are shown in panel e). Initially the nuclei are distant from each other and a very short term exponential growth is followed by the Taylor-Culick linear regime (Rahman et al., 2023; Savva and Bush, 2009) - the discussion pertinent to this constitute the next chapter of this thesis. However, and as depicted by the red line, the growth of the central nucleus (n_2) is affected by the presence of the two expanding side-nuclei (n_1, n_3) until it coalesces with one of them.

Beyond coalescence, the combined nucleus (n_1 and n_2) maintains linear growth. It is observed from the slopes of the blue (single nucleus, n_3) and the black (coalesced n_1, n_2, i.e., $n_{c,1,2}$) lines, that the growth rate of the single nucleus, n_3 and that of the coalesced nucleus, $n_{c,1,2}$ is the same. After the final coalescence at around $t/\tau \sim 4$, a slightly steeper slope (of the black line, $n_{c,1,2,3}$) is observed, this is because the growth is no longer restrained by any surrounding nucleus and there is sufficient space for expansion (the film is larger in lateral dimension than in panel e which shows only the area surrounding the nuclei). Notably, the dashed line denotes the equivalent radial growth of the three nuclei ($R_{\text{eq}} = \sqrt{A/\pi}$, with $A = \sum_{i=1}^{3} A_i$) which as well, captures the growth rate of the coalesced nuclei, and thus proves to be a representative measure. More importantly, and in agreement with previous conclusions (Herminghaus et al., 1998; Jacobs et al., 1998), this implies that the growth of a coalesced nucleus can be extrapolated to the initial nucleation time, provided that growth is hindrance free. Jacobs et al. (1998) carried out a similar extrapolation in time for an estimation of the nucleation time, but without considering any temporal behavior of the nucleus distribution in spinodal process, and any dynamical instability thereof. Herminghaus et al. (1998) also proposed the use of nucleus diameter as a 'clock' for the rupture. However, we will shortly see that such a straightforward extrapolation in time is valid only for a few special cases, and generally imprecise, if not prohibitive.

Figure 4.8 (b) provides insight into the growth dynamics of the equivalent nucleus radius, R_{eq}/h_0 (depicted as red circles corresponding to the left y-axis), and the number of nuclei (illustrated as blue circles corresponding to the right y-axis) for

a relatively thinner film ($h_0 \sim 10$) that ruptures spontaneously; panel (f) presents representative snapshots of this process. In panel (b), the reference point $t/\tau_i = 0$ denotes the time of the first nucleation event. The number of nuclei (blue circles) initially rises during the nucleation phase and subsequently declines from $t/\tau_i \sim 5.8$, indicating the transition to the coalescence regime. The red circles trace the time evolution of the equivalent nucleus radius, revealing a linear growth during the nucleation regime, followed by a phase of quasi-stagnation where R_{eq} experiences marginal increments. This contrasts with the observations in panel (a) where the growth rate increased after coalescence. The underlying reason for this divergence in growth patterns lies in the available space for expansion. For the case in panel (a), the coalesced nuclei have sufficient room to expand, as exemplified by the snapshot at $t/\tau_i = 5$ in panel (e). However, for the case in (b), the coalescence of multiple nuclei restricts their individual expansion due to spatial constraints, reminiscent of the middle nucleus in the former case. These insights unveil two pivotal aspects of rupture: (i) the growth rate of a nucleus is contingent upon its size and position relative to other nuclei on the film, and (ii) if two nuclei coalesce, the post-coalescence growth rate of the amalgamated nucleus mirrors that of individual nuclei, provided hindrance-free expansion persists. This is feasible only when two closely situated nuclei merge during an early stage of the film rupture process, namely before the onset of the coalescence regime. Our observations underscore that a straightforward temporal extrapolation, as discussed earlier, encounters limitations without comprehensive details regarding nucleation dynamics and the spatio-temporal arrangement of the nuclei.

Figure 4.8 (c) demonstrates how the number of neighbors impact the growth of a central (synthetic) nucleus surrounded by n neighbors. The initial radii of all the nuclei, $R(t = 0)$, and the initial center-to-center distance between the central and any of the neighbor nuclei were kept constant for all cases considered (the initial conditions are shown in panel g, color of the nuclei in panel g correspond to the symbol color in panel c). As n increases, the growth starts deflecting from the linear behavior. One can observe that at $n = 6$ (green circles), the growth curve reaches nearly a plateau - meaning the neighbors surround the central nucleus from all sides inducing sufficient wall effect to suffocate further growth. If n is increased beyond 6, the initial

growth is shortened and the growth of the central nucleus soon ceases. The solid lines in panel (b) corresponds to fitting of the MD data to an equation of the form, $R/h_0 = a \tanh(\mathrm{bt}/\tau_\mathrm{i})$, where a and b are fitting coefficients.

An expansion of the fitting equation suggests that the frustrated growth can indeed be captured through higher order corrections to the Taylor-Culick law of retraction, i.e., $R/h_0 = c_1 (R_\mathrm{TC}/h_0) - \mathcal{O}(\chi^n)$, here, R_TC is the unrestrained radius of the nucleus at time t, and c_1 is the coefficient of the expansion whose magnitudes is governed by the frustration of growth, and $\mathcal{O}(\chi^n)$ denotes higher order terms in the expansion. The different stages of nucleus growth including the above mentioned frustrated regime is schematically presented in panel (d). The early-time exponential growth is followed by the Taylor-Culick linear growth, ($U = \beta U_\mathrm{TC}$), with $\beta = 1$. Upon sufficient expansion, when a nucleus comes into close proximity of its neighbors, the growth is slowed ($\beta < 1$). The extent to which the growth is frustrated depends on the number of neighbors. As $n \to n_\mathrm{max}$ (see section A.3 for further details), the frustration is maximized and growth is ceased.

As time unfolds, the resulting grown-up patterns show striking similarity with patterns observed in earlier experimental studies. Figure 4.9 compares some of the patterns observed in the present investigation with the experimental findings by Thiele et al. (1998). The left column on panel (a) presents the initial stages of synthetic nuclei, which are allowed to evolve over time, the corresponding later stages are displayed on the right column of the panel. Panel (b) shows similar looking patterns found through scanning force microscopy (SFM) of collagen film rupturing on a solid substrate, revealing a diverse array of rupture sites with varying shapes and sizes. This coherence between the present simulations and previous experimental observations underscores the effectiveness of molecular dynamics (MD) simulations in capturing the spatio-temporal dynamics of liquid film rupture.

4.8 Summary

To summarize, the present investigation unravels the complete life cycle of a black film, delving into its inception, evolution, and ultimate fragmentation with intricate

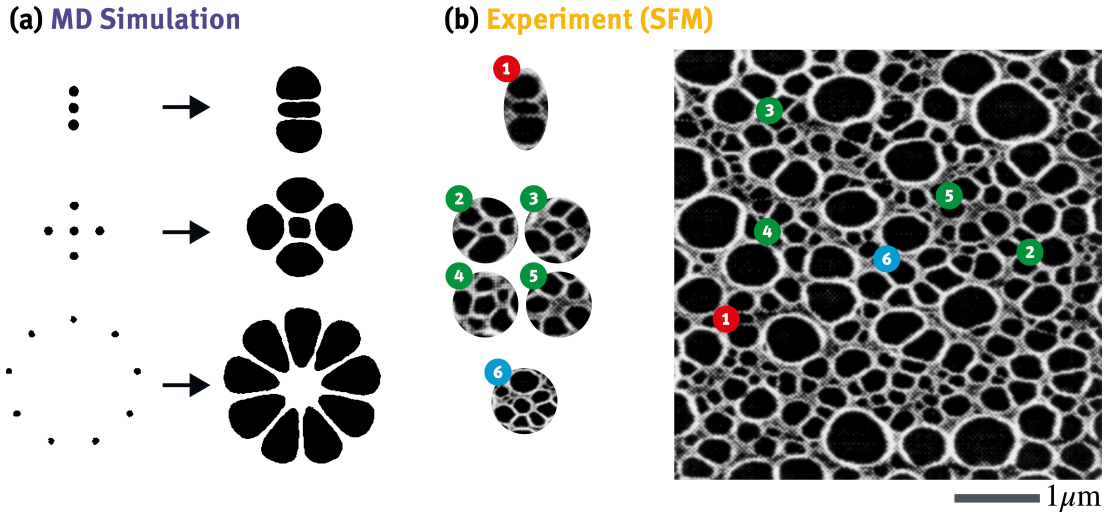


Figure 4.9: (a) Patterns observed in current investigations through varied synthetic perturbation. The left images depict the initial conditions, while the right images capture snapshots during the later stages of rupture. (b) The patterns observed in panel a, are compared to the those observed in the scanning force microscopy (SFM) image (adapted from panel c of Figure 1 in Thiele et al. (1998), with permission from the authors and the publishers) of a collagen film on a solid substrate. Similar looking patterns in MD and experiments are marked by identical numbers.

insights into these phases. Findings contrast the conventional understanding of rupture in pure films, revealing that the unfolding of film morphologies – commonly characterized as spinodal and nucleation dominated rupture – are broadly analogous except for their respective timescales.

The highly resolved time in this investigation discloses a 'film-pinching' phase preceding the exponential growth of rupture. A brief but discernible window of determinism, which emerges amidst the stochastic nature of rupture dynamics, indicates the liquid's inherent structure as the gateway to predicting rupture. Following the evolution of the nucleated sites through exponential and linear growths, the late stage is marked by considerable frustration in growth, resulting in delayed coalescence and coarsening. In essence, this study sheds light on the intricacies of black-film rupture dynamics, providing valuable insights into the underlying mechanisms governing

this phenomenon. These not only expand the fundamental understanding of thin film behavior but also open doors to potential applications in various scientific and technological domains.

The oldest, shortest words - 'yes' and 'no' - are those which require the most thought.

Pythagoras

5

Thin Film Rupture: An Expanding Nucleus

The retraction of thin films, as described by the Taylor-Culick (TC) theory, is subject to widespread debate, particularly for films at the nanoscale. This study employs non-equilibrium molecular dynamics simulations to explore the validity of the assumptions used in continuum models, by tracking the evolution of holes in a film. By considering a locally varying surface tension at the front of the retracting film, this study reconciles the original theory with simulation to recover a corrected TC speed valid at the nanoscale*.

*A version of this chapter has been published as Rahman, M.R., Shen, L., Ewen, J.P., Collard, B., Heyes, D.M., Dini, D. and Smith, E.R., 2023. Non-equilibrium molecular simulations of thin film rupture. The Journal of Chemical Physics (Communications), 158 (15).

Codes to reproduce the data are publicly available at:
https://github.com/MuhammadRRahman/Thin-Film-Rupture-NEMD.

5.1 Introduction

Any rupture event must start at the smallest scale, therefore, molecular dynamics is an ideal technique to realize the origins of this process. It provides the full picture of a fluid down to the atomic interactions; and the interface dynamics, surface tension and viscosity emerge as outputs from the simulations. Hence, many fluid properties have been successfully studied by molecular dynamics. Koplik and Banavar (2000) used this technique to show the origins of dewetting, alongside the studies of film breakup (Koplik and Banavar, 1993; Zhao et al., 2019), boiling and nucleation (Diemand et al., 2014) and a range of cases (Kadau et al., 2010; Todd and Daivis, 2017). Kono et al. studied a two-dimensional film breakup with MD, and observed temperature rise due to rapid rupture which would cause a decrease in surface tension.

In this chapter, the full three-dimensional film breakdown is modeled, and all possible contributions from the atomic scale systematically outlined. Using local pressure measurement techniques, interface tracking and dynamic time-evolving mappings, local surface tension is calculated. This uncovers the complete picture of surface force and interface shape, putting the thermal effects in context and exposing other key factors contributing to the dynamics. The TC model does not take into account any surface-species and their contributions to the surface properties of the film (Manikantan and Squires, 2020; Tammaro et al., 2021). By construction, the film investigated in this work is pure in nature, and hence, closest to the TC model. Present work thereby tests this model by removing external factors and shows that the classical theory fails for molecularly thin films even in the absence of surface active agents; and only when certain atomic-scale corrections are made, TC equation can successfully predict the retraction process for films with thickness down to a few nanometers.

5.2 Simulation Details

The simulation methodologies employed in the studies presented within this chapter largely mirror those detailed in Chapter 4. In an effort to reduce redundancy, this section will offer a succinct overview of the simulation process, focusing exclusively on aspects that are unique to the discussions at hand.

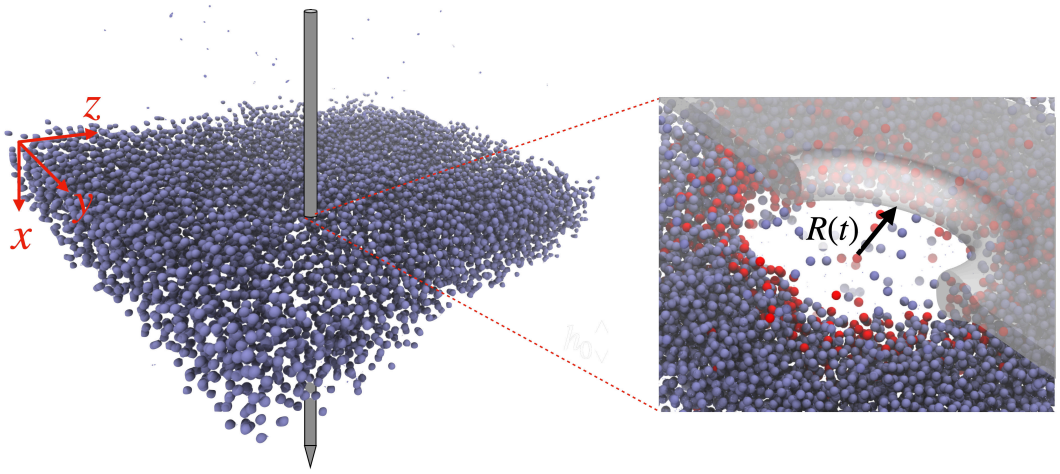


Figure 5.1: Thin film retraction. Computational domain considered for this study. A hole is nucleated at the center of the film in the yz plane. A cylindrical needle schematically shows the hole-poking process. Zoomed view of the hole: atoms in red denote the atoms initially in the hole at $t = 0$ that are displaced; faint schematic shows an idealization of the rim surrounding the hole which borders the unperturbed film.

All films investigated in this chapter were modeled using a Lennard-Jones (LJ) fluid simulated in Flowmol (Smith, 2013). The initial simulation domain was a cubic box of dimensions $L_x = 76.19$ and $L_y = L_z = 609.56$ in LJ units, with periodic boundary conditions applied in all directions. These dimensions correspond to $\approx$ 207 nm wide films with $h_0 < 5$ nm. Note, for argon, $\sigma = 0.34$ nm (Frenkel et al., 1996). The system was allowed to equilibrate until a stable liquid−vapor coexistence was established. This was run in the canonical (NVT) ensemble using a Nosé-Hoover thermostat (Hoover, 1985; Nosé, 1984). The schematic in Fig. 5.1 (a) shows the system modelled in this study where all atoms (≈ 3.54 million) are identical, forming a central liquid film coexisting with surrounding vapor at equilibrium. After equilibrating the film at $T = 0.78 \pm 0.03$ in the canonical ensemble (NVT), a hole of initial radius, R_0 was induced in the YZ plane of the otherwise stable film. Two separate hole-making techniques were employed, (i) cut-holes: where molecules within a circular region of radius R_0 were randomly deleted to achieve a target vapor density, $\rho_{h,0}$ within the

hole, and (ii) poked-holes: where an external force in the direction normal to the film, as in Eq. (5.1), was applied to mimic the popular experimental procedure of puncturing a film (Bird et al., 2010; Oratis et al., 2020; Savva and Bush, 2009).

$$F_{\text{ext.}} = \begin{cases} F\left(1 + \mathrm{e}^{-1/r^2}\right) & r \leq R_0 \\ 0 & \text{otherwise,} \end{cases} \tag{5.1}$$

where, R_0 is the target initial radius of the hole. In case of poked holes, the forcing time was only a few hundred steps to confirm that a stable hole (or, nucleus) is created. While cutting the hole, a target density $\rho_{h,0} = 0$ was specified within a circular region of radius, $r = R_0$. The effect of the target density $\rho_{h,0}$ is tested by setting it to different values in the range of $[0, 0.025]$, however no noticeable differences in the film density, or in the overall dynamics were observed. In all the cases reported, both cut-holes and poked-holes, the average density of the liquid film is found to be 0.7 ± 0.01.

Upon equilibration and puncturing, the system was then set to evolve in the micro-canonical ensemble (NVE) and R was measured over time. The inset in Fig. 5.1 (a), shows the liquid atoms surrounding an expanding hole. Displaced atoms (in red) from the hole collect around the hole to form a rim. The radial-averaged film extracted from MD data, in panel (b), shows its temporal evolution - with simplified schematic in panel (c). In order to reduce the computational cost in simulating the relatively large systems, a cut-off radius, $r_c = 2.5$ is used. Although a smaller cut-off radius results in a smaller surface tension; accordingly the retraction rate should similarly scale down. However, this should not impact the overall retraction dynamics. Near-zero densities are observed inside the hole.

To ensure that the periodic boundary does not affect the statistics (Pannuzzo et al., 2014; Seveno et al., 2013; Watanabe et al., 2022), the growth dynamics for film with lateral dimensions (in LJ units) of (i) 304.78×304.78 with ~ 0.88 million particles, (ii) 609.56×609.56 with ~ 3.54 million particles, and (iii) 1219.12×1219.12 with ~ 14.1 million particles, are tested. For (i), the hole soon reaches the film boundary giving a shorter time-window for the rupture speed to reach a plateau, and (iii) demands considerably higher computation time while producing similar statistics as of

(ii). As such, all reported cases are simulated for the lateral dimension of (ii), and the tracking of the hole-evolution was stopped before the hole radius grew upto one-third of the domain. Unless otherwise stated, throughout this study, each reported case has been averaged over at least three independent simulations.

5.2.1 Selection of Film Thickness

The inherent instabilities in ultra-thin films, owing to the long range disjoining forces and the mechanical or thermal perturbations (Debrégeas et al., 1998), make the examination of the rupture process challenging. Surface deformations arising from thermal motion increases the likelihood of spontaneous rupture (Ivanov et al., 1970; Vrij, 1966b; Vrij and Overbeek, 1968). Therefore, to find a stable, and computationally tractable case, films with a range of thicknesses were tested without applying any external perturbation.

To capture the growth dynamics of the induced holes, first films are examined with a wide range of thicknesses to ensure that the selected film does not rupture on its own. Substantial increase of film stability (i.e., exponential increase of natural rupture time) is observed with increasing thickness. To study the hole-growth dynamics, an initial film thickness, $h_0 \sim 14$, is selected which allows sufficient time when the film would not spontaneously break. As such the growth dynamics of the induced hole can be considered free from any effects otherwise caused by the instability of the film.

5.2.2 Effect of Initial Conditions

To ensure that the films under investigations are not inherently unstable, a range of film thicknesses were examined. In addition, the effect of initial nucleus radius was thoroughly tested and the late-time growth dynamics was found to be independent of R_0 With all other parameters unchanged, Taylor-Culick equation suggests an inverse dependency of the retraction speed on the film thickness, h_0, i.e., $U \propto 1/\sqrt{h_0}$. This is evident in Fig. 5.2 (a), which plots $R(t)$ with time for $h_0 \sim 14$ and ~ 26. The effect of the initial radius of the induced holes are examined with different radii, i.e., $R_0/h_0 \sim 0.4, 0.8$ and 1.2 in Fig. 5.2 (b). Irrespective of R_0, holes attain same terminal speed. Indeed, for lower $\mathrm{Oh} = \mu/\sqrt{\rho\gamma h_0}$, the relatively shorter timescale involved to

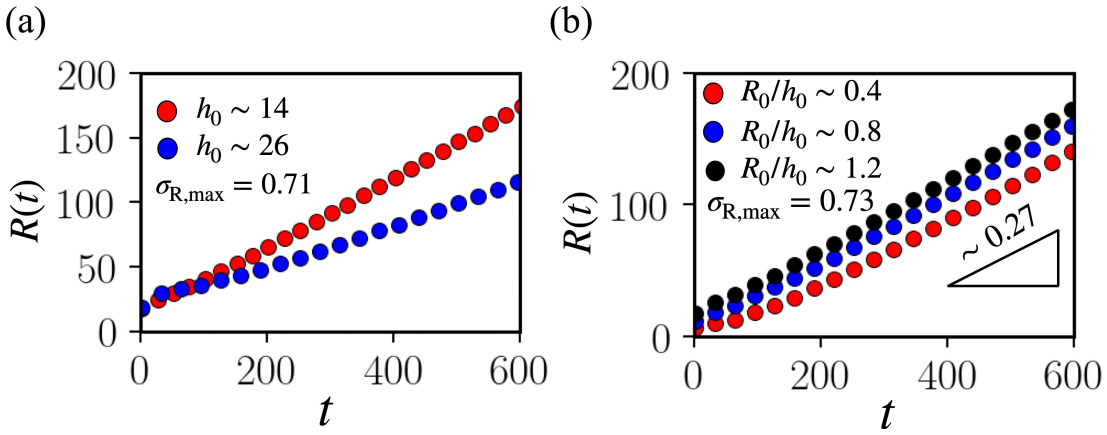


Figure 5.2: (a) The growth rate (Taylor-Culick speed) of an expanding hole decreases for thicker films. (b) Terminal retraction rate is independent of the initial hole radius. In both panels, $\sigma_{R,max}$ denotes the maximum standard deviation across three independent simulations.

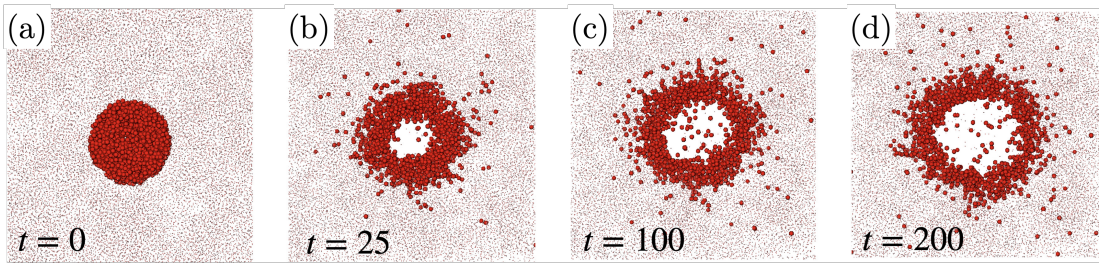


Figure 5.3: Formation and growth of a spontaneously nucleated hole, (a) before nucleation, (b-d) as the hole expands. Atoms displaced from within the hole of panel (d) are colored in red in each of the panels, remaining liquid atoms are faintly drawn. The displaced atoms are collected in the rim surrounding the hole as it grows. Note, these panels show only a portion (∼one-third) of the film in the close vicinity of the growing hole.

approach the terminal speed minimizes any effect of initial radius (Savva and Bush, 2009).

5.3 Nucleus Formation

Starting from initial hole formation (Fig. 5.3), through a short-time exponential regime, the rate of film retraction eventually reaches a constant speed which can be shown to match TC when the local changes in shape and in surface tension are accounted for. For systems at macroscopic length scale, growth of holes with an initial radius, $R_0 < h_0$ is not energetically favoured, i.e., an open hole closes (Taylor and Michael, 1973). Hence, earlier experiments or numerical investigations (McEntee and Mysels, 1969; Pandit and Davidson, 1990; Sanjay et al., 2022; Savva and Bush, 2009) on sheet retraction considered an initial hole dimension satisfying, $R_0 \gg h_0$. Additionally, continuum assumptions require long-wave approximations to describe the rupture process which is valid for h_0 much larger than the atomic scale (Vaynblat et al., 2001). However, in the limit of a few nanometers thickness (essentially Newtonian black films), the disjoining force acts as a destabilizer opposing the stabilizing effect of surface tension, and therefore, becomes responsible for the puncture of the film (Neél and Villermaux, 2018; Villermaux, 2020). At this scale, MD is the only appropriate tool to scrutinize the hole opening process. It was observed that $R_0 \gg h_0$ no longer remains an essential requirement for holes to expand. This agrees with the seminal study of Koplik and Banavar (2000), where the authors reported that for any dry patch larger than a few molecular diameters, the separated molecules suffer from mutual interactions, and the hole always grows.

The hole creation technique may invoke slight differences to the initial conditions, but any difference rapidly ceases (Frankel and Mysels, 1969). This is confirmed by applying two separate techniques to create holes, by (i) deleting atoms from a circular region of radius, R_0, or (ii) applying a small radially decaying force for a short time that models poking a film (Mandracchia et al., 2019; Oratis et al., 2020). Henceforth, these two types will be referred to as cut- and poked-holes, respectively.

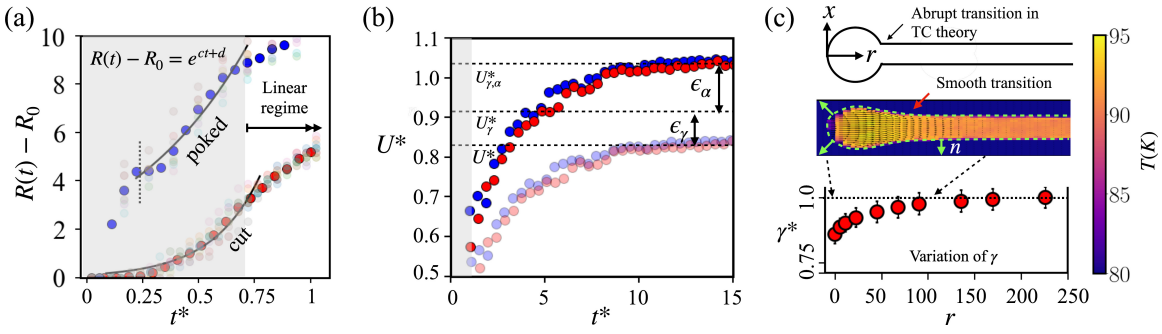


Figure 5.4: Retraction regimes and correction to Taylor-Culick speed. (a) Short-term nonlinear retraction of film for cut- and poked-holes with initial thickness is $h_0 \approx 14$, time is non-dimensionalized by the inertial time scale, i.e., $t^* = t/\sqrt{\rho h_0^3/2\gamma}$. Faint and solid symbols denote, respectively, data from individual simulations, and data averaged over 10 simulations. Solid line is an exponential fit to the data of the form: $R(t) - R_0 = e^{ct+d}$. For the poked cases, a brief transitory behavior is seen before the exponential regime (left to the vertical dotted line). (b) Retraction velocity (blue: poked-, red: cut-holes) normalized by the TC speed, $U^* = U/U_{\mathrm{TC}}$ with 2% standard deviation. Faint symbols denote cases where the classical U_{TC} is used, whereas, solid symbols denote cases where U_{TC} is corrected considering the local surface tension (U^*_γ), and the existence of a transition regime ($U^*_{\gamma,\alpha}$). $\epsilon_{\gamma,T}$, $\epsilon_{\gamma,\kappa}$ and ϵ_α denote, respectively, various corrections arising from the local variation of surface tension due to temperature, and curvature, and because of the existence of the transition regime. In panels a and b, the non-linear growth region is shaded. (c) The schematic in the top-panel shows an idealized retracting film. The mid-panel sheds molecular insights where a transition region is present between the rim and the unperturbed film. Green arrows show the directions normal (n) to the local film surface. Color map shows radial-averaged instantaneous temperature field with velocity vectors (black arrows) overlaid. The bottom panel shows the local to global (time-averaged) surface tension ratio, ($\gamma^* = \gamma_r/\gamma$) against distance, r from the tip of the retracting film.

5.4 Short-Term Retraction

At the onset of retraction, an exponential growth for a short period of time is observed, which converges to a linear terminal speed at later times. Fig. 5.4 (a) portrays this short-term hole expansion for cut- and poked-holes. In agreement with the observations in (Debrégeas et al., 1995; Masson and Green, 2002), it is evident that the

early-time hole growth shows an exponential behavior, i.e., $R(t) - R_0 = \exp(ct + d)$, where c and d are fitting parameters. While in (Debrégeas et al., 1995), the short-term growth was ascribed to the viscoelastic effects, it was confirmed to be a generic feature of circular hole retraction (Savva and Bush, 2009), and was also accredited to the initial shape of the puncture (Roth et al., 2005; Savva and Bush, 2009).

5.5 Taylor-Culick Retraction

The lone acting force that drives the film retraction process, i.e., the surface force, F_γ must be balanced by the inertia of the mass, m collected in the rim. When this dynamic balance is attained, the film retracts with a constant velocity, U_{TC}. Note, for smaller Oh, this assumption of uniform velocity inside the blob becomes invalid (Pierson et al., 2020). The surface force, F_γ can be expressed as:

$$F_\gamma = 4\pi R(t)\gamma \tag{5.2}$$

On the other hand, the change of momentum, P of the accumulated mass is:

$$\frac{dP}{dt} = U_{\mathrm{TC}}\frac{dm_h}{dt} \tag{5.3}$$

As the liquid from the hole is accumulated in the rim, the continuity equation gives: $dm_h/dt = 2\pi\rho R(t)h_0 U_{\mathrm{TC}}$. Using this expression and equating (5.2) and (5.3) yields: $4\pi R(t)\gamma = 2\pi\rho R(t)h_0 U_{\mathrm{TC}}^2$, and the Taylor-Culick speed can be expressed as:

$$U_{\mathrm{TC}} = \sqrt{\frac{2\gamma}{\rho h_0}}. \tag{5.4}$$

Beyond the short-term exponential regime, the retraction velocity approaches a plateau - the constant TC speed (Savva and Bush, 2009). This is shown by the faint symbols in Fig. 5.4 (b) for cut- (red) and poked-holes (blue). Retraction speed, U is measured over 50 consecutive time-steps, and is non-dimensionalized by U_{TC} from Eq. (2.7) with $\phi = 2$, i.e., $U^* = U/U_{\mathrm{TC}}$. Evident from Fig. 5.4 (b), U_{TC} is appreciably faster than the measured speed ($U^* \approx 0.8$), that is MD predicts a speed which is only 80% of the Taylor-Culick prediction. This is not unexpected, and documented in the literature (McEntee and Mysels, 1969; Müller et al., 2007; Petit et al., 2015; Tammaro

et al., 2021; Trittel et al., 2013). Notably, McEntee and Mysels (McEntee and Mysels, 1969) studied the retraction of soap-films with a wide range of thicknesses. In their experiments, the retraction speeds for films of thickness smaller than 100 nm were found to be substantially slower than U_{TC}, requiring $\phi \approx 0.7$. U_{TC} is rather closer to our measured speed requiring $\phi \approx 1.35 \pm 0.05$ for $h_0 \approx 4.75$ nm. However, having the effects of surfactants and visco-elasticity (Vrij and Overbeek, 1968) completely eliminated in the present study (by considering pure film), why the TC theory still fails to estimate the retraction rate is explored now.

A number of factors, i.e., temperature variation due to internal heat generation, curvature effects and viscous contribution (Pierson et al., 2020) might play a critical role in slowing down the retraction. Although viscosity does not appear in Eq. (2.7) and therefore, does not affect the terminal speed, its relative importance to the surface tension decides the length over which the film is disturbed, and how the momentum is distributed through the film(Savva and Bush, 2009). This is often characterized by the Ohnesorge number, $\mathrm{Oh} = \mu/\sqrt{\rho\gamma h_0}$, which is moderate ($\approx 0.8$) for the present case. The dynamics at higher Oh could have been explored by simulating a significantly thicker film (also larger in lateral dimension to have sufficient time for the growth of the hole) than in the current study. However, we chose not to pursue this due to the substantial computational resources that would have been required.

5.6 Surface Tension Modulation by Temperature Rise

Adjusting the value of ϕ marries the theoretical estimate with the measured speed, but it does not necessarily explain the underlying physics responsible for the slower retraction. This disagreement was attributed to the disturbance caused by the presence of a precursor ahead of the rim arising from surface tension gradient due to surface shrinkage and surfactant concentration (McEntee and Mysels, 1969; Mysels and Stikeleeather, 1971). It was inferred by Frankel and Mysels (Frankel and Mysels, 1969) that the slow growth-rate should be due to a large variation of the local surface tension at the film-front. Although such local fluctuation is not unusual (Moody and Attard, 2001; Wen et al., 2021), capturing these with continuum models is difficult, and the only MD study is the quasi-2D case of Kono et al. (Kono et al., 2014) who

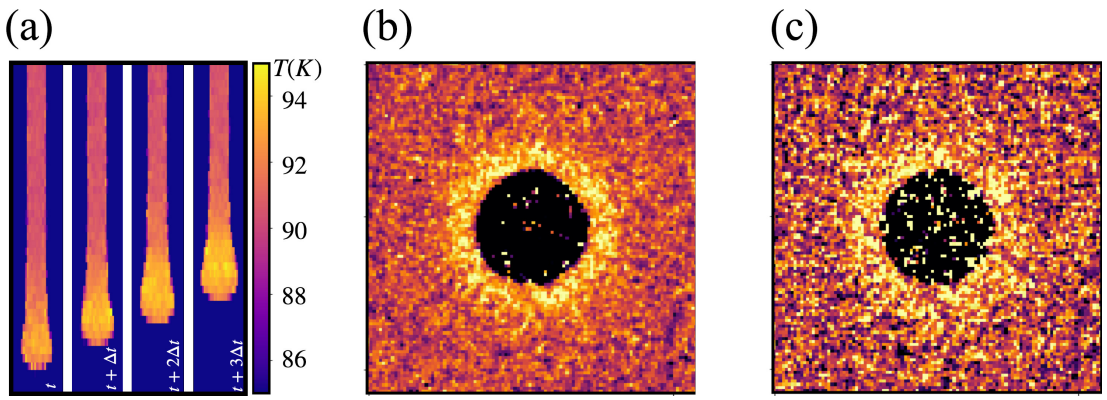


Figure 5.5: (a) Radial-averaged temperature field shows warmer rim/blob region as the film retracts. Top-down view of the film (b) averaged over the thickness, and (c) central-slice shows a region of elevated temperature surrounding the film. For each of the figures, same color-bar applies which is in the units of Kelvin.

reported considerable temperature rise ($> 5K$) in the liquid surrounding the hole for $h_0 \approx 5\,\text{nm}$.

In contrast to 2D systems, fully 3D simulations are computationally more expensive, but avoid the well-known deficiencies of 2D fluids, such as divergent transport coefficients (Irving and Kirkwood, 1950b). One expects the behavior of an interface to be dominated by the number of interacting neighboring molecules - which is much smaller in 2D. Therefore, a 2D interface would be overly susceptible to rupture (Koplik and Banavar, 1993). Even with periodic boundary conditions, the strong system-size dependency of the diffusion coefficient cannot also be ignored (Yeh and Hummer, 2004). The present study therefore minimizes these effects by simulating a fully three-dimensional (3D) system which is ≈ 8 times larger (in terms of particle number) than the 2D system of (Kono et al., 2014). A warmer region surrounding the expanding hole is observed, and the temperature increase is rather less pronounced, 2.9K vs. > 5K.

Fig. 5.5 (a) shows the radial-averaged temperature field for $h_0 \sim 14$, at four instantaneous time as the film retracts. It is observed that the temperature inside the rim is higher than the rest of the film. Similar observations are made from the thickness averaged (panel b) and the central slice (panel c) top-down view of the temperature

field. Clearly a warmer rim region surrounds the expanding hole. To quantify the temperature increase, an annular region of inner radius, r_i, and width dr (set arbitrarily to one third of σ) is drawn which surrounds the hole, and the average temperature of this circular strip is defined as $T_{\text{c.av}}$. For each instantaneous time, $T_{\text{c.av}}$ is measured for increasing r_i and plotted against the radial distance from the hole center. Fig. 5.6 (a-c) plots $T_{\text{c.av}}$ against r for three such instantaneous time. Temperature is seen to increase in the part of the film that just surrounds the hole, reaches a peak and then decreases to the film temperature. Notably, and as also observed by Kono et al. (2014), the maximum temperature does not remain constant, rather increases with time (panels a to c). Fig. 5.6 (d) plots the temporal evolution of the maximum local temperature, $T_{\text{c.av}}^{\text{max}}$. As seen from the figure and in line with Kono et al. (2014)'s observations, $T_{\text{c.av}}^{\text{max}}$ tends to convergence, although does not reach within our simulation time window. Note here, the retraction speed in the case considered for this study reaches the constant TC speed before $t/\tau_{\text{inv}} = 10$. The rise in temperature decreases for thicker films (Kono et al., 2014).

Such an increase in temperature constitutes around $5 - 7\%$ drop in γ. This is, of course, non-negligible; but is not sufficient to explain the slower retraction. Note, the local increase in temperature will slightly lower the viscosity of the liquid surrounding the hole, but should not result in a perceptible variation in Oh.

5.7 Surface Tension Modulation due to Curvature

The retraction process is mainly driven by the tangential component of the pressure tensor (Braga et al., 2018; Shi et al., 2023), while the normal component is responsible for the radial growth of the rim. From the constituent pressure components, γ can be locally calculated using the Kirkwood-Buff definition (Kirkwood and Buff, 1949) from the Hulshof integral (Hulshof, 1901) as:

$$\gamma_r = \frac{1}{2}\int_{-\infty}^{\infty} \left[P_{xx}(r,x) - P_{rr}(r,x)\right] dx \tag{5.5}$$

Here, $P_{xx}(r,x)$ is the normal pressure at location r, where x denotes the direction normal to the film surface at r; $P_{rr}(r,x)$ is the tangential pressure at r. The time-

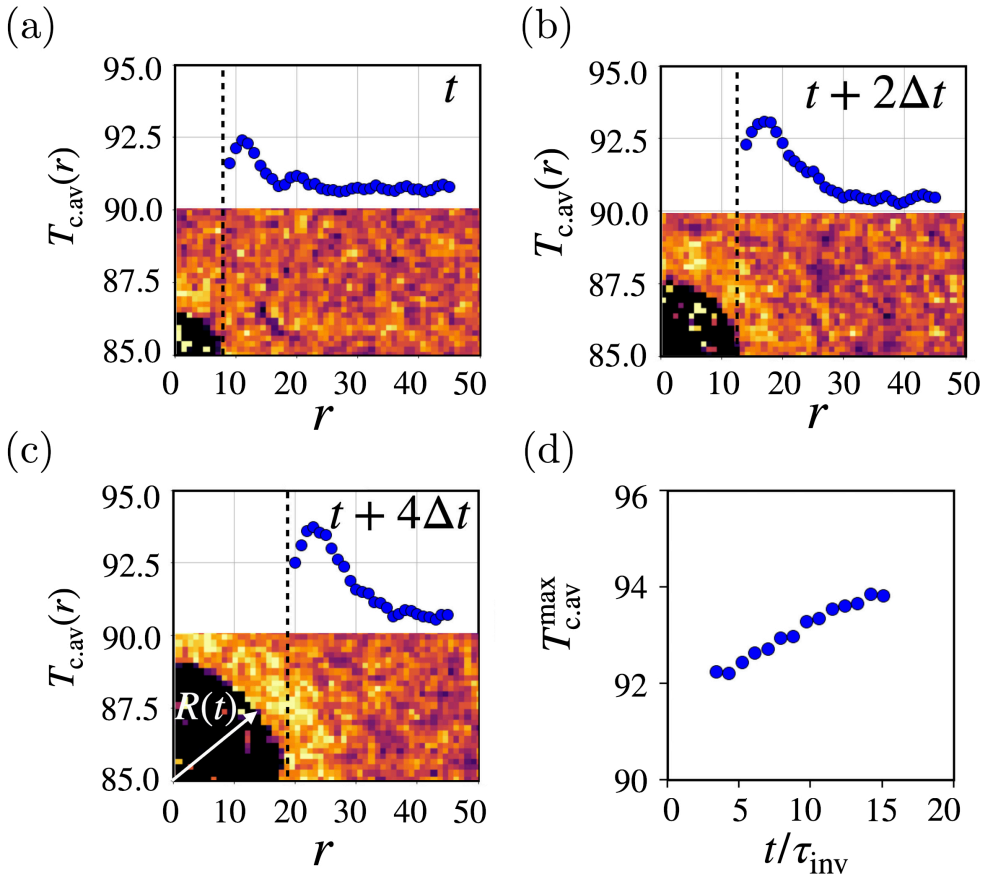


Figure 5.6: (a-c) Averaged temperature along a circular strip of width dr surrounding the hole is plotted against increasing radius. The insets show the top-right quadrant of the corresponding thickness-averaged temperature fields. (d) Maximum temperature (averaged over ± 10 time-steps) slowly approaches to convergence. For each of the figures, $Y-$axis is in the units of Kelvin.

averaged surface tension is found to be 0.51 which is in excellent agreement with the literature (Mecke et al., 1997) for similar cut-off radius. If the pressure tensor is resolved spatially along the film profile in the local tangential and normal directions, this reveals a noticeable depression of the tangential pressure. The time-averaged (local) tangential pressures obtained in this fashion are plotted in Fig. 5.7 (a) which shows the noticeable depression of the tangential pressure at the tip as compared to

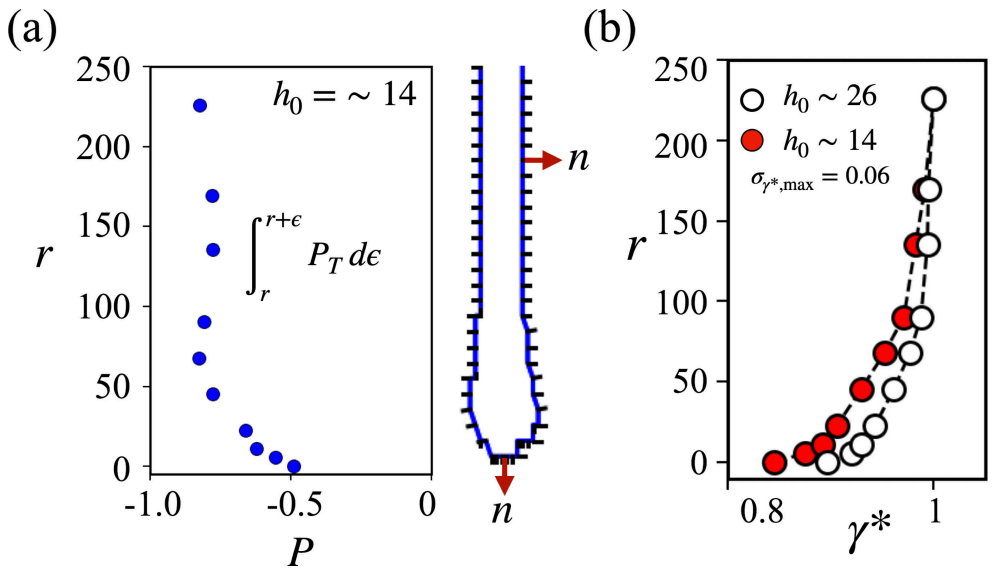


Figure 5.7: (a) Tangential component of pressure along the radial direction of a film of thickness, $h_0 \sim 14$. Schematic at the right shows local normal directions to the surface. (b) The drop in local surface tension at the film front for a relatively thicker film ($h_0 \sim 26$) is less pronounced than that of a thinner film ($h_0 \sim 14$). The maximum standard deviation of γ and γ^* in panels b and c are, respectively, 0.03 and 0.06.

the far-field[†].

The tension acts as a 'pulling force' in Taylor-Culick formulation, purely in the

[†]The Cartesian coordinate system is first transformed to radial coordinates. Later, the tangential components of the pressure tensor are transformed as:

$$\begin{aligned} P_{t1} &= P_{xx}\cos^2\theta + P_{yy}\sin^2\theta + P_{xy}\sin 2\theta \\ P_{t2} &= P_{xx}\sin^2\theta + P_{yy}\cos^2\theta - 2P_{xy}\sin\theta\cos\theta \end{aligned} \tag{5.6}$$

The normal forces acting around the rim should cancel each other. To identify any local variation, a strip of infinitesimally small width is defined over which the tangential and normal pressure are integrated.

A full rotation and mapping of the pressure tensor using a radially-varying normal vector does not give a notably different surface tension. A rotation of the pressure tensor to get true normal and tangential pressure at each point on the surface, together with an integral along the local surface normal $\mathbf{n}(r)$ at each point on the interface, would give

$$\gamma_n = \frac{1}{2}\int_{-\infty}^{\infty} [\boldsymbol{P}\cdot\mathbf{n} - \boldsymbol{P}\cdot\mathbf{t}]\cdot d\mathbf{n} \tag{5.7}$$

This surface tension, $\gamma_{rot.}$ shows broadly similar trends, see Fig. 5.7 (b). A relatively thicker film with $h_0 \approx 26$ was simulated, and a decrement in γ was observed. However, the decrease in tip surface tension, $\Delta\gamma$ for $h_0 \approx 26$ is less than that for $h_0 \approx 14$. Note, the quantities reported in Fig. 5.7 are time-averaged, and also radially averaged to obtain better statistics.

direction of retraction, seen from the Kirkwood-Buff with P_{rr} the main contribution to γ. The bottom-panel in Fig. 5.4 (c) shows the ratio of the local to global surface tension (time-averaged and radial-averaged) with increasing r. Remarkably, this gives evidence of a substantial drop in γ_r ($\approx 15\%$) at the tip of the retracting film ($r = 0$), and $\gamma_r \to \gamma$ far from the rim. While the local temperature rise explains a $\approx 5 - 7\%$ drop ($\epsilon_{\gamma,T}$) in γ, the remaining can be attributed to surface curvature and shrinkage, $\epsilon_{\gamma,\kappa}$, so $\epsilon_\gamma = \epsilon_{\gamma,T} + \epsilon_{\gamma,\kappa}$. This is plausible that the latter reduction is linked to the Tolman length effect. However, given the complexity and ambiguity in quantifying the Tolman length (Lei et al., 2005; van Giessen and Blokhuis, 2009), this is not pursued in the present work. Interested readers are referred to Wen et al. (2021) on the curvature dependence of surface tension for simpler systems. Accounting for the local variation in surface tension, an improvement $\epsilon_\gamma = 1 - \sqrt{\gamma_{r=0}/\gamma}$ is obtained; and for the present case, using the surface tension averaged over the film front in Eq. (2.7) results in agreement with the measured speed within only a $\approx 8\%$ deviation, shown by the dashed line denoted by U^*_γ in Fig. 5.4 (b). These corrections, however, will diminish for thicker films as the variations of temperature (Kono et al., 2014) and curvature become less pronounced.

5.8 Transition Regime

The classical formulation discounts any possibility of a transition regime between the rim and the undisturbed film. Our results confirm, for molecularly thin films, the existence of an intermediate (or transition) bridge between the rim and the undisturbed film (Fig 4.1 b). The top panel in Fig. 5.4 (c) shows an idealized picture of film retraction upon which the TC formalism is based on. This simplified description requires the liquid from the hole to be collected in a spherical rim bordering on the unperturbed film. Contrasting Taylor's assumption of a sudden transformation, the present study rather agrees with the experimentally (Lhuissier and Villermaux, 2009b; Petit et al., 2015) and numerically (Gordillo et al., 2011; Koplik and Banavar, 2000) observed transition, shown in the mid-panel of Fig. 5.4 (c). Previous studies reported an 'aureole-shaped' regime for films of liquid with surfactants, and attributed this to surface tension gradient, and surface elasticity (De Corato et al., 2022; Lhuissier and

Villermaux, 2009a; Petit et al., 2015). Existence of a similar 'extended rim' in the present study - where the film is made of pure liquid - indicates a local variation of the surface force, but caused by curvature effects (geometry).

The transition[‡] can be explored through a mass balance argument by assuming an elliptic blob, of aspect ratio $\alpha = b/a$, connected by a smooth transition region, of length L, to the neck of width h_0. The length, L is given by,

$$L = \pi h_0(\beta^2 - 1)/2\alpha \tag{5.8}$$

where, $\beta = 2b/h_0$. Transition must take place over the finite length, L (Frankel and Mysels, 1969), rather than the assumption of an unperturbed film bordering on the rim. As Eq. (5.8) suggests, the transition length becomes more prominent with thinner films, and disappears when $b \approx h_0/2$ corresponding to viscous film retraction (Brenner and Gueyffier, 1999; Savva and Bush, 2009). The MD data indicates that the normal pressure difference of the surface is minimal at the point where the rim meets the transition region. In order to satisfy the Young-Laplace equation, it follows that the absolute value of the curvature must also be minimized. Under these assumptions, the atomistic form of Eq. (2.7) can be expressed as

$$U = \left(1 + \alpha^2\right)^{-1/4} U_{\mathrm{TC}}. \tag{5.9}$$

For simplicity, assuming a spherical rim, i.e., $\alpha = 1$ yields a surface-shape correction factor, $\epsilon_\alpha = 2^{-1/4} \approx 0.84$. When ϵ_α is accounted for, in addition to ϵ_γ, the corrected TC model ($U^*_{\gamma,\alpha}$) shows close agreement with the MD results. This is shown by the solid symbols in Fig. 5.4 (b), and as evidenced by the figure, $U^*_{\gamma,\alpha} \approx 1$.

There remain a few other aspects which plausibly affect the dynamics of film retraction. Any mutual dependency of the two correction factors developed in this study cannot be ruled out. The growth of the blob is non-negligible as compared to $\dot{R}$. In situations like this, it has been argued (De Corato et al., 2022; Pierson et al., 2020; Savva and Bush, 2009) that the velocity within the blob is non-uniform; the velocity vectors overlaid on the temperature field in Fig. 5.4 (c) confirm this hypothesis. The

[‡]This theoretical exercise is carried out by Li Shen and Ben Collard, co-authors of Rahman et. al., J. Chem. Phys. (2023) which is based on this chapter.

effect of this velocity would contribute to the departure of the blob shape from being circular and therefore, is assumed to be included in the surface shape correction, ϵ_α. The effect of evaporation, however, in agreement with previous study (Kono et al., 2014), was found to be negligible.

5.9 Summary

To summarize, this study examines the Taylor-Culick theory for film retraction at atomic scale using large-scale MD simulations. Similar growth rate of holes made by two separate methods, either poking or cutting, confirms that the dynamics is independent of hole creation mechanism. This then allows a systematic study, where this chapter repeatably shows a short term exponential growth period followed by a constant velocity regime over an ensemble of cases - both behaviours observed in the experimental literature. A Lennard-Jones model is used to remove viscoelastic effects so the various driving contributions to the growth dynamics can be exposed. The theoretical conjecture of a constant terminal retraction rate is accurate at this scale, however, this study shows that estimating the 'true' retraction speed requires corrections for (i) the local variation of surface tension arising from surface curvature and temperature rise, and, (ii) the existence of a transition regime between the rim and the unperturbed film - both of these factors were ignored in the classical formulation. Surface tension, and interface shapes are outputs of MD simulations, and this chapter shows how they contribute to the dynamics, and quantifies their impact. While these contributions are marginal for macroscopic films, these are the key reasons for the failure of the classical theory as film thickness is reduced to nano-scale. This work provides compelling evidence that the pioneering theory of Taylor and Culick, which in its original form fails at the atomic scale, can be corrected to accurately predict the film retraction speed.

This page intentionally left blank.

Have fun on sea and land
Unhappy it is to become famous
Riches, honors, false glitters of this world
All is but soap bubbles. (Boudin)

Pierre-Gilles de Gennes (Nobel lecture)

6

Transport on the Surface

Surfactant dynamics at the liquid-vapor interface is central to a broad spectrum of applications, spanning from engineering to natural phenomena. The well-documented role of surfactants in modulating surface tension and facilitating complex fluid behavior contrasts sharply with the absence of detailed understanding of their transport mechanisms at the nanoscale - an area where traditional continuum models often fall short. This study employs non-equilibrium molecular dynamics simulations to obtain molecular-level insights, which are subsequently incorporated into the continuum transport equation to improve its resolution. This leads to a notable alignment between the two models in depicting the transport of surfactant molecules along the interface of a deforming thin liquid film. The enhancement of the continuum model's fidelity at the nanoscale, by coupling with the molecular scale details, signals a leap forward in the understanding of the interfacial dynamics*.

*A version of this chapter is in preparation for submission as Rahman, M.R. et al., Nanoscale Surfactant Transport: Bridging Molecular and Continuum Models (under review).

6.1 Introduction

† The continuum framework, with its reliance on long wave approximations, often falls short in addressing the subtleties at the nanoscale − a domain uniquely suited to the strengths of molecular dynamics analysis. Specially, the non-equilibrium nature of the transport process makes molecular dynamics more appropriate to tackle these questions. Regardless, the nano-scale mechanisms underlying surfactant transport along the interface have remained relatively under explored (Maldarelli et al., 2022). The MD community focused largely on the understanding of the structural and thermodynamic properties of surfactants (Bui et al., 2021; Chanda and Bandyopadhyay, 2005; Rideg et al., 2012; Shi et al., 2019), micelles formation, their adsorption kinetics and self assembly (Kanduc et al., 2024; Marrink et al., 2000; Sangwai and Sureshkumar, 2011; Shinoda et al., 2008; Wang and Larson, 2015; Weiand et al., 2023), transport of nanoparticles across surfactant monolayer (Xu et al., 2017), or the spreading mechanism of surfactant laden droplets on solid substrates (Kim et al., 2006; Theodorakis et al., 2019). Of the very few studies that looked at the dynamical behavior of surfactant at the interface, Johansson et al. (2022) studied a system of two immiscible Lennard-Jones fluids with surfactants at the interface. Their study highlighted the importance of local surfactant concentration and interfacial viscosity in accurately modeling the nanoscopic flows. The study described in this Chapter, models the transport of surfactants (*sds*) on the liquid-vapor surface of a thin water film by employing non-equilibrium molecular dynamics simulations (NEMD). The primary motivation stems from the question of whether the continuum model is sufficient to describe transport processes at the microscopic scale. To address this, present study carefully deconstructs the components of the transport equation to a molecular resolution, incorporating their local variations, and compares these findings against empirical data derived from present molecular simulations.

†The MD and FD algorithms have been developed by MRR, whereas, a molecular version of the transport equation has been derived by Edward R. Smith. This molecular transport equation is briefly discussed in Appendix B, and described in full length in Rahman et al., Nanoscale Surfactant Transport: Bridging Molecular and Continuum Models (under review).

6.2 Problem Description

A thin water film of length, $2L = 100\,\text{nm}$, width, $w = 20\,\text{nm}$, and thickness $h = 10\,\text{nm}$ is considered. A monolayer of sodium dodecyl sulfate (SDS) − a soluble surfactant − is placed at the central area of both the top and bottom surfaces of the film, without perturbing the film, see Fig. 6.1 (a), which spans an area of $20 \times 20\,\text{nm}^2$. The presence of surfactant results in a reduced surface tension at the central region as compared to the surfactant free regions. Consequently, a surface pressure develops, i.e., $\Pi = \gamma_0 - \gamma_m$; where, γ_0 is the surface tension at the leading edge of the surfactant monolayer, or of the pure supporting liquid, and γ_m is the surface tension of water within the adsorbed monolayer (Myers et al., 1999). This so called surface pressure initiates fluid flow which then leads to the transport of the surfactant in a complex and coupled way. Another set of simulations are carried out considering similar situations, with the exception that the horizontal film below the surfactant monolayer is replaced with a droplet (as in panel b in Fig.6.1).

6.3 Molecular Description of the System

A coarse-grained modeling approach is employed to simulate the behavior of water and sodium dodecyl sulfate (SDS) molecules. The MARTINI polarizable water model (Yesylevskyy et al., 2010) is used here, which considers both the Lennard-Jones interactions with surrounding particles, and Coulombic interactions. the SDS molecule is described by a five-bead coarse-grained model (Anogiannakis et al., 2019; Weiand et al., 2023). This includes three apolar C_1 beads, each representing a chain of four methylene groups, a negatively charged Q_a bead for the hydrophilic sulfate headgroup, and a Q_d bead to represent the sodium cation. The film (or, the droplet) and the surfactant monolayers on both the surfaces are separately energy minimized, thermostated (at 300 K) with the Nosé-Hoover thermostat (Hoover, 1985; Nosé, 1984), and sufficiently pre-equilibrated (for 5 ns). The initial configurations were separately equilibrated (Fig. 6.2 panels a−c) in the NVT (canonical) ensemble to stabilize the system to a target temperature of 300 K. The equilibration of the two species was carried out separately to restrict any surfactant transport before the system is stabilized,

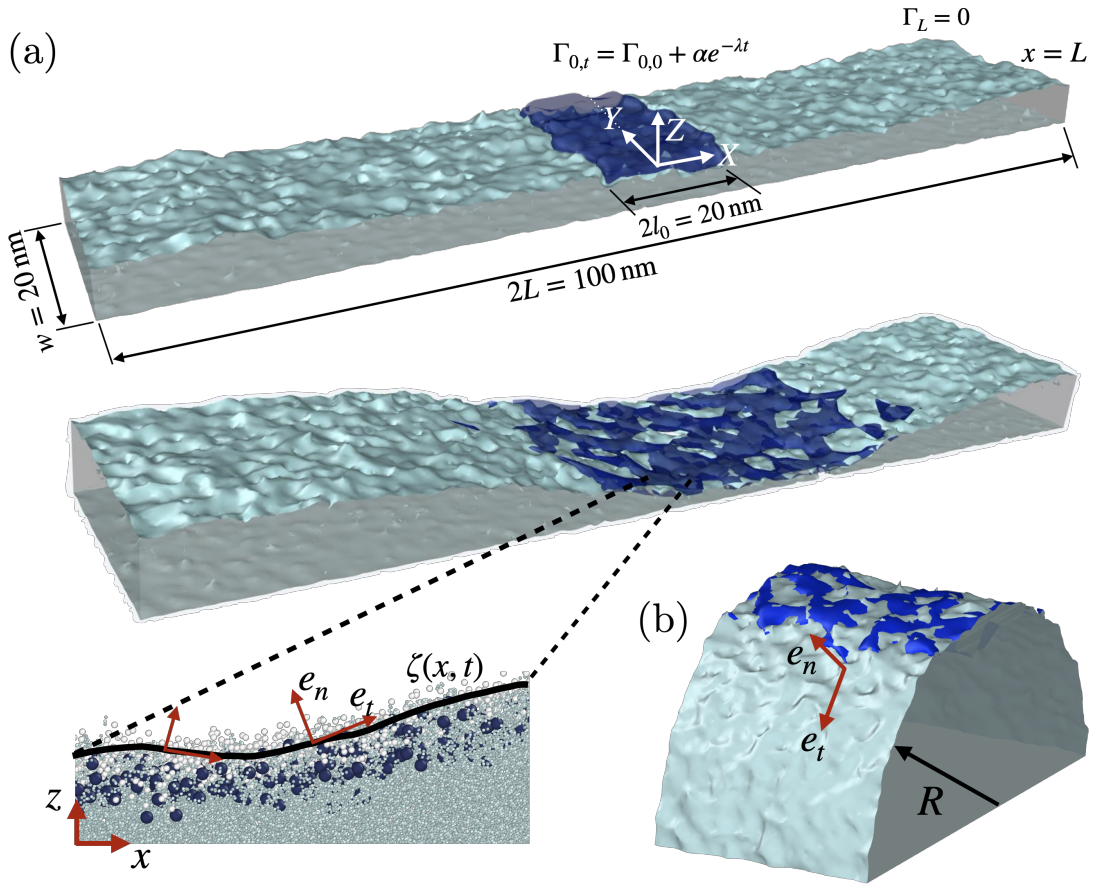


Figure 6.1: (a) A monolayer of sodium dodecyl sulfate deposited on the central area of a thin water film of dimensions 100nm × 20nm × 10nm, where the third dimension denotes film thickness, h_0. Top-panel: surfactant initially concentrated over an area of 20nm × 20nm. Bottom panel illustrates the spreading of the monolayer across the surface, and subsequent deformation of the film. The local curvature of the surfactant-water-air interface is shown in the zoomed inset, the surface element $d\mathbf{s}$ is resolved into normal, $\mathbf{e_n}$ and tangential, $\mathbf{e_t}$ components. Solid line shows spline fitting, $\zeta(x,t)$ to the surface. (b) Surfactant transport along the surface of a (cylindrical) droplet of radius, $R = 15$nm.

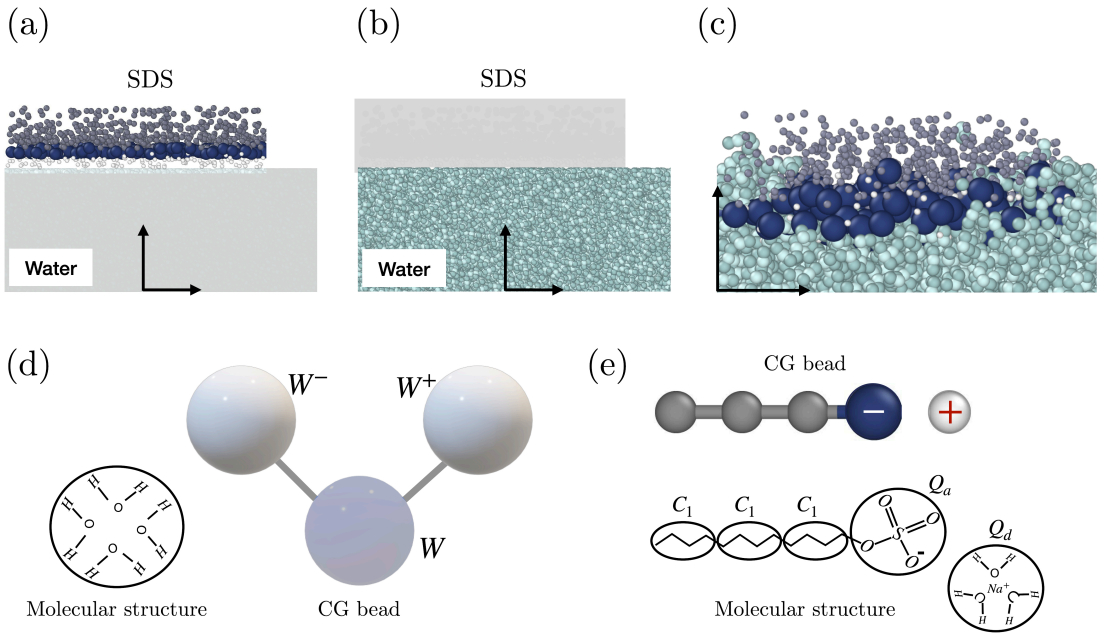


Figure 6.2: (a,b) Initial configuration of SDS layer and water film, with Hydrophilic head group of SDS close to the water surface, and hydrophilic tail group away from the surface. These were separately equilibrated: equilibration of (a) SDS, (b) water. (c) Zoomed view of a portion of the surfactant-water interface after equilibration. Schematic of the coarse grain description of (d) MARTINI polarizable water model consisting of three CG beads, where 4 water molecules are mapped into one bead, and (e) SDS CG bead. Molecular structures of water and SDS are also shown, respectively, in panels d and e.

and before the production phase starts. Following this, the system underwent a NVT production phase when data were collected for analysis (although the micro-canonical ensemble would have been a more natural choice, production phase was carried out in the canonical ensemble for the sake of consistency with the available literature concerning MD of surfactant transport). Panels (d−e) show, respectively, the coarse grain descriptions of water, and SDS. This approach leads to a well equilibrated initial state before commencing the production phase within the canonical (NVT) ensemble. Simulations are carried out using the open source Large-scale Atomic/Molecular Massively Parallel Simulator, LAMMPS. Velocity-Verlet integrator is used with a timestep of 5 fs. All properties from the MD simulations are averaged over the width

of the film (y-axis) for improved statistics.

6.3.1 MARTINI WATER MODEL

The MARTINI water model is composed of three particles: a charge-neutral central particle (w), accompanied by positively (wp) and negatively charged (wm) particles. The central particle, w engages in Lennard-Jones interactions with surrounding particles, whereas wp and wm interact via Coulombic forces, with no interaction occurring within the same water bead. The mass of each coarse-grained bead is set at 72 amu, reflecting the aggregate mass of four actual water molecules, as in Fig. 6.2.

The initial configurations were prepared using the open source codes Packmol (Martínez et al., 2009) and Moltemplate (Jewett et al., 2021). All simulations for this study were carried out in the Large-scale Atomic/Molecular Massively Parallel Simulator, LAMMPS (Thompson et al., 2022). The molecular model incorporated detailed representations for both bonded and non-bonded interactions. Bonded interactions were described using harmonic potentials for bonds, i.e.,

$$V_b(r_{ij}) = \frac{1}{2}k^b_{ij}(r_{ij} - b_{ij})^2$$

were, $V_b(r_{ij})$ is the potential energy associated with the bond between atoms i and j at distance r_{ij}. b_{ij} is the equilibrium bond length between atoms i and j, i.e., the natural length of the bond at which the potential energy is minimized, and k_{ij} is the force constant that determines the stiffness of the bond. To model the energy associated with the bending of angles between three consecutive bonded atoms, the cosine-squared potential was used. This is generally expressed as:

$$V_a(\theta) = \frac{1}{2}k^\theta \left(\cos\theta - \cos\theta_0\right)^2$$

here, V_a is the potential energy as a function of angle θ formed by three bonded atoms i, j and k; θ_0 is the equilibrium angle, and k^θ is the force constant for angle. Non-bonded interactions were accounted for through a combination of Lennard-Jones and Coulombic potentials, employing a hybrid overlay approach to capture the nuanced

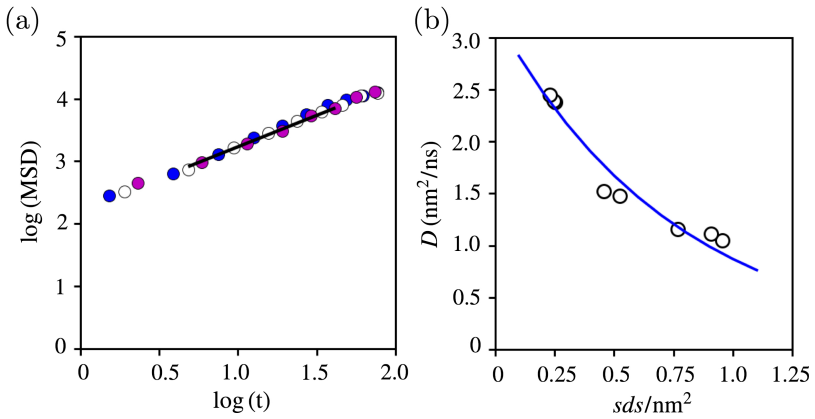


Figure 6.3: Estimating diffusion coefficient. (a) Mean square displacements of surfactant molecules homogeneously spread over the surface of a film. (b) Diffusion coefficient as a function of surfactant concentration. Blue line denote fitting to the data of the form: $D = \alpha\, e^{-\beta\rho}$.

interplay of forces at different scales. Generally expresses as:

$$V_{\text{non-bonded}}(r) = V_{\text{LJ}}(r) + V_{\text{Coul.}}(r)$$

where $V_{\text{LJ}}(r)$ is the Lennard-Jones potential, i.e.,

$$V_{\text{LJ}}(r) = 4\varepsilon \left[\left(\frac{\sigma}{r}\right)^{12} - \left(\frac{\sigma}{r}\right)^{6} \right]$$

and the Coulombic interactions are given by,

$$V_{\text{Coul.}}(r) = (q_i q_j / 4\pi\varepsilon_0\varepsilon_r)\frac{1}{r}$$

where, symbols carry their usual meanings. The long-range electrostatic forces were calculated by the *Particle-Particle Particle-Mesh* (PPPM) algorithm. This method allowed to accurately account for the electrostatic component of our system at reasonable computational cost. The *SHAKE* algorithm was used to maintain rigid $O-H$ bonds within water molecules.

6.3.2 Diffusion Coefficient

In a dedicated series of simulations focusing on uniformly distributed surfactants on a water film, the surface diffusion of SDS molecules was estimated. To distinguish surface diffusion from bulk diffusion, only the surfactant molecules that remained on the film's surface were tracked. As discussed earlier, the trajectories of these molecules were analyzed to calculate the mean squared displacement (MSD) over the simulation period, i.e., MSD $= \langle |s(t_0 - t) - s(t_0)|^2 \rangle$, where $s(t)$ is the position of a molecule at time t and $s(t_0)$ is its initial position. Subsequently, Einstein's equation for surface diffusion, $D_s = \text{MSD}/t$ (Rideg et al., 2012) is employed. Fig. 6.3 (a) shows MSD of the surfactant molecules from three independent simulations, but for same concentration. The average slope gives the diffusion coefficient, D. The diffusion coefficient obtained shows a concentration dependence, i.e., $D_s = 3.22\text{e}^{-\beta\rho}$, where ρ is the number of SDS molecules per unit area, $\beta = 4/3$. For dimensional consistency, β should have the units of ρ^{-1}. This functional relation employed in solving (6.1), accounts for variations in local diffusivity caused by the variable local surfactant concentration, instead of a constant diffusion coefficient. Fig. 6.3 (b) shows this variation of D over a range of concentrations. This is consistent with scenarios where intermolecular interactions become significant at higher concentrations, leading to a reduced mobility of the molecules.

6.4 Continuum Description of Surfactant Transport

The spreading of the surfactant layer across the liquid-air interface, results in a locally dilute surfactant-water layer that extends over a larger surface area. This dynamic behavior of the surfactant monolayer is described by the advection-diffusion equation (Gaver and Grotberg, 1990; Stone, 1990), a continuum model that elegantly captures the underlying physical mechanisms of the transport phenomena on the surface:

$$\frac{\partial \Gamma}{\partial t} + \underbrace{\nabla_s \cdot (\Gamma \mathbf{u_s})}_{\text{advection}} + \underbrace{\Gamma(\nabla_s \cdot \mathbf{e_n})(\mathbf{u} \cdot \mathbf{e_n})}_{\text{geometric effect}} = \underbrace{D_s \nabla_s^2 \Gamma}_{\text{diffusion}} + \underbrace{j_n}_{\text{source term}} \tag{6.1}$$

Here, Γ denotes the local surfactant concentration, $\mathbf{u_s}$ represents the velocity vector along the surface, $\mathbf{e_n}$ is the unit normal vector to the surface and $\nabla_s = (\mathbf{I} - \mathbf{e_n}\mathbf{e_n})$ is the surface gradient operator. D_s characterizes the surfactant diffusion rate across the interface. The second and third terms in equation (6.1) describe surfactant advection along the surface, the fourth term, $D_s\nabla_s^2\Gamma$, elucidates the diffusive transport of surfactants, and j_n models the adsorption or desorption of surfactants, acting as a source or sink in the system. While, j_n is pivotal in understanding the mechanisms through which surfactants are introduced to or eliminated from the interface, influencing the overall dynamics of surfactant transport, this term is avoided by carefully selecting the surface concentrations, Γ_0 to obtain $j_n \to 0$, cases where surfactants were absorbed into the bulk and formed micelles, were discarded. Collectively, the above elements of the transport equation provide a comprehensive understanding of surfactant spreading dynamics, shedding light on the intricate interplay between diffusion, advection, and surface processes that dictate the behavior of surfactants at the interface.

6.4.1 Numerical Scheme

A finite difference scheme for the numerical resolution of the transport equation, (6.1), employs both spatial and temporal discretizations to capture the dynamics of surfactant transport due to advection, diffusion, and surface curvature effects. A simple backwards Euler is used to discretise the evolution of Γ in time,

$$\frac{\partial \Gamma}{\partial t} \approx \frac{\Gamma_i^n - \Gamma_i^{n-1}}{\Delta t} \tag{6.2}$$

where superscripts denote the time steps and subscripts the spatial. The advection terms is one dimensional in s, hence, $\nabla_s \cdot (\Gamma \mathbf{u_s}) = \partial \Gamma u/\partial s$ with the subscript in u_s dropped for notational simplicity,

$$\frac{\partial \Gamma u}{\partial s} = u\frac{\partial \Gamma}{\partial s} + \Gamma\frac{\partial u}{\partial s} \approx u_i\frac{\Gamma_{i+1} - \Gamma_i}{\Delta s} + \Gamma_i\frac{u_{i+1} - u_i}{\Delta s}$$

Here forward difference has been used to include upwinding (Hirsch, 2007) as $u > 0$ with surfactant moving from left to right and $\Gamma \geq 0$. The distance along the interface is worked out from $(\Delta s)^2 = (\Delta x)^2 + (\Delta z)^2$. For the diffusion term, a second order

discretisation is applied,

$$D_s \frac{\partial^2 \Gamma}{\partial s^2} \approx D_s \frac{\Gamma_{i+1} - 2\Gamma_i + \Gamma_{i-1}}{(\Delta s)^2} \tag{6.3}$$

Together, the discretized form of the transport equation is:

$$\frac{\Gamma_i^n - \Gamma_i^{n-1}}{\Delta t} + u_i^n \frac{\Gamma_{i+1}^n - \Gamma_i^n}{\Delta s} + \Gamma_i^n \frac{u_{i+1}^n - u_i^n}{\Delta s} + \Gamma_i^n \kappa_i^n v_i^n = D_s \frac{\Gamma_{i+1}^n - 2\Gamma_i^n + \Gamma_{i-1}^n}{(\Delta s)^2} \tag{6.4}$$

Assuming a zero source term (i.e., $j_n = 0$), the discretized form of the transport equation, with like terms grouped together in the form of a matrix $a\Gamma = b$, is given by

$$\Gamma_{i+1}^n \overbrace{\left[\frac{\Delta t u_i^n}{\Delta S} - \frac{D\Delta t}{(\Delta S)^2}\right]}^{a_{i+1}^n} + \Gamma_i \overbrace{\left[1 + \Delta t \left(\frac{u_{i+1}^n - 2u_i^n}{\Delta s} + \kappa_i^n v_i^n + \frac{2D}{(\Delta s)^2}\right)\right]}^{a_i^n} + \Gamma_{i-1}^n \overbrace{\left[-\frac{D\Delta t}{(\Delta S)^2}\right]}^{a_{i-1}} = \Gamma_i^{n-1} \tag{6.5}$$

here, i and n denotes, respectively, spatial and temporal discretization.

In solving the transport model, the domain assumes symmetry about $x = 0$, and hence is discretized from $x = 0$ to $x = l$ along the positive x-axis. Note, the continuum equation is solved in s coordinates following the surface; x and s are equivalent, only difference arises in quantifying the length traveled by the molecules, i.e., $\Delta s \neq \Delta x$. As such, the distance along the surface is worked out from $(\Delta s)^2 = (\Delta x)^2 + (\Delta z)^2$. The following set of initial and boundary conditions and the surface fit provides a

closed-set of equations to solve the transport model:

$$\Gamma(s, t = 0) = \Gamma_{MD}(s, t = 0) \tag{6.6}$$

$$\Gamma(s = 0, t) = \alpha e^{-\lambda t} + \alpha_0 \tag{6.7}$$

$$\Gamma(s = l, t) = 0 \tag{6.8}$$

$$\boldsymbol{e_n}(s, t) = -\frac{\nabla_s \zeta(s, t)}{||\nabla_s \zeta(s, t)||} \tag{6.9}$$

$$u_s(s, t) = \frac{1}{\Gamma} \Sigma_{i=1}^{N} m_i s_i \vartheta_i \tag{6.10}$$

$$D_s = D_0 \mathrm{e}^{-\beta \rho} \tag{6.11}$$

The initial concentration field is set to the MD data at $t = 0$ (6.6), the left boundary condition (6.7) is modeled based on a fit to the data from MD at $s = 0$. As surfactant molecules do not reach the right end of the film during the simulation time, zero concentration is assumed at the far right (6.8). A careful tracking of the spatially and temporarily evolving surface to get the local properties is necessary to attain an accurate molecular description of the transport process. The system of equations is solved using the inbuilt linear algebra solver in Numpy (v.1.26.0). The accuracy of the implicit numerical scheme has been confirmed by testing against the analytical solutions of pure convection and pure diffusion.

The accuracy of the implicit numerical scheme has been confirmed by testing against the analytical solutions of pure convection and pure diffusion. In solving the surfactant transport, the domain assumes symmetry about $x = 0$, and hence is discretized from $x = 0$ to $x = l$ along the positive x-axis. The initial concentration field was set to the MD data at $t = t_0$, i.e., $\Gamma_{0,FD} = \Gamma_{0,MD}$. The left boundary condition was modeled as $\Gamma(x = 0, t) = \alpha e^{-\lambda t} + \alpha_0$ based on a fit to the MD data. At the far right, $\Gamma(x = l, t) = 0$ as surfactant molecules do not reach the right end of the film during the simulation time.

The local diffusion coefficient $D(s, t) = 3.2\, e^{-4N/3}$ for finite N was obtained by measuring the diffusion coefficient as a function of surfactant (number) concentration (see section 6.3.2). The effective diffusion coefficient, which dynamically updates

based on the local concentration, reflects non-linear interactions and is crucial for accurately modeling transport in systems with variable properties. Note, the diffusion coefficients obtained in our simulations are larger than the experimentally measured bulk diffusion of SDS in aqueous solutions (Ribeiro et al., 2003) by a factor of 2 to 3. This can be attributed to the speed up process of the kinetics in coarse grain models which contributes to the over-estimation of diffusion (Schmitt et al., 2023; Vögele et al., 2015). In Martini models, the best estimated kinetic speed up factor is approximately 4, however, the polarized water model is reported to show a ~ 2.5 times speed up (Marrink and Tieleman, 2013). However, the present study does not aim to predict these values, rather the focus is to capture the overall transport mechanism. To overcome any potential mass imbalance arising from numerical diffusion or discretization errors, a conservation correction mechanism is integrated to ensure that the total quantity of the transported scalar is preserved throughout the simulation, i.e., $\int_0^l \Gamma ds = \text{Constant}$.

The numerical resolution of the velocity field along the local tangential direction of a curved surface was a crucial aspect of the modeling process. This involved computing the scalar component of the velocity that is tangential to the topology of the surface at any given point. This has been done by resolving the local velocity into the normal and tangential components relative to the surface.

6.4.2 Reconciliation of MD with Continuum Framework

Experimental quantification of the physical mechanisms associated with surfactant transport is extremely challenging, if not impossible. This difficulty arises primarily from the interwoven physics of the process, which complicates the isolation and measurement of individual mechanisms. There are other issues − such as the molecular lengthscale of the associated processes. Any attempt to trace the surfactant particles inevitably alters their intrinsic properties, thereby affecting the system's dynamics (Manikantan and Squires, 2020). Conversely, the molecular system under investigation here affords direct access to individual molecules and their instantaneous properties, providing an ideal platform to verify the efficacy of (6.1) in describing the transport phenomena.

The second and third term of (6.1) captures the effects of surface compression and expansion due to the non-uniformity of convective flows, and curvature. These terms together account for the redistribution of surfactants driven by surface dynamics, including the Marangoni effect, which propels surfactant motion due to gradients in surface tension. The subscript 's' signifies that the quantities should be considered along the tangential direction to the surface. Specially, the third term − which is a product of local curvature, ($\kappa = \nabla_s \cdot \mathbf{e_n}$) and the surface normal velocity, ($v = \mathbf{u} \cdot \mathbf{e_n}$) − highlights the geometric effect of the locally deforming interface on the transport process. In quantifying these contributions in the transport of the surfactants, the SDS molecules at the liquid-vapor interface were tracked over time.

A careful tracking of the spatially and temporarily evolving surface to obtain the local properties is necessary for attaining an accurate molecular description of the transport process. First, a functional form of the surface, $\zeta(x,t)$ is obtained by fitting a spline to the liquid-vapor interface. Then the curvature at each point on the surface is obtained using the derivatives, i.e., $\kappa(x) = \zeta''/[1+\zeta'^2]^{3/2}$, where ζ' and ζ'' represent the first and second derivatives of the spline fit, respectively. Notably, any derivatives concerning molecular resolution are noisy, hence the Savitzky-Golay filter was used which smooths the data without significantly distorting the signal's higher moments. These calculations enables finding the spatio-temporal surface vectors, i.e., $\mathbf{e_t}$ and $\mathbf{e_n}$, which are instrumental in resolving the velocities of surfactant molecules along and normal to the interface.

Surfactant particles on a curved surface may occupy a larger area compared to a flat surface, potentially slowing down the evolution of the concentration gradient. Additionally, the paths available for diffusion are geometrically constrained by curvature, leading to anisotropic diffusion (Ramírez-Garza et al., 2021; Shu and Gong, 2001). The surface Laplacian ∇_s^2, or the Laplace-Beltrami operator, extends the concept of Laplacian to curved geometries, thus incorporating the effect of curvature on the scalar field $\Gamma(t)$.

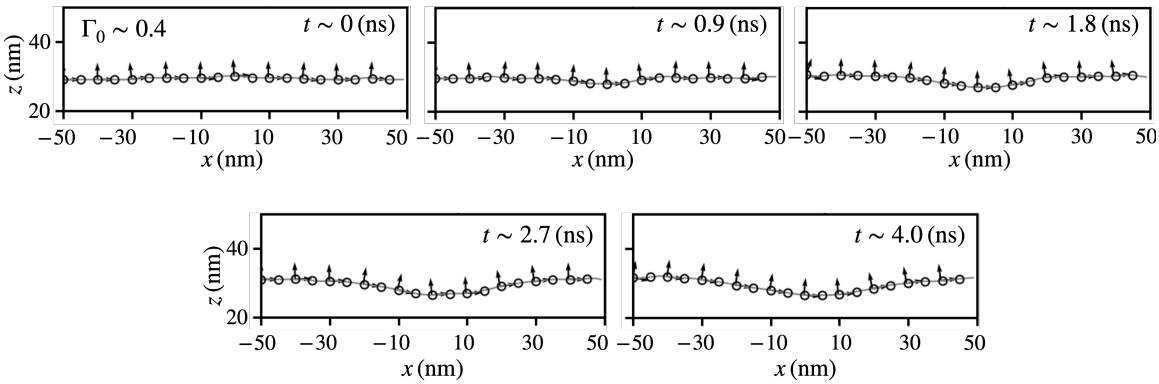


Figure 6.4: Evolution of the surface of a film with a monolayer of initial concentration, $\Gamma_0 \sim 0.4$, placed at the central area ($x = -10$ to 10) of the surface. Symbols denote surface position from MD data, while faint gray lines denote fitting to the data. Arrows show local directions normal and tangential to the surface.

6.5 Surfactant Transport

Figure 6.4 shows the time evolution of surface deformation in a thin liquid film induced by the lateral migration of surfactant molecules. The top surface of the water layer was fitted to a cubic spline which ensures ensures continuity up to the second derivatives. At the initial stage ($t \approx 0$ ns), the surface presents a near-uniform profile. As the surfactant molecules spread across the surface, they locally decrease the surface tension in the central region, giving rise to Marangoni flow. This dynamics result in the advective transport of water molecules away from the central zone. Consequently, as in Fig. 6.4, a notable reduction in film thickness at the central zone becomes evident with simultaneous increase at the edges of the film. Arrows denote local surface normal, and tangent to the surface. Surfactant velocities were resolved along these directions for the numerical solution of the transport equation.

Figure 6.5 examines the time-evolution of the local surfactant concentration, Γ (normalized by the initial concentration at $x = 0$, i.e., Γ_0) at different time instances. This considers a case where 0.35 ng of surfactant molecules is deposited on a planar film. Finite difference solution of (6.1) is depicted by the solid line, whereas, symbols denote data from MD. The close agreement affirms the validity of the continuum

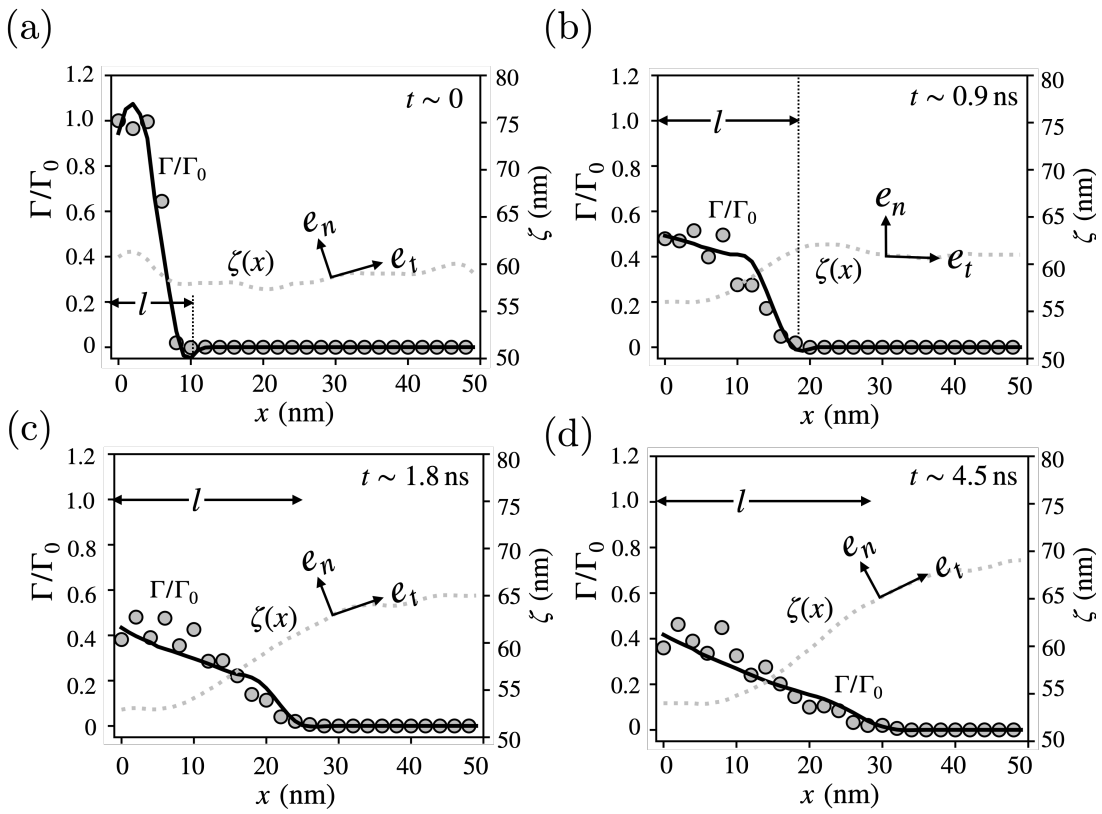


Figure 6.5: Spatio-temporal variation of surfactant concentration (normalized by initial concentration, Γ_0) along the film's length over time, i.e., at (a) $t \sim 0.75$ ns, (b) $t \sim 1.5$ ns, (c) $t \sim 3.75$ ns, and (d) $t \sim 4.5$ ns. $x = 0$ denotes the center of the film. Solid line represents surfactant evolution captured by the continuum transport equation (6.1), while symbols denote data from molecular simulations. The dotted line corresponds to spline fitting to the evolving surface. The arrows show the local tangential (e_t) and normal (e_n) surface vectors (not to scale).

model in capturing the nanoscale transport mechanism. The dotted line represent the spline fit, ζ to the instantaneous liquid-vapor surface. The agreement between the molecular dynamics simulations, and the transport equation is further evidenced from Fig. 6.6 which shows the time evolution of normalized surfactant concentration along the surface of the film for varied amount of deposited surfactant.

It is observed that simulations with denser monolayer, align more closely with the

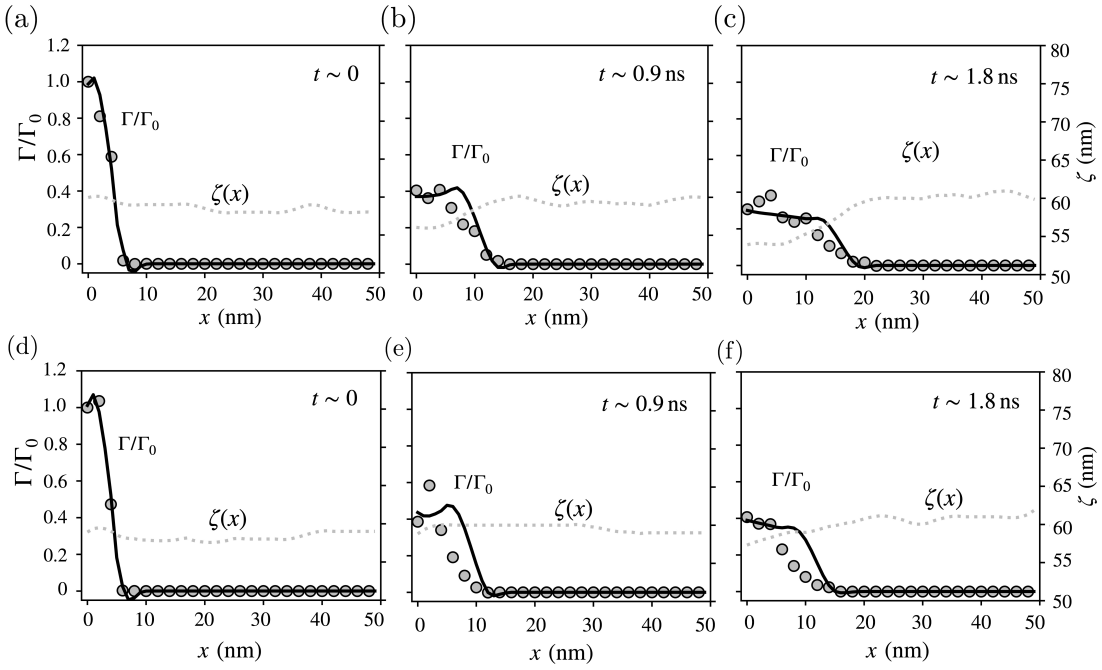


Figure 6.6: Spatio-temporal variation of surfactant concentration (normalized by initial concentration, the amount of deposited surfactant is ~ 0.75 ng for panels a-c, and $\sim$ 0.2 ng for panels d-f) along the film's surface. Solid lines denote numerical solution of the transport equation, symbols represent MD data, and the dotted lines denote fitting to the surface.

numerical solution of the transport equation. The reasons for this are not obvious but could be due in part to uncertainties associated with estimating the diffusion coefficient in these surfactant-deficient systems. Also local concentration fluctuations are likely for less denser monolayers, which would not be captured by the mean-field continuum model.

In addition to the spreading of surfactant across a planar film, the analysis has been extended to a globally curved geometry, i.e., a droplet of radius ~ 15 nm, as in Fig. 6.1 (b). Although a droplet has a higher global curvature than the planar films, Fig. 6.7 shows that the transport mechanism remains largely unaffected. The upper two panels of Fig. 6.7 depict the temporal evolution of SDS molecules on the surface of a cylindrical droplet. These images illustrate the surfactant spreading along the upper hemisphere of the droplet, and subsequent frames exclude the droplet for enhanced

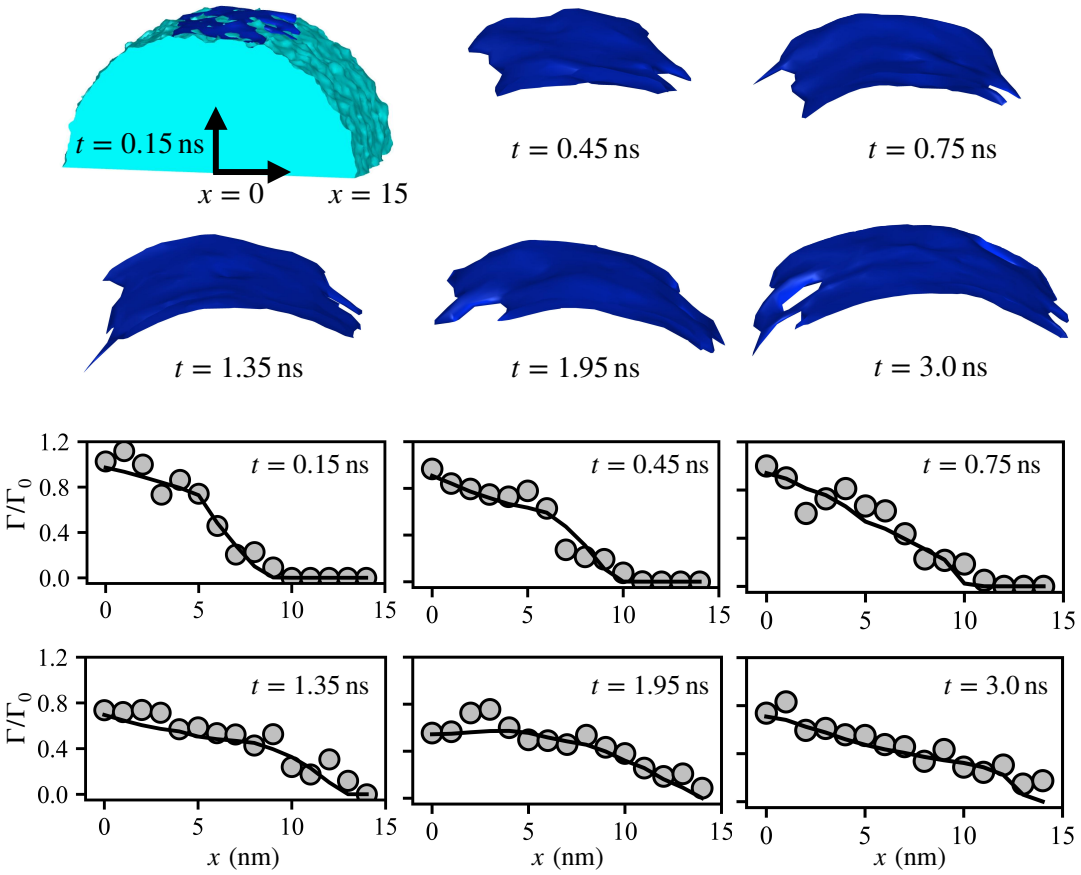


Figure 6.7: Temporal variation of surfactant concentration for the case of a droplet with where 0.2 ng of SDS was deposited at the top and bottom surfaces of the droplet. Data from molecular dynamics (MD) simulations are represented by symbols, while the solid lines indicate the numerical solutions to the transport equation.

clarity of the surfactant layer. The lower two panels of Fig. 6.7 present the spatial variation in surfactant concentration, with discrete symbols indicating data points from molecular dynamics (MD) simulations and solid lines depicting solutions to the corresponding transport equations. Similar to the horizontal film case, the transport equation is seen to closely follow the MD data. Although a droplet has a higher global curvature than the planar films, it is evident that the transport mechanism

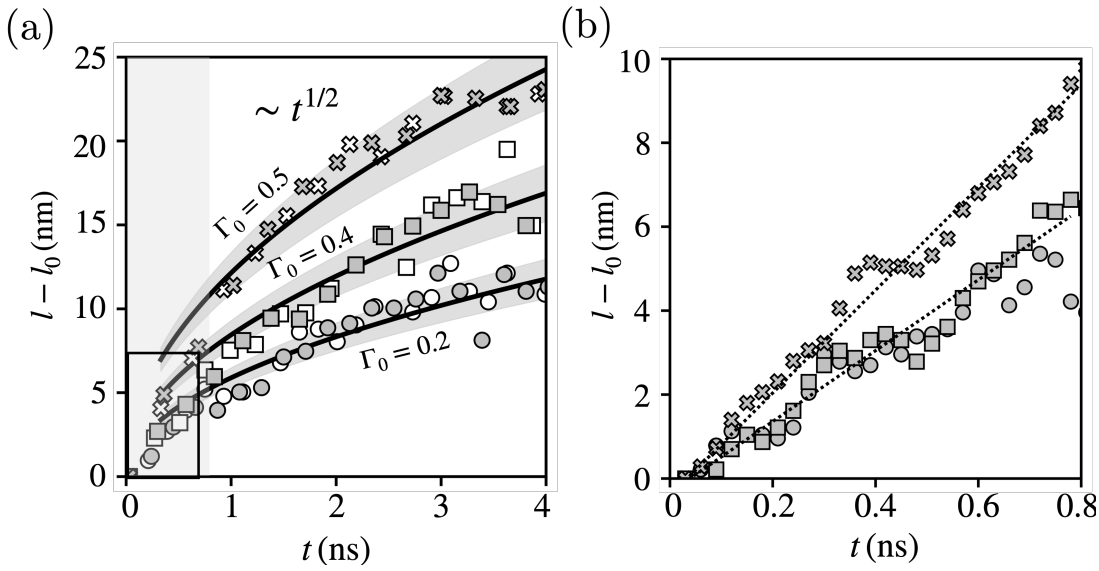


Figure 6.8: (a) Spreading of monolayer: symbols denote MD data, with empty and solid symbols denoting independent simulations. Solid lines show $l \sim t^{1/2}$ fitting to the data. Shaded region shows 90% confidence interval of the fitting. (b) Zoomed in view of the initial rapid transient period (boxed in panel b) showing the early time (linear) spreading.

remains largely unaffected. The local curvature, although consistently minor across the simulations, causes subtle fluctuations which warrant further study, particularly in their potential to highlight non-linear responses at higher surfactant concentration. The coherence between the MD simulations with the continuum model allows to propose a molecular version of the transport equation, which has been described in Appendix B.

6.6 Spreading Length

A more pragmatic parameter to characterize surfactant transport is the spreading rate which essentially denotes the rate at which the front of the surfactant layer spreads across the liquid-vapor interface. The presence of a monolayer creates a difference in surface tension across the interface of the underlying liquid layer, i.e., lower surface tension at the surfactant rich regions, and higher surface tension in surfactant poor

regions. This gradient of tension, i.e., the surface pressure, Π, drives the spreading of the monolayer. The spreading must overcome the viscous drag, and by balancing these two forces Ahmad and Hansen (1972) presented a simplified scaling law for the spreading length, l, which has the form, $l \sim t^{1/2}$. Despite the simplicity of that model, good agreement with experimental results of spreading monolayer was observed. Borgas and Grotberg (1988) derived a similar power-law dependency between l and t, via a more formal analysis by solving the Navier-Stokes equation including the lubrication approximations, taking into account the surface tension gradients, and the viscous dissipation within the thin liquid film underlying the monolayer. Fig. 6.8 (b) shows that the spreading of a surfactant monolayer follows the predicted characteristic square root of time dependence for a range of initial concentrations. This observation agrees with experimental studies by Hanyak et al. (2012) for soluble surfactants SDS spreading on deformable liquid surfaces, obtaining an average exponent of 0.48 for various surfactant concentrations. A similar power law dependency was also observed for isopropyl alcohol-water system (Hernández-Sánchez et al., 2015). This and other studies on spreading (Howell and Stone, 2005; Mitra and Mitra, 2016; Motaghian et al., 2022) demonstrate the importance of the power-law description of the spreading evolution. The exponent may assume a range of values depending on the geometry of the problem, and the physicochemical properties of the liquids involved, such as viscosity, surface tension, miscibility, and surface roughness (Rafaı and Bonn, 2005; Santiago-Rosanne et al., 2001).

While the $t^{1/2}$ rate dependence persists over the rage of simulation time window in the present study, the initial spreading ($t < 0.5\,\text{ns}$) appears to be relatively faster with the exponent $n \to 1$, see panel (c) for a zoomed view of the initial spreading period. This local ballistic or atomistic-scale relaxation behavior may be a unique feature of the full atomistic description provided by MD (Alder and Wainwright, 1967), although its origin is still not entirely clear and would be worthy of further investigation. Similar accelerated initial spreading was also observed in several previous studies (Mitra and Mitra, 2016; Motaghian et al., 2022).

6.7 Summary

This study reconciles the continuum model of surfactant transport with empirical data from non-equilibrium molecular simulations, validating the continuum model's efficacy even at the most fundamental scale. The advection-diffusion equation, a cornerstone of fluid mechanics, is affirmed to be an effective descriptor of the complex interfacial behaviors studied here. The findings highlight the key significance of considering the local and temporal variations of the surface fluxes, surface deformation, and the local gradients of surfactant concentration in modeling the transport of surfactant monolayer. The agreement between the outcomes of the molecular dynamics simulations and the continuum model validates the latter's applicability for nanoscale phenomena - a domain where the continuum framework often reveals its limitations.

This page intentionally left blank.

Sooner or later these ideas will be proven wrong, that's no surprise, nor is unusual, rather that's how science progresses - moving from more incorrect to less incorrect.

7 Conclusion

7.1 Key Findings

This thesis systematically investigates the interfacial dynamics, rupture mechanisms, and surfactant transport phenomena in thin liquid films through a series of detailed studies employing non-equilibrium molecular dynamics (NEMD) simulations, supplemented by other numerical schemes. The central question asked in this thesis is whether the continuum based equations hold in describing nanoscopic flows. In Chapter 5, the Taylor-Culick theory is examined, and is extended for the retraction of molecularly thin films. Chapter 6 critically examined the applicability of the advection-diffusion equation for surfactant transport on a deforming liquid film. The preceding chapters set the scene, develops the methodologies required to test the theories at the fundamental scale. The research described in this thesis identifies the necessary details at the small-scale which needs to be accounted for, and provides intriguing insights that the mean-field theories cannot capture. A brief discussion on the key findings follows.

7.1.1 Surface Structure and Surface Tension

Chapter 3 analyses the liquid-vapor interface of a Lennard-Jones fluid and provides insights into the mechanical basis of surface tension and its dependency on temperature. By utilizing non-equilibrium molecular dynamics simulations with an intrinsic sampling method, we achieved the sharpest view to examine the outermost molecular layer of the liquid-vapor interface. This enabled a careful analysis of surface properties and stress distributions. By identifying and mapping stress clusters within the intrinsic surface layer, we established that these clusters' configuration and stability, influenced markedly by temperature changes, serve as reliable predictors of surface tension variations. A key contribution of this chapter has been the introduction of the concept of percolating stress network. By applying percolation theory and fractal analysis, we showed that the liquid-vapor interface can be perceived as a connected network of stresses. The degree of this 'connectedness' diminishes with increasing temperature, leading to a corresponding decrease in surface tension. This insight provides a new perspective on interfacial tension.

7.1.2 Rupture Dynamics of Thin Liquid Films

While the literature on the stability and rupture of thin films abounds, a molecular-scale understanding of the origin of spontaneous rupture, and the subsequent evolution is incomplete. Moreover, previous studies focused mostly on the rupture of films supported on solid or liquid substrates, introducing subtleties and ambiguities arising from the solid-liquid or liquid-liquid interfaces. Chapter 4 and Chapter 5 investigate the origin of film rupture by simulating a freely suspended thin liquid film, removing the contact line dependencies. Chapter 4 depicts the complete life cycle of a film, from hydrodynamic drainage to stochastic nucleation, and finally coarsening. One of the pivotal findings was the identification of a spatio-temporal memory in the rupture process, underscoring the deterministic outcomes arising from stochastic processes. This challenges the traditional understanding of nucleation events and emphasizes the role of the liquid's inherent structure in predicting rupture. Furthermore, this chapter unifies the concepts of spinodal and heterogeneous nucleation, showing that heterogeneous nucleation can occur without defects or impurities. The investigation into the neighbor effects on nucleus growth shows a frustrated growth regime, leading to delayed coalescence and coarsening.

Chapter 5 extends the rupture study to a single isolated nucleus, revisiting the classical Taylor-Culick theory of thin-film retraction. Through NEMD simulations, the atomic-scale origins of the retraction process is uncovered, providing corrections to the existing theory for films below 100 nm in thickness. Key findings include the identification of reduced local surface tension at the film front, influenced by both thermal effects and curvature. Additionally, a previously overlooked transition regime between the retracting film-front and the unperturbed film is identified, necessitating revisions to the classical theory. These corrections offer a more accurate understanding of thin-film dynamics at the nanoscale and pave the way for future research on more complex liquid-vapor systems.

7.1.3 Surfactant Transport Mechanisms

Chapter 6 focuses on the practical implications of surfactant transport on deforming thin liquid films, both planar and droplet-shaped. By solving the continuum-scale

transport equations using a finite difference scheme with inputs from molecular simulations, this chapter provides the first confirmation of the validity of the continuum equation at the nanoscale. This study reveals that Marangoni stress-induced advection dominates the transport mechanism in monolayers with high surfactant coverage, surpassing diffusion and curvature effects. This study further contributes to resolve the long-standing debate on the applicability of continuum models to molecularly thin films.

The insights gained from this thesis are expected to have implications across various scientific disciplines and practical applications. Understanding the stability and rupture of thin films, and the impact of their interfacial dynamics would enhance the ability to model and manipulate myriad processes, such as coating technologies, foaming, lubrication, and emulsification; this can also inspire robust approaches in the fields of micro-fluidics, nanotechnology, materials science, drug delivery, and biological systems where thin films play a crucial role.

AN OVERARCHING SUMMARY

This thesis presents a comprehensive investigation into the potential of non-equilibrium molecular dynamics (NEMD) simulations to uncover novel insights into the complex dynamics of thin films. It further explores the integration of findings from molecular dynamics (MD) simulations with continuum-scale models to achieve a more accurate representation of physical phenomena at the fundamental scale.

Central to this study is the recognition that the local and temporal variations in surface tension, diffusion coefficients, and curvature within the fluid system are critical for an accurate description of thin film dynamics. The research demonstrates that continuum-scale models, when applied to the fluid dynamics at the smallest scales, need to be informed of the detailed spatio-temporal information at the molecular level captured by MD.

The overarching conclusion of this work challenges, extends and improves the traditional treatments of dynamical systems. MD simulations are shown to provide a more complete understanding of thin film dynamics. Hence, this study advocates for a paradigm shift towards a combined or coupled approach, integrating MD simulations with continuum models to provide a more holistic and encompassing description of the film dynamics without missing the essential details at the nano-scale.

7.2 Future Works

All models are wrong, but some are useful. - George Box

7.2.1 Improvements to Current Work

The research presented in this thesis is subject to certain limitations that, if addressed, could broaden the scope and applicability of the findings. Specifically, the studies on film rupture outlined in Chapters 4 and 5 were conducted using Lennard-Jones systems. Expanding these studies to encompass real systems, particularly water and water-surfactant systems, could provide valuable insights. It would be particularly instructive to investigate the existence and extent of the memory window observed in Chapter 4 in these real systems, thereby contributing to a more comprehensive understanding of deterministic outcomes from stochastic processes. Rapidly quenching the film states within and outside of the memory would shed light on the inherent structure. Furthermore, in addition to what has been investigated in Chapter 5, systematically perturbing relatively thicker films with incrementally increasing the perturbation would give insights on the rupture strength of the induced noise. Another important contribution to the literature would be to gain deeper understanding on the effect of viscosity in rupture, and in transport mechanism. In particular, MD can serve as a powerful tool for tracking surface layers, thereby enabling us to determine whether the debated concept of surface viscosity plays a crucial role.

In Chapter 6, the water-surfactant system is analyzed using the polarizable MARTINI water model. Although this coarse-grained description has been popular for its simplicity, it notably underestimates the surface tension by almost a factor of two. While the focus of Chapter 6 is primarily on the gradient of surface tension due to surfactant concentration rather than its absolute value, employing a molecular description that provides closer estimates to the experimental value of surface tension of water, i.e., SAFT$-\gamma$ (Lobanova et al., 2015) or the Big Multipole Water (BMW) model (Wu et al., 2011) could potentially amplify the effects of Marangoni-induced advection. Verifying this could be crucial, as it would provide a clearer picture of the interplay between surface tension gradients and the underlying dynamics. Com-

plementary to this, would be an atomistic study of Lennard-Jones fluid with dimers acting as surfactants − such a system would avoid any uncharted uncertainties (i.e., any effect from the coarse-grain description, parameterisation etc.) and would provide clearer and more fundamental conclusions.

7.2.2 Extending to New Ideas

The research presented in this thesis provides insights, at the same time raises important new questions, opening several avenues for future research. Notably, the corrections to the classical film-retraction theory discussed in Chapter 5 not only highlight the significance of small-scale factors, but more importantly establish a direct connection between the molecular dynamics (MD) scale and the macroscopic scale. Additionally, Chapter 6 unites the continuum transport model with coarse-grained molecular dynamics simulations. This integration lays the motivation for developing multi-scale approaches (Ewen, 2017; Smith, 2013) for a wide range of phenomena. In principle, a multi-scale approach involves applying quantum mechanics at the smallest scale, subsequently integrating its results into the investigation at the next scale, i.e., molecular dynamics (MD) simulations. Findings at the MD scale can then inform continuum-scale models by providing crucial information of local variations (as in Chapter 5), and the accurate initial and boundary conditions (as in Chapter 6). This hierarchical methodology has the potential to significantly enhance investigative approaches, offering robust and detailed insights while reducing computational costs. Consequently, this approach provides experimentalists and theoreticians with valuable and unprecedented information across multiple scales, fostering a deeper understanding of complex systems.

7.2.3 Soluto- and Thermo-capillary Flows for Self-Propulsion

A natural extension of the study described in 6 involves a comprehensive investigation of soluto-thermo capillary flows. These flows emerge from gradients at interfaces, with the type of gradient determining the nature of the flow. For instance, Marangoni flow (or, soluto-capillary flow) arises from concentration gradients, and thermo-capillary flow is driven by thermal gradients along the interfaces. Recent investigations have

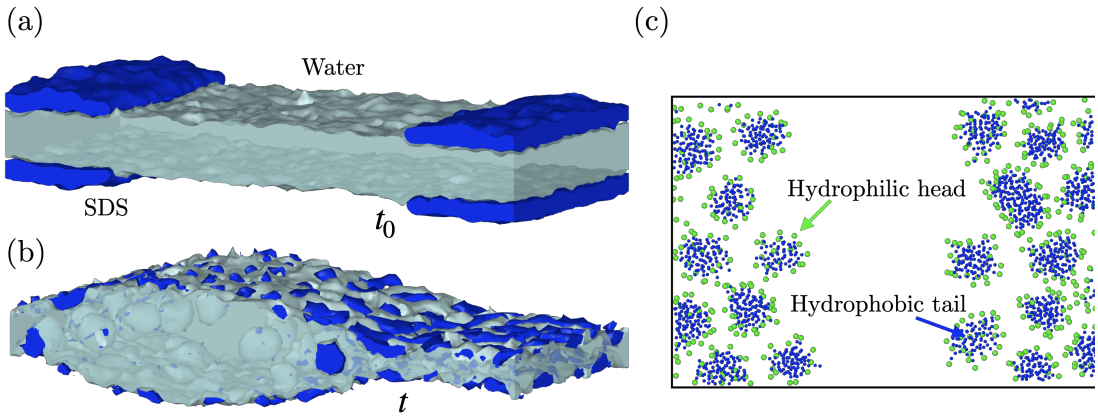


Figure 7.1: Micelle generation: (a) surfactants initially placed at the edges of a thin film, (b) migration of surfactant molecules in the bulk leads to formation of micelles. (c) top view of the micelles.

provided valuable insights into these phenomena (Basu and Gianchandani, 2007; Benouaguef et al., 2021; Gao et al., 2021; Johansson et al., 2022).

In Chapter 6, surfactant redistribution is studied where film thickening is observed at surfactant poor regions, and the surfactant rich regions underwent consistent thinning. While Marangoni stress-induced convection was present, the primary emphasis was on elucidating the underlying transport mechanisms. It would be fruitful to extend this analysis to explicitly investigate the dynamics of Marangoni convection and ascertain its impact. Understandings the soluto-capillary flow is imperative for adding the next layer of complexity, i.e., the introduction of a thermal gradient, through a heat source or sink. Together, these would significantly advance our understanding of nanoscopic flows, in particular Marangoni driven self-propulsion (Masoud and Stone, 2014). These types of flows being highly complicated to address by theoretical investigations, or by CFD, molecular dynamics simulations would prove revealing.

7.2.4 Micelle generation for Targeted Drag Delivery

The transport mechanism of SDS monolayers is examined in Chapter 6, when positioned at the center of an extended film (or, on a droplet), allowing the surfactant molecules to sufficiently cover the surface area. However, reducing the film length

or increasing the amount of surfactant results in a substantial number of surfactant molecules migrating into the bulk phase, thereby promoting micellization. Figure 7.1(a) presents a thin film with a thickness of 10 nm and a length of 50 nm, where surfactant monolayers are initially placed at the two edges, as opposed to the central placement discussed in Chapter 6. After a few time steps, as depicted in panel (b), surfactants redistribute across the surface. Marangoni convection induces fluid flow from the edges towards the center of the film, leading to edge thinning and central thickening. Simultaneously, a significant quantity of surfactant molecules enters the bulk phase, forming micelles that are subsequently driven towards the central region of the film. A top view of the central region illustrates the presence of these micelles. This observation might inspire careful future investigation, since gaining a control mechanism on micelle generation and their directional flow would significantly benefit the nanotherapeutic approach for the targeted delivery of hydrophobic chemotherapeutic agents - a powerful strategy in the treatment of cancer and tumor cells (Ghosh and Biswas, 2021).

The above discussion is far from complete. Understanding the nature of the interface and the transport mechanisms opens numerous possibilities for addressing long-standing challenges in practical applications, including but not limited to aeration in high-speed engines, bubble entrainment, and various biomedical, microfluidic and nanofluidic devices. With the advancement of technology, it is anticipated that the barrier of computational expense will gradually diminish, thereby enhancing the relevance of these studies at even larger scales. A perhaps 'overly-enthusiastic' blue-sky goal could be testing the concepts of network-map, and the stochastic-to-deterministic transition in social dynamics.

A

Appendix to Chapter 4

A.1 Nuclei Growth

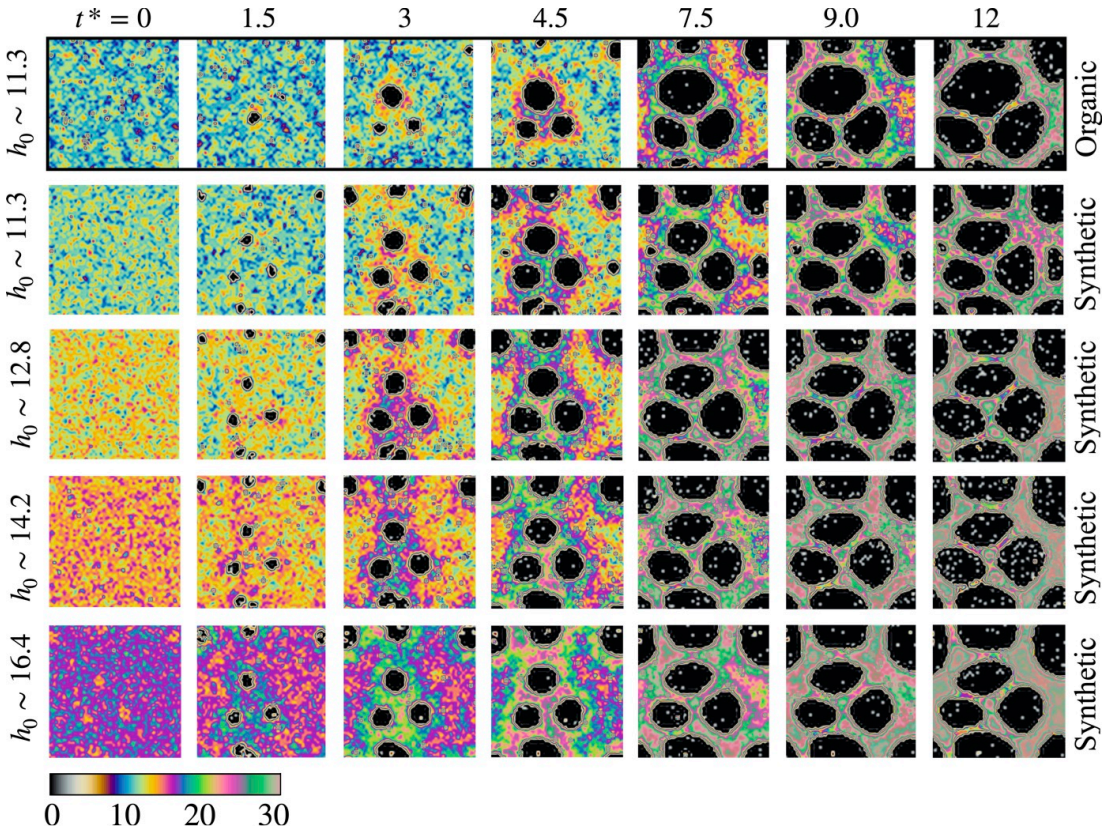


Figure A.1: Spontaneously formed (top row) and synthetically generated (other rows) nuclei on films of various thicknesses show similar evolution pattern over non-dimensional time, $t^* = (t - t_n)/\tau_i$; τ_i is the inertial time scale. The synthetic nuclei were generated in a controlled way to maintain $R_0/h_0 \sim 0.8$.

The locations of the center of the spontaneously formed nuclei of 1st row in Supplementary Fig. A.1 on a film of thickness, $h_0 \sim 11.3$ were identified and, were later used to generate synthetic nuclei at the same locations on thicker films. The time-sequence of spontaneous nucleus formation was removed by nucleating the holes at the same time. While generating the synthetic nuclei, the initial radii were chosen such that $R_0/h_0 \sim 0.85$. Once formed, the nuclei grow at the so-called Taylor-Culick speed which depends on the film thickness, until the neighboring nuclei are grown enough

to start interacting with each other, when the growth slows down and deflect from the linear Taylor-Culick speed. The thickness dependence of the growth dynamics is removed by normalizing the time by the inertial time scale, $\tau_i = \sqrt{\rho h_0^3/2\gamma}$. Irrespective of the initial thickness, h_0, the nuclei in each of the films grow in the exact same fashion, except for $h_0 \sim 11.3$ where a new nucleus emerges spontaneously within the simulated time-window. Supplementary Figure A.2 shows later stages of growth where the nuclei coalesce leading to fragmentation of the film into droplets.

Apparently, films with varied h_0 would show identical evolution if the time and location of nucleation were same. It is the spatio-temporal distribution of nucleation that results in differences in film evolution.

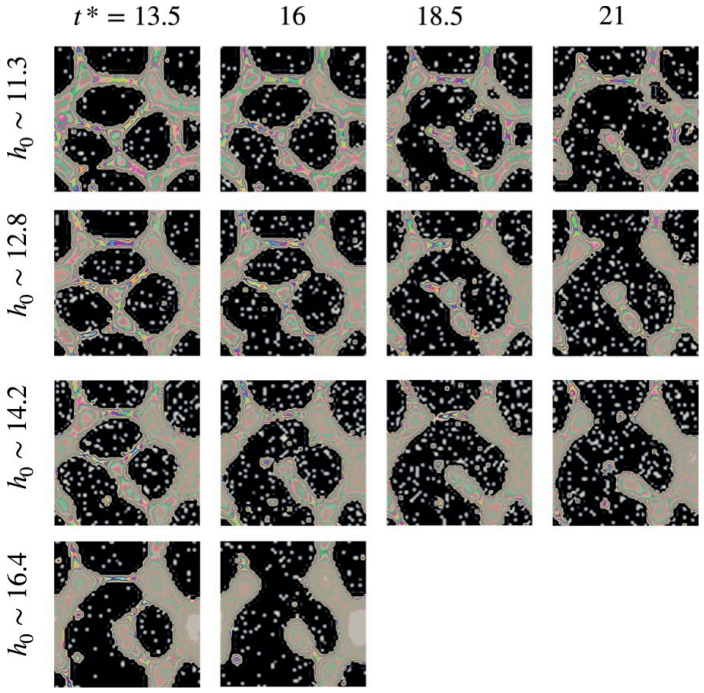


Figure A.2: Transition to coalescence regime: nuclei in a relatively thicker film coalesce earlier than those in a thinner film.

The 'undisturbed' growth of a nucleus is highly affected once it come to close proximity of surrounding nuclei. The scarceness of space to grow, and the increasing thickness of the surrounding liquid between the neighbors frustrates the growth and the nucleus is squeezed - indicated by the deviation of the circularity of its shape.

When two neighboring nuclei come in close contact to each other, the likelihood of coalescence increases with their sizes as two larger nuclei will share larger contact area in the direction normal to the film-surface. The liquid trapped within the two nuclei can then be thought of another freely suspended film but spans across the direction along the thickness of the parent film. As the lateral dimension of this 'trapped' film increases both with the film thickness and the size of the nuclei, larger nuclei and in thicker films, are more prone to rupture as compared to smaller nuclei and thinner films. Indeed, these trapped films are essentially a fractal version of the parent film, so one can expect similar behavior, but in a smaller length and time scale. As seen from the top row of Supplementary Fig. A.2, the growth of the nuclei, their coalescence and subsequent growth results in long liquid threads (Verma and Sharma, 2007), which can be considered as films along the normal direction, these soon break due to the Rayleigh instability.

A.2 Rupture Memory

Figure A.3 shows another instance of the memory-effect of film rupture, in addition to what has been described in earlier in Chapter 4. Multiple independent simulations nucleate at the identical spot until approximately $t_n \sim 401$. However, delving further back in time (i.e., $t < 401$), differences arise both in spatial distribution and nucleation timing. It is important to note that the memory window differs between the two investigated cases (~ 100 *vs* ~ 50 LJ time units), but in both cases, the span of the memory window exceeds the numerical correlation time of the molecular simulation. An analogy for the concept of inherent structures is illustrated in Fig. A.4.

A.3 Neighbor Effect on the Rupture Propagation

It is rare, if not impossible, to find a film where the rupture sites are isolated. Indeed, and as can be seen in the films presented in the figures of the manuscript, multiple sites on the film rupture almost simultaneously. For relatively thicker films, the rupture sites are more sparsely distributed than for thinner films, but upon expansion, the rim of these distant nuclei come close to each other effecting the growth of other nuclei.

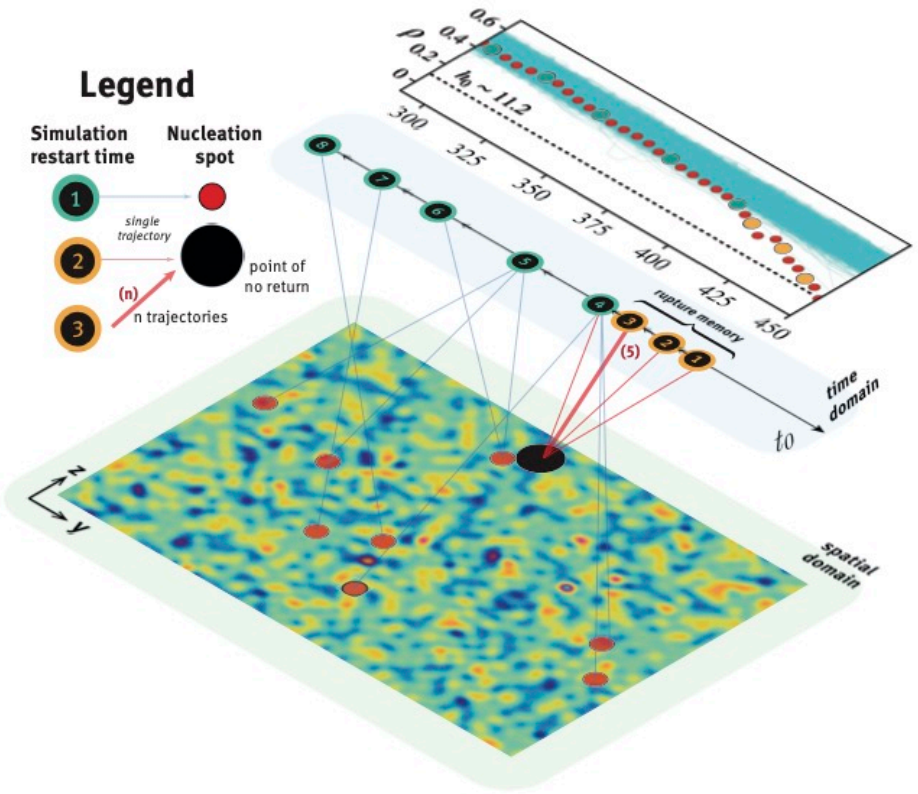


Figure A.3: In addition to the film detailed in the manuscript Figure 3, a repeat examination of an independent simulations (which originally nucleates at $t \sim 450$) is carried out (bottom density plot and the related connection lines). Similar to what is described in the MS, connection lines to the nuclei are red when a restarted case nucleates at the same location as of the original film (white circle on the film), and blue otherwise.

As can be seen from Fig. A.5 (a-d), the growth of each of the nuclei is effected due to the presence of the neighbors. And, such effect is seen to be a function of the relative size, location and the number of neighbors. In panel (a), the two nucleus share nearly equal effect from each other, but in panel (b), where one nucleus is significantly aged (hence, larger) than the other, the larger nucleus is seen to push the smaller one. In panel (c), the greatest impact is on the central nucleus which is squeezed by the two side-nuclei. In contrast, in panel (d) each of the three nuclei effect each-other equally.

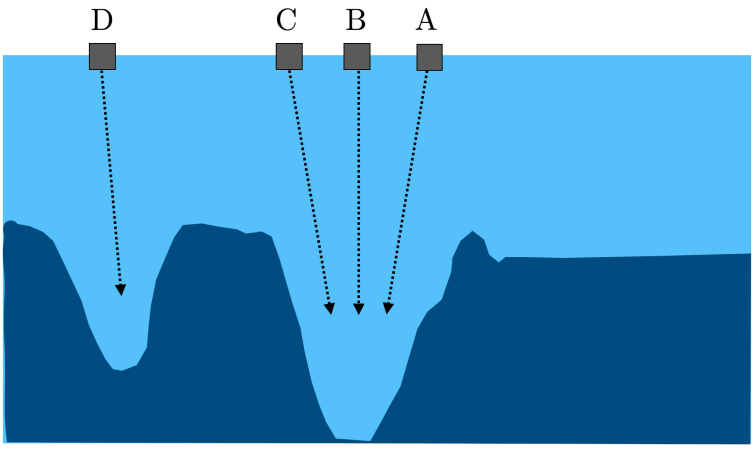


Figure A.4: An analogy for the concept of inherent structures in a potential energy landscape. If a ship is positioned at points A, B, or C, quenching the water instantaneously would cause the ship settling into the same depression or "well" in the seabed. However, a ship located at point D would fall into a different abyss, illustrating that despite proximity, distinct energy basins may exist.

It can be realized that depending on the time and location of nucleation, an infinite set of possibilities may occur. In this study, we systematically examine few simplified but representative cases that presents an understanding of the over-all neighbor effects.

Maximum Number of Neighbors

For simplicity, we assume N nearest-neighbors nuclei each of radius, r surround a central nucleus, C_c of radius R, and $R(t_0) = r(t_0)$. If the nn nuclei are uniformly located at a distance l from the center of C_c, the maximum possible number of neighbors of radius, r can be obtained as:

$$N_{\max} = \frac{\pi}{\sin^{-1}(r/l)} - 1 \tag{A.1}$$

This, however, refers to a situation where the neighbors are densely packed, i.e., they touches their side nuclei without overlapping, see Fig.A.5 (e). Note, in situation like this, $N_{\max}$ varies with the center-to-center distance, l, i.e., $N_{\max} = N(l)$. Further, since the neighbors themselves would grow over time, if such a situation arises, they

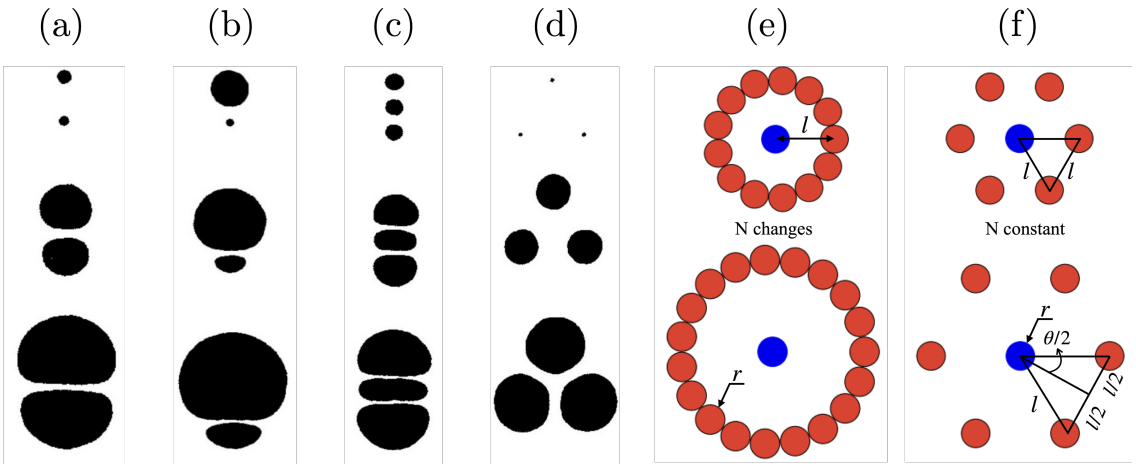


Figure A.5: (a-d): Effect of neighbors on the shape and size of a nucleus: two nuclei where one nucleates (a) slightly earlier than the other, (b) substantially earlier than the other. Three nuclei that nucleate at the same time located (c) on the same axis, (d) on the vertices of an equilateral triangle. (e-f): Schematic of a central nucleus surrounded by neighbor nuclei. (e) densely packed case where neighbors touch but do not overlap onto each other, (f) center-to-center distance between two neighbors equals the center-to-center distance between the central nucleus and the neighbor nucleus. For both panels, the distance between the central and the neighbor nuclei is increased by nearly 50%. For (e) $N = 6$ only when $l = 2r$, whereas, for (f) irrespective of the magnitude of l, $N = 6$.

will rather coalesce with each other before the central nucleus is effected.

A different arrangement is shown in the top and bottom rows of panel (f), where the distance between the central and any of the neighbor nuclei is equal to the distance of any two neighbor nuclei. If such a condition is imposed, (i) the neighbor nuclei would affect each-other only when they also start affecting the central nucleus, and (ii) any pre-mature coalescence can be avoided. With such an arrangement, the maximum number of neighbor nuclei can be obtained from the geometry:

$$N_{\max} = \frac{\pi}{\sin^{-1}\left(\frac{l/2}{l}\right)} \tag{A.2}$$

As evident from Eq. A.2, $N_{\max}$ is independent of l and assumes a value of 6. This is portrayed in Fig. A.6 where 8 neighbor nuclei surrounds a central nucleus. Initially,

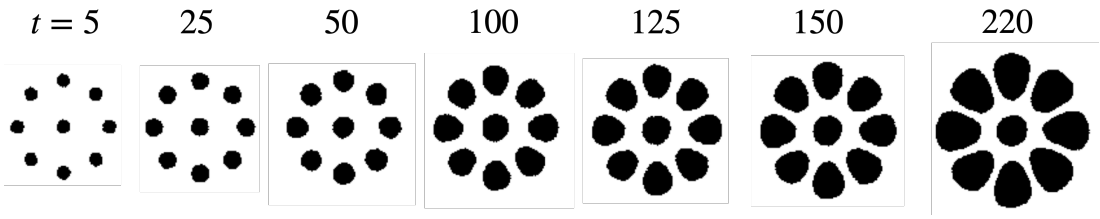


Figure A.6: Evolution of a central nucleus surrounded by 8 neighbor nuclei initially located at equal distance from the central nucleus. After initial growth, the central nucleus is seen to suffocate to grow and eventually reaches a stagnant shape. Time is in MD units.

all the nuclei are seen to grow in similar fashion. However, one can notice that after $t \geq 100$, the growth of the central nucleus is slowed and later almost stopped, while the neighbour nuclei keep growing and effecting each other.

A.4 Further Details and Discussions

A.4.1 Spinodal and nucleation processes

For metastable films, dewetting can occur by (i) nucleation and subsequent growth. The accumulation of materials around the hole's perimeter gives rise to the formation of an elevated structure, also known as rim. The second mechanism, characteristic to unstable films (Bollinne et al., 2003), is the (ii) spinodal rupture which is an instability driven spontaneous process. This instability in question arises from the thermally activated surface waves (Bischof et al., 1996), i.e., through the amplification of capillary waves. The number density of the initially formed holes was observed to display h^{-4} dependency as an indication of surface instability (Reiter, 1992). Similar dependency is also evident from Figure 4.5, panel (f). However, such correlation for the spatial distance between the holes has been contradicted (Jacobs et al., 1998). While holes by nucleation exhibit circular shape, those formed due to spinodal instability are irregular.

Thiele et al. (1998) investigated, by scanning force microscopy, the dewetting during on-going thinning (due to evaporation) of collagen solution on a solid substrate. From the distribution of the hole sizes, the authors observed a pronounced bimodality for thinner films (films evaporating at lower humidity, hence higher evaporation rate resulting in thinner film) indicative of two distinct mechanisms. Au contraire, the thicker films (films evaporating at higher humidity) exhibited unimodal distribution shifted towards larger holes - this was attributed to nucleation. Besides the size of the holes, a common perception in the literature to distinguish between the two mechanisms is based on the stability of the film, assigning rupture in linearly unstable films to spinodal process, whereas, those in metastable films are attributed to nucleation. Thiele et al. (2001), however, showed that these two distinct mechanisms can indeed occur and overlap within the unstable regime.

In Figure A.7, we examine whether the distribution of hole sizes reveals a unimodal pattern (distribution with a single peak) typically associated with nucleation-driven dewetting—or a bimodal pattern (which exhibits two peaks) - characteristic of the

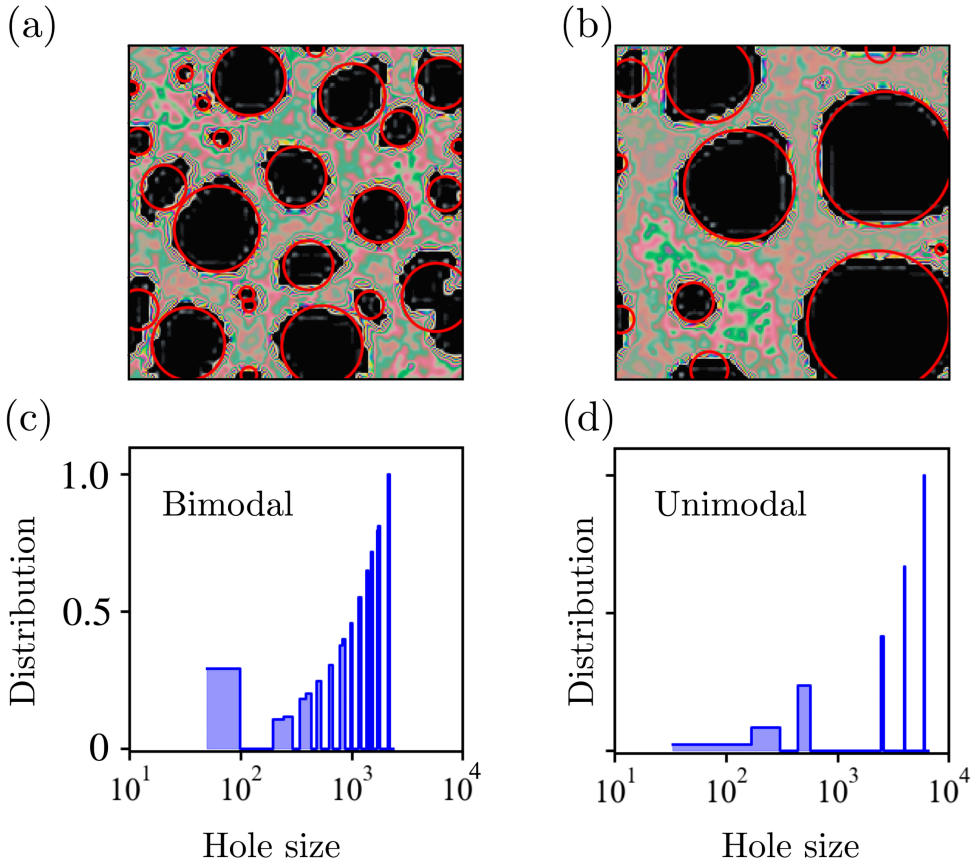


Figure A.7: Thickness maps (top panels) and corresponding hole size distributions (bottom panels) of dewetting films with initial thickness, h_0: (a,c) ~ 9.5, and (b,d) ~ 11.5. Holes are marked by red circles.

presence of two distinct mechanisms. This is achieved through identifying the holes, categorizing the hole areas into bins, with the average area per bin forming the basis for computing the distribution function (Thiele et al., 1998). The top panels in Figure A.7 presents thickness maps for films of varying initial thicknesses ($h_0 \sim 9.5\,\&\,11.5$) before the onset of coalescence. In the bottom panels, the corresponding normalized hole size distributions are shown. These distributions reveal that thinner films exhibit pronounced bimodality, see, panels (a,c). In contrast, a relatively thicker film in panels (b,d) displays unimodal size distribution.

Notably, despite the morphological similarities, when spinodal process was studied for a liquid film supported on a liquid substrate, Shiri et al. (2023) observed distinct behavior, both in rupture time and in wavelength, as compared to films on solid-substrate, mainly due to the absence of contact line singularities. As such, in a free standing film (as in present study) which incorporates two free liquid-vapor surfaces, variations from solid-liquid or liquid-liquid cases are expected. Therefore, and because of the system size and the periodic boundary conditions applied in our simulations, we refrain from making any definitive statement on the distinction between the processes, and defer this for future studies.

A.4.2 Thickness Measurement from MD Data

The time-evolving local thickness of the films are measured by employing a peak-to-peak analysis by identifying the liquid and the vapor phases. First, a binary representation (where liquid and vapor regions are differentiated) is created from the density field based on a density threshold. Then, to locate the liquid-vapor interfaces, the gradient of this representation is calculated along the direction normal to the film. The distance between these interfaces (top and bottom surfaces) corresponds to the peak-to-peak thickness. See Figure A.8.

A.4.3 Undulation at the Upper and Lower Surfaces of a Film

Fig. A.8 panels (a-f) shows the growing undulation at both lower and upper surfaces of a film. Initially corrugations are small in magnitude (a), which soon start growing (b). The continued growth leads to eventual rupture, i.e., formation of holes (c) followed by subsequent growth, as well as new rupture events (d-f). The peak to peak thickness measures the spatio-temporal distance between the two surfaces as explained earlier - this is shown in panel (g).

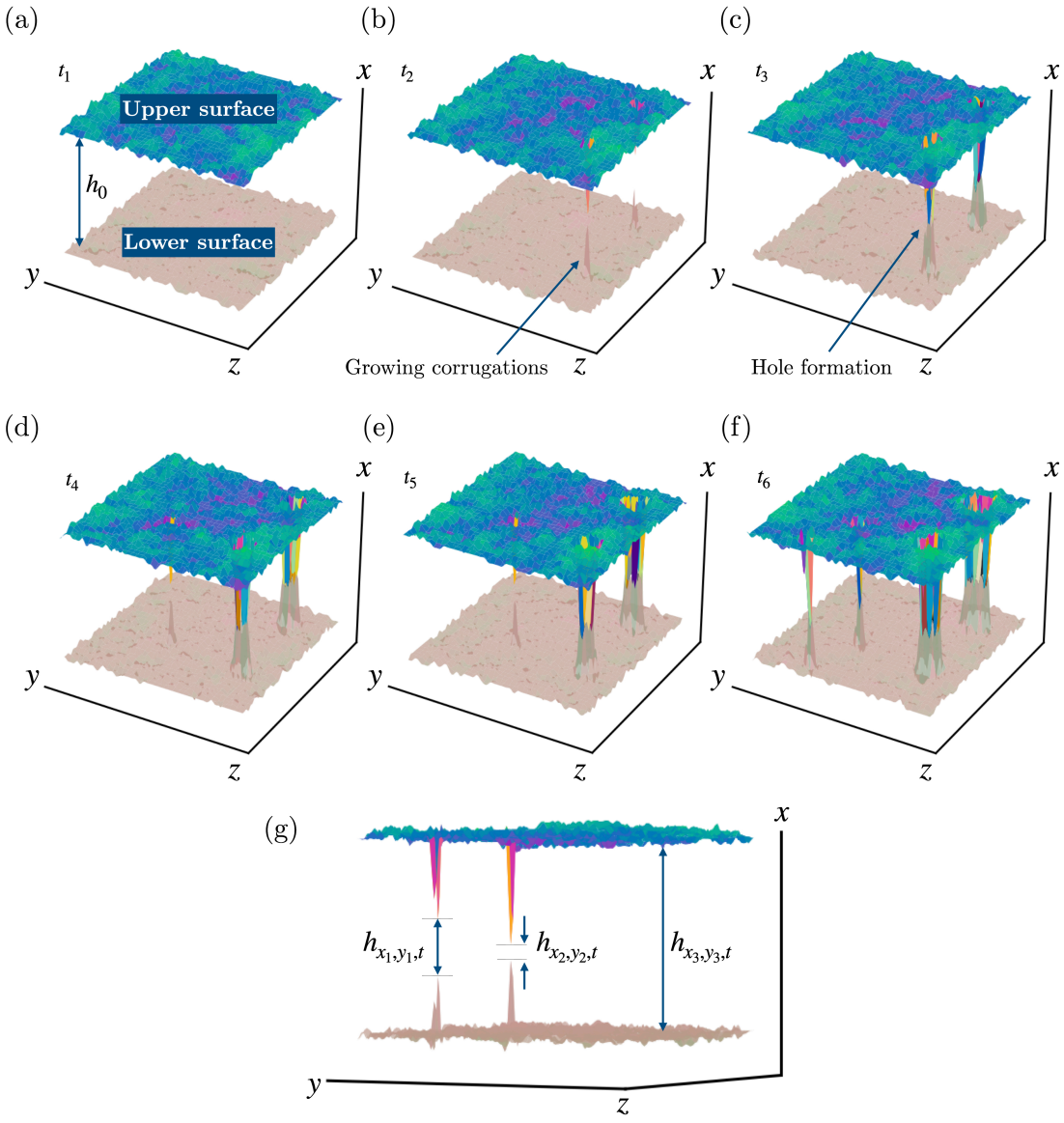


Figure A.8: (a-f) Growth of corrugations at the lower and upper surfaces of a thin film leading to rupture - images are not to scale, also the x axis is exploded for better visual along the direction of film thickness. (g) Side view of the film shows local peak-to-peak thickness, $h(x, y, t)$.

B

Appendix to Chapter 6

B.1 A molecular version of the transport equation

The coherence between the MD simulations with the continuum model allows us to propose a molecular version of the transport equation as*:

$$\sum_{i=1}^{N_S}\Bigg[\underbrace{\frac{1}{J_i}\frac{d}{dt}\left(m_i\vartheta_i J_i\right)}_{\text{unsteady}}-\underbrace{m_i\dot{u}_i dS_{ui}}_{\text{advection}}-\underbrace{m_i\vartheta_i\frac{\dot{J}_i}{J_i}}_{\text{geometric effect}}-\underbrace{m_i\dot{v}_i dS^-_{vi}}_{\text{source term}}\Bigg]=0 \tag{B.1}$$

Here, u and v are mapped coordinates following, respectively, the tangential and normal directions to the interface $\zeta(x,t)$ at every point. The function $\vartheta_i=\Lambda_u\Lambda_v$ is the control volume function, which select molecules inside the Heavisides with value one when molecule i is in the volume and zero otherwise.

Here, $\Lambda_u=[H(u^+-u_i)-H(u^--u_i)]$, and $\Lambda_v=[H(v^+-v_i)-H(v^--v_i)]$ each representing a boxcar function, H is the Heaviside function, superscripts $+,-$ denote positions of top and bottom surfaces in mapped space with molecular surface crossings captured by $dS_{ui}=dS^+_{ui}-dS^-_{ui}=\delta(u^+-u^-)-\delta(u^--u_i)$ and J_i is the Jacobian at the position of particle i. The underbraces identify the equivalence between terms to the continuum equation 6.1, the unsteady term is the change in time of the molecules in a volume, the advection is the derivative in the tangential direction of velocity along the tangent, which can be seen to be equivalent to the continuum differential form in the limit of zero volume $\Delta u\to 0$, so $dS_{ui}=\frac{\partial}{\partial u}\delta(u-u_i)\Lambda_u$ and $\frac{\partial}{\partial u}\sum_{i=0}^{N_S}m_i\dot{u}_i\delta(u-u_i)\delta(v-v_i)=\nabla_{\mathbf{s}}\cdot\Gamma\mathbf{u}_{\mathbf{s}}$. For the source term in (B.1), is flow from the bulk to the surface assuming no surfactant molecules leave the surface, hence $\sum_{i=0}^{N_S}m_i\dot{v}_i dS^+_{vi}=0$. The geometric effect is given by the time-derivative of the Jacobian, i.e., $\dot{J}_i$, measuring the effect of the deforming volume in time. There is no obvious diffusion contribution obtained by this treatment, which is consistent with Scriven and Sternling (1960b), although it might be possible to justify a diffusion like effect through consideration of Ficks law style flux and the interaction with the non-surfactant molecules, this is not considered here.

*This has been derived by Edward R. Smith, and has been described in full length in Rahman et al., Nanoscale Surfactant Transport: Bridging Continuum and Molecular Models (in preparation).

C

General Appendix

C.1 Some definitions in MD simulations

Molecular dynamics (MD) is a computational technique used to model the behavior of atoms and molecules by solving Newton's equations of motion. It involves tracking particles in a simulation box by calculating forces between them based on interaction potentials, such as the Lennard-Jones or Coulomb potentials. These forces are used to compute the accelerations of particles, which are then integrated over time using numerical methods, e.g., *Velocity-Verlet* or *Leap frog* algorithms. The positions and velocities of particles are updated at each time step, forming a trajectory through phase space, which is the combination of positions and momenta of all particles. To avoid boundary effects, periodic boundary conditions are often applied, meaning that particles exiting one side of the simulation box re-enter from the opposite side. The system is typically first equilibrated to reach a stable state. The purpose of equilibration in molecular dynamics (MD) simulations is to allow the system to reach a

stable, balanced state before collecting data for analysis. At the start of a simulation, the system's particles may have random or unrealistic positions and velocities. During equilibration, the particles move and adjust based on the forces acting on them, until they settle into a state of the desired temperature, pressure, and overall energy of the system. This is followed by a production phase where properties such as temperature, pressure, and energy are recorded.

C.1.1 Thermostats

Thermostats are used to control the temperature of a system being simulated. Of several available thermostats, the Nosé-Hoover thermostat (Hoover, 1985; Nosé, 1984) is a widely used thermostat that efficiently maintains a constant temperature while not affecting the natural dynamics of a evolving system. The system is coupled to a 'virtual' heat bath, which interacts with the system to regulate its temperature. The key idea is to introduce an additional dynamic variable, $\xi(t)$, which evolves over time and adjusts particle velocities by accelerating or decelerating them until the specified temperature is attained. Essentially it acts as a fictitious friction parameter. The equations of motion in the Nosé-Hoover thermostat are:

$$\dot{\mathbf{r}}_i = \frac{\mathbf{p}_i}{m_i}$$

$$\dot{\mathbf{p}}_i = \mathbf{F}_i - \xi \mathbf{p}_i$$

$$\dot{\xi} = \frac{1}{Q}\left[\sum_{i^N} \frac{\mathbf{p}_i^2}{2m_i} - \frac{3N+1}{2} k_B T\right]$$

where $\mathbf{r}_i$ and $\mathbf{p}_i$ are respectively, the position and momentum of particle i, Q controls the strength of the thermostat coupling, T is the target temperature. $3N+1$ instead on $3N$ is due to the added degree of freedom, ξ, and k_B is Boltzmann's constant. Variable ξ adjusts the particle momenta over time, allowing the system's temperature to fluctuate around the desired value while maintaining the natural dynamics of the system. Unlike simpler thermostats (e.g., velocity rescaling), the Nosé-Hoover thermostat conserves the equations of motion such that long-term energy drift is

minimized, making it suitable for equilibrium and non-equilibrium simulations.

C.1.2 Integrator

Originally proposed by Verlet (1967), the Verlet algorithm algorithm has been a widely used integration method in molecular dynamics simulations. The particle position is expanded to the third Taylor series expansion,

$$\mathbf{r}(t+\Delta t) = \mathbf{r}(t) + \dot{\mathbf{r}}(t)\Delta t + \frac{1}{2}\ddot{\mathbf{r}}(t)\Delta t^2 + \frac{1}{6}\dddot{\mathbf{r}}(t)\Delta t^3 + \mathcal{O}(\Delta t^4)$$

$$\mathbf{r}(t-\Delta t) = \mathbf{r}(t) - \dot{\mathbf{r}}(t)\Delta t + \frac{1}{2}\ddot{\mathbf{r}}(t)\Delta t^2 - \frac{1}{6}\dddot{\mathbf{r}}(t)\Delta t^3 + \mathcal{O}(\Delta t^4)$$

Adding the two expansions give,

$$\mathbf{r}(t+\Delta t) = 2\,\mathbf{r}(t) - \mathbf{r}(t-\Delta t) + \ddot{\mathbf{r}}(t)\Delta t^2 + \mathcal{O}(\Delta t^4)$$

It updates particle positions using both the current and previous positions, along with the current acceleration. The position at time $t + \Delta t$ is calculated as:

$$\mathbf{r}(t+\Delta t) = 2\,\mathbf{r}(t) - \mathbf{r}(t-\Delta t) + \ddot{\mathbf{r}}(t)\Delta t^2$$

where $\ddot{\mathbf{r}}(t)$ is the acceleration at time t, and $\mathbf{r}$ represents the position. The Verlet algorithm does not directly update the velocities, but can be approximated afterward as:

$$\dot{\mathbf{r}}(t) \approx \frac{\mathbf{r}(t+\Delta t) - \mathbf{r}(t-\Delta t)}{2\Delta t}$$

An improvement on the Verlet algorithm, known as *Velocity-Verlet*, which explicitly updates both positions and velocities at each time step, i.e.,

$$\mathbf{r}(t+\Delta t) = \mathbf{r}(t) + \dot{\mathbf{r}}(t)\Delta t + \frac{1}{2}\ddot{\mathbf{r}}(t)\Delta t^2$$

$$\dot{\mathbf{r}}(t+\Delta t/2) = \dot{\mathbf{r}}(t) + \frac{1}{2}\ddot{\mathbf{r}}(t)\Delta t$$

$$\ddot{\mathbf{r}}(t+\Delta t) = \frac{1}{m}\mathbf{F}(t+\Delta t)$$

And update velocity at $t + \Delta t$ as:

$$\dot{\mathbf{r}}(t + \Delta t) = \dot{\mathbf{r}}(t + \Delta t/2) + \frac{1}{2}\ddot{\mathbf{r}}(t + \Delta t)\Delta t$$

As clear from the above set of equations, the velocities are updated in two steps: a half-step before computing the new positions and a final half-step after updating the positions. This modification allows for better control and calculation of velocities, making the Velocity-Verlet algorithm more suitable for simulations that require temperature control or kinetic energy calculations.

C.1.3 Reduced units

In molecular dynamics simulations of Lennard-Jones (LJ) systems, it is common to use *reduced units*, where physical quantities are expressed in terms of the characteristic scales of the Lennard-Jones potential (Rapaport, 2004). This non-dimensionalisation simplifies the equations of motion and reduces the number of parameters, effectively increasing simulation efficiency. The Lennard-Jones potential is given by:

$$V_{\mathrm{LJ}}(r) = 4\epsilon \left[\left(\frac{\sigma}{r}\right)^{12} - \left(\frac{\sigma}{r}\right)^{6} \right]$$

where ϵ is the depth of the potential well (energy scale), and σ is the distance at which the potential is zero (length scale). To non-dimensionalise the system, *reduced units* are based on these characteristic values. For example, distance is expressed in units of σ, so the reduced distance is $\tilde{r} = r/\sigma$. Energy is expressed in units of ϵ, the reduced energy being $\tilde{E} = E/\epsilon$. The time scale is non-dimensionalized as $\tilde{t} = t\sqrt{\epsilon/m\sigma^2}$, and temperature is reduced as $\tilde{T} = k_B T/\epsilon$, where k_B is the Boltzmann constant. Using these reduced units, the Lennard-Jones potential becomes:

$$V_{\mathrm{LJ}}(\tilde{r}) = 4 \left[\left(\frac{1}{\tilde{r}}\right)^{12} - \left(\frac{1}{\tilde{r}}\right)^{6} \right]$$

This non-dimensionalization simplifies the MD simulations by eliminating explicit dependence on σ, ϵ, and m, allowing results to be interpreted in a more general framework. For the Lennard-Jones fluid (as in Chapters 3, 4, 5) $\sigma = 3.4 = 3.4 \times 10^{-10} m$, $\epsilon = k_B \times 120 = 1.65 \times 10^{-21}$, $t = 2.161 \times 10^{-12}$ s and, Boltzman constant,

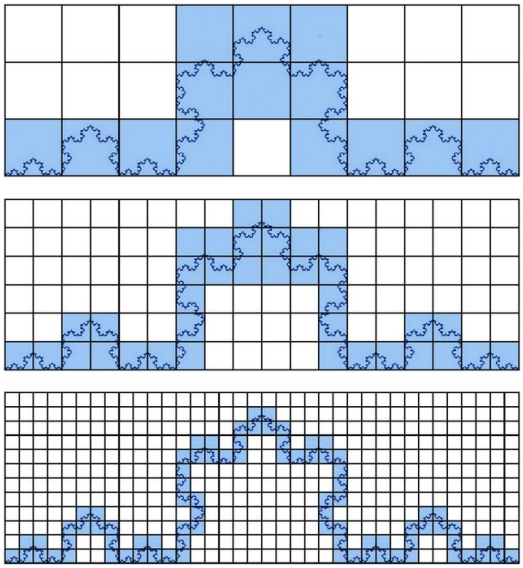


Figure C.1: Fractal dimension by Minkowski or popularly known as box counting method (figure adapted from Pilgrim and Taylor (2018)). The side of the boxes/grids is ς, which is made finer at each iteration and the number of boxes, $N(\varsigma)$ required to cover the fractal object (shaded in blue) is counted.

$k_B = 1.380649 \times 10^{-23} J/K$. In Chapter 6, real units were used for the simulations in LAMMPS, where mass is in units of grams permole, distance in Angstrom, time in femtoseconds, energy in kcal per mol, velocity in Angstroms per femtosecond, temperature in Kelvin, and density in g per cubic centimeter. However, in presenting the results, non-dimensionalized concentration or areal density is plotted, and distance and time are plotted, respectively in the units of nanometer and nonosecond.

C.2 Minkowski dimension

The *Minkowski dimension*, also known as the box-counting dimension, is a method to determine the fractal dimension, Φ. To calculate it, the set is covered by a grid, and the number of boxes $N(\varsigma)$ required to cover the set is counted as the grid becomes finer, (with smaller box size ς, see Fig. C.1). Φ is given by:

$$\Phi = \lim_{\varsigma \to 0} \frac{\log N(\varsigma)}{\log(1/\varsigma)}. \tag{C.1}$$

This page intentionally left blank.

Bibliography

Afsar-Siddiqui, A. B., Luckham, P. F., and Matar, O. K. (2003). The spreading of surfactant solutions on thin liquid films. *Advances in Colloid and Interface Science*, 106(1-3):183–236.

Ahmad, J. and Hansen, R. S. (1972). A simple quantitative treatment of the spreading of monolayers on thin liquid films. *Journal of Colloid and Interface Science*, 38(3):601–604.

Alder, B. and Wainwright, T. (1967). Velocity autocorrelations for hard spheres. *Physical review letters*, 18(23):988.

Allen, M. P. and Tildesley, D. J. (2017). *Computer Simulation of Liquids*. Oxford University Press.

Alvarado, J., Sheinman, M., Sharma, A., MacKintosh, F. C., and Koenderink, G. H. (2017). Force percolation of contractile active gels. *Soft Matter*, 13(34):5624–5644.

Ancey, C. (2007). Plasticity and geophysical flows: A review. *Journal of Non-Newtonian Fluid Mechanics*, 142(1-3):4–35.

Anderson, A. M., Brush, L. N., and Davis, S. H. (2010). Foam mechanics: spontaneous rupture of thinning liquid films with plateau borders. *Journal of Fluid Mechanics*, 658:63–88.

Anogiannakis, S. D., Petris, P. C., and Theodorou, D. N. (2019). Promising route for the development of a computational framework for self-assembly and phase behavior prediction of ionic surfactants using martini. *The Journal of Physical Chemistry B*, 124(3):556–567.

Antonin, M., Joost, W., Snoeijer, J., and Andreotti, B. (2011). Why is surface tension a force parallel to the interface? *American Journal of Physics*, (10):999–1008.

Avnir, D., Farin, D., and Pfeifer, P. (1984). Molecular fractal surfaces. *Nature*, 308(5956):261–263.

Bagchi, B. (2013). *Water in biological and chemical processes: from structure and dynamics to function*. Cambridge University Press.

Ball, P. (2014). The hidden structure of liquids. *Nature Materials*, 13(8):758–759.

Barnes, G. and Gentle, I. (2011). *Interfacial science: an introduction*. Oxford University Press, USA.

Basu, A. S. and Gianchandani, Y. B. (2007). Shaping high-speed marangoni flow in liquid films by microscale perturbations in surface temperature. *Applied Physics Letters*, 90(3):034102.

Becker, J., Grün, G., Seemann, R., Mantz, H., Jacobs, K., Mecke, K. R., and Blossey, R. (2003). Complex dewetting scenarios captured by thin-film models. *Nature Materials*, 2:59–63.

Benouaguef, I., Musunuri, N., Amah, E. C., Blackmore, D., Fischer, I. S., and Singh, P. (2021). Solutocapillary marangoni flow induced in a waterbody by a solute source. *Journal of Fluid Mechanics*, 922:A23.

Berry, M. (1971). The molecular mechanism of surface tension. *Physics Education*, 6(2):79.

Bestehorn, M. and Neuffer, K. (2001). Surface patterns of laterally extended thin liquid films in three dimensions. *Physical review letters*, 87(4):046101.

Bhanvase, B. and Barai, D., editors (2021). *Nanofluids for Heat and Mass Transfer*. Academic Press.

Bhatt, D., Newman, J., and Radke, C. (2002). Molecular simulation of disjoining-pressure isotherms for free liquid, lennard-jones thin films. *The Journal of Physical Chemistry B*, 106(25):6529–6537.

Bickel, T. (2019). Spreading dynamics of reactive surfactants driven by marangoni convection. *Soft Matter*, 15(18):3644–3648.

Bickel, T. and Detcheverry, F. (2022). Exact solutions for viscous marangoni spreading. *Physical Review E*, 106(4):045107.

Bird, J. C., De Ruiter, R., Courbin, L., and Stone, H. A. (2010). Daughter bubble cascades produced by folding of ruptured thin films. *Nature*, 465(7299):759–762.

Bischof, J., Scherer, D., Herminghaus, S., and Leiderer, P. (1996). Dewetting modes of thin metallic films: nucleation of holes and spinodal dewetting. *Physical Review Letters*, 77(8):1536.

Bollinne, C., Cuenot, S., Nysten, B., and Jonas, A. M. (2003). Spinodal-like dewetting of thermodynamically-stable thin polymer films. *The European Physical Journal E*, 12:389–396.

Boltzmann, L. (1872). Sitzungsberichte akad. *Wiss*, 66:275.

Borgas, M. S. and Grotberg, J. B. (1988). Monolayer flow on a thin film. *Journal of Fluid Mechanics*, 193:151–170.

Bourouiba, L. (2021). The fluid dynamics of disease transmission. *Annual Review of Fluid Mechanics*, 53:473–508.

Braga, C., Smith, E. R., Nold, A., Sibley, D. N., and Kalliadasis, S. (2018). The pressure tensor across a liquid-vapour interface. *The Journal of Chemical Physics*, 149(4):044705.

Brenner, M. P. and Gueyffier, D. (1999). On the bursting of viscous films. *Physics of Fluids*, 11(3):737–739.

Bresme, F., Chacón, E., and Tarazona, P. (2008). Molecular dynamics investigation of the intrinsic structure of water–fluid interfaces via the intrinsic sampling method. *Physical Chemistry Chemical Physics*, 10(32):4704–4715.

Bresme, F. and Faraudo, J. (2004). Computer simulation studies of newton black films. *Langmuir*, 20(12):5127–5137.

Buff, F., Lovett, R., and Stillinger Jr, F. (1965). Interfacial density profile for fluids in the critical region. *Physical Review Letters*, 15(15):621.

Bug, A., Safran, S., Grest, G. S., and Webman, I. (1985). Do interactions raise or lower a percolation threshold? *Physical Review Letters*, 55(18):1896.

Bui, T., Frampton, H., Huang, S., Collins, I. R., Striolo, A., and Michaelides, A. (2021). Water/oil interfacial tension reduction–an interfacial entropy driven process. *Physical Chemistry Chemical Physics*, 23(44):25075–25085.

Burnley, P. (2013). The importance of stress percolation patterns in rocks and other polycrystalline materials. *Nature Communications*, 4(1):1–6.

Butt, H.-J., Graf, K., and Kappl, M. (2023). *Physics and chemistry of interfaces*. John Wiley & Sons.

Butt, H.-J. and Kappl, M. (2018). *Surface and interfacial forces*. John Wiley & Sons.

Carroll, S. (2017). *The big picture: on the origins of life, meaning, and the universe itself*. Penguin.

Carroll, S. (2022). *The biggest ideas in the universe: Space, time, and motion*. Penguin.

Casteletto, V., Cantat, I., Sarker, D., Bausch, R., Bonn, D., and Meunier, J. (2003). Stability of soap films: hysteresis and nucleation of black films. *Physical Review Letters*, 90(4):048302.

Chacón, E., Reinaldo-Falagán, M., Velasco, E., and Tarazona, P. (2001). Layering at free liquid surfaces. *Physical Review Letters*, 87(16):166101.

Chacón, E. and Tarazona, P. (2003). Intrinsic profiles beyond the capillary wave theory: A monte carlo study. *Physical Review Letters*, 91(16):166103.

Chacón, E., Tarazona, P., and Alejandre, J. (2006). The intrinsic structure of the water surface. *The Journal of Chemical Physics*, 125(1):014709.

Chanda, J. and Bandyopadhyay, S. (2005). Molecular dynamics study of a surfactant monolayer adsorbed at the air/water interface. *Journal of Chemical Theory and Computation*, 1(5):963–971.

Chatzigiannakis, E. and Vermant, J. (2020). Breakup of thin liquid films: From stochastic to deterministic. *Physical Review Letters*, 125(15):158001.

Chen, D. Z., Shi, C. Y., An, Q., Zeng, Q., Mao, W. L., Goddard III, W. A., and Greer, J. R. (2015). Fractal atomic-level percolation in metallic glasses. *Science*, 349(6254):1306–1310.

Constante-Amores, C. R., Chergui, J., Shin, S., Juric, D., Castrejón-Pita, J., and Castrejón-Pita, A. A. (2022). Role of surfactant-induced marangoni stresses in retracting liquid sheets. *Journal of Fluid Mechanics*, 949:A32.

Courbin, L. and Stone, H. A. (2006). Impact, puncturing, and the self-healing of soap films. *Physics of Fluids*, 18(9).

Craster, R. V. and Matar, O. K. (2009). Dynamics and stability of thin liquid films. *Reviews of Modern Physics*, 81(3):1131.

Crowdy, D. G. (2021). Viscous marangoni flow driven by insoluble surfactant and the complex burgers equation. *SIAM Journal on Applied Mathematics*, 81(6):2526–2546.

Crowdy, D. G., Curran, A. E., and Papageorgiou, D. T. (2023). Fast reaction of soluble surfactant can remobilize a stagnant cap. *Journal of Fluid Mechanics*, 969:A8.

Culick, F. E. C. (1960). Comments on a ruptured soap film. *Journal of Applied Physics*, 31(6):1128–1129.

Dapp, W. B., Lücke, A., Persson, B. N., and Müser, M. H. (2012). Self-affine elastic contacts: Percolation and leakage. *Physical Review Letters*, 108(24):244301.

De Corato, M., Tammaro, D., Maffettone, P. L., and Fueyo, N. (2022). Retraction of thin films coated by insoluble surfactants. *Journal of Fluid Mechanics*, 942:A55.

de Gennes, P.-G. (2001). Some remarks on coalescence in emulsions or foams. *Chemical Engineering Science*, 56(19):5449–5450.

De Gennes, P.-G., Brochard-Wyart, F., and Quéré, D. (2013). *Capillarity and Wetting Phenomena: Drops, Bubbles, Pearls, Waves*. Springer Science & Business Media.

de Souza, V. K. and Harrowell, P. (2009). Rigidity percolation and the spatial heterogeneity of soft modes in disordered materials. *Proceedings of the National Academy of Sciences*, 106(36):15136–15141.

De Vries, A. (1958). Foam stability: Part v. mechanism of film rupture. *Recueil des Travaux Chimiques des Pays-Bas*, 77(5):441–461.

Debrégeas, G., De Gennes, P.-G., and Brochard-Wyart, F. (1998). The life and death of "bare" viscous bubbles. *Science*, 279(5357):1704–1707.

Debrégeas, G., Martin, P., and Brochard-Wyart, F. (1995). Viscous bursting of suspended films. *Physical Review Letters*, 75(21):3886.

Deka, H. and Pierson, J. L. (2020a). Revisiting the taylor-culick approximation. ii. retraction of a viscous sheet. *Physical Review Fluids*, 5:093603.

Deka, H. and Pierson, J.-L. (2020b). Revisiting the taylor-culick approximation. ii. retraction of a viscous sheet. *Physical Review Fluids*, 5(9):093603.

Derjaguin, B. and Prokhorov, A. (1981). On the theory of the rupture of black films. *Journal of Colloid and Interface Science*, 81(1):108–115.

Dhaliwal, V., Pedersen, C., Kadri, K., Miquelard-Garnier, G., Sollogoub, C., Peixinho, J., Salez, T., and Carlson, A. (2024). Instability and rupture of sheared viscous liquid nanofilms. *Physical Review Fluids*, 9(2):024201.

Diemand, J., Angélil, R., Tanaka, K. K., and Tanaka, H. (2014). Direct simulations of homogeneous bubble nucleation: Agreement with classical nucleation theory and no local hot spots. *Physical Review E*, 90(5):052407.

Dolganov, P., Shuravin, N., and Dolganov, V. (2020). Coalescence of holes in two-dimensional free-standing smectic films. *Physical Review E*, 101(5):052701.

Dupré, A. (1869). *Théorie mécanique de la chaleur*. Gauthier-Villars.

Durán-Olivencia, M. A., Gvalani, R. S., Kalliadasis, S., and Pavliotis, G. A. (2019). Instability, rupture and fluctuations in thin liquid films: Theory and computations. *Journal of statistical physics*, 174(3):579–604.

Dysthe, D., Fuchs, A., and Rousseau, B. (1999). Fluid transport properties by equilibrium molecular dynamics. i. methodology at extreme fluid states. *The Journal of chemical physics*, 110(8):4047–4059.

Eckertova, L. (2012). *Physics of thin films*. Springer Science & Business Media.

Eijkel, J. C. and Berg, A. v. d. (2005). Nanofluidics: what is it and what can we expect from it? *Microfluidics and Nanofluidics*, 1:249–267.

Erinin, M., Liu, C., Liu, X., Mostert, W., Deike, L., and Duncan, J. (2023). The effects of surfactants on plunging breakers. *Journal of Fluid Mechanics*, 972:R5.

Erneux, T. and Davis, S. H. (1993). Nonlinear rupture of free films. *Physics of Fluids A: Fluid Dynamics*, 5(5):1117–1122.

Evans, R., Henderson, J., Hoyle, D., Parry, A., and Sabeur, Z. (1993). Asymptotic decay of liquid structure: Oscillatory liquid-vapour density profiles and the fisher-widom line. *Molecular Physics*, 80(4):755–775.

Evers, L. J., Shulepov, S. Y., and Frens, G. (1996a). Rupture of thin liquid films from newtonian and viscoelastic liquids. bursting behaviour of newton-black films. *Faraday Discussions*, 104:335–344.

Evers, L. J., Shulepov, S. Y., and Frens, G. (1996b). Rupture of thin liquid films from newtonian and viscoelastic liquids bursting behaviour of newton-black films. *Faraday Discussions*, 104:335–344.

Evers, L. J., Shulepov, S. Y., and Frens, G. (1997). Bursting dynamics of thin free liquid films from newtonian and viscoelastic solutions. *Physical Review Letters*, 79:4850.

Ewen, J. (2017). *Molecular dynamics simulations of lubricants and additives*. PhD thesis, Imperial College London.

Fernández, E. M., Chacón, E., and Tarazona, P. (2011). Thickness and fluctuations of free and adsorbed liquid films. *Physical Review B*, 84(20):205435.

Florence, A. T. and Mysels, K. J. (1974). Bursting of soap films. vi. effect of surfactant purity. *The Journal of Physical Chemistry*, 78(3):234–235.

Forrest, J., Dalnoki-Veress, K., Stevens, J., and Dutcher, J. (1996). Effect of free surfaces on the glass transition temperature of thin polymer films. *Physical review letters*, 77(10):2002.

Frankel, S. and Mysels, K. J. (1969). Bursting of soap films. II. Theoretical considerations. *The Journal of Physical Chemistry*, 73(9):3028–3038.

Frenkel, D. and Smit, B. (2023). *Understanding molecular simulation: from algorithms to applications*. Elsevier.

Frenkel, D., Smit, B., and Ratner, M. A. (1996). *Understanding molecular simulation: from algorithms to applications*, volume 2. Academic press San Diego.

Gamba, Z., Hautman, J., Shelley, J. C., and Klein, M. L. (1992). Molecular dynamics investigation of a newtonian black film. *Langmuir*, 8(12):3155–3160.

Gao, A., Butt, H.-J., Steffen, W., and Schonecker, C. (2021). Optical manipulation of liquids by thermal marangoni flow along the air–water interfaces of a superhydrophobic surface. *Langmuir*, 37(29):8677–8686.

Gaver, D. P. and Grotberg, J. B. (1990). The dynamics of a localized surfactant on a thin film. *Journal of Fluid Mechanics*, 213:127–148.

Ge, S., Pu, Y., Zhang, W., Rafailovich, M., Sokolov, J., Buenviaje, C., Buckmaster, R., and Overney, R. (2000). Shear modulation force microscopy study of near surface glass transition temperatures. *Physical Review Letters*, 85(11):2340.

Ghosh, B. and Biswas, S. (2021). Polymeric micelles in cancer therapy: State of the art. *Journal of Controlled Release*, 332:127–147.

Ghoufi, A., Goujon, F., Lachet, V., and Malfreyt, P. (2008). Expressions for local contributions to the surface tension from the virial route. *Physical Review E*, 77(3):031601.

Ghoufi, A. and Malfreyt, P. (2019). Calculation of the surface tension of water: 40 years of molecular simulations. *Molecular Simulation*, 45(4-5):295–303.

Ghoufi, A., Malfreyt, P., and Tildesley, D. J. (2016). Computer modelling of the surface tension of the gas–liquid and liquid–liquid interface. *Chemical Society Reviews*, 45(5):1387–1409.

Gibbs, W. (1928). Collected works. I:219.

Gloor, G. J., Jackson, G., Blas, F. J., and de Miguel, E. (2005). Test-area simulation method for the direct determination of the interfacial tension of systems with continuous or discontinuous potentials. *The Journal of Chemical Physics*, 123(13):134703.

Goldstein, R. E., Huppert, H. E., Moffatt, H. K., and Pesci, A. I. (2014). Instability of a gravity current within a soap film. *Journal of Fluid Mechanics*, 753:R1.

Gordillo, L., Agbaglah, G., Duchemin, L., and Josserand, C. (2011). Asymptotic behavior of a retracting two-dimensional fluid sheet. *Physics of Fluids*, 23(12):122101.

Goujon, F., Ghoufi, A., Malfreyt, P., and Tildesley, D. J. (2016). Can we approach the gas–liquid critical point using slab simulations of two coexisting phases? *The Journal of Chemical Physics*, 145(12):124702.

Goujon, F., Malfreyt, P., and Tildesley, D. J. (2014). The gas–liquid surface tension of argon: A reconciliation between experiment and simulation. *The Journal of Chemical Physics*, 140(24):244710.

Greene, J. E. (2014). Tracing the 5000-year recorded history of inorganic thin films from 3000 bc to the early 1900s ad. *Applied Physics Reviews*, 1(4).

Griesser, H. J. (2016). *Thin film coatings for biomaterials and biomedical applications*. Woodhead Publishing.

Grotberg, J. B. (2001). Respiratory fluid mechanics and transport processes. *Annual Review of Biomedical Engineering*, 3(1):421–457.

Hammonds, K. and Heyes, D. (2020). Shadow hamiltonian in classical nve molecular dynamics simulations: A path to long time stability. *The Journal of Chemical Physics*, 152(2).

Hanyak, M., Sinz, D. K., and Darhuber, A. A. (2012). Soluble surfactant spreading on spatially confined thin liquid films. *Soft Matter*, 8(29):7660–7671.

Hasmy, A., Ispas, S., and Hehlen, B. (2021). Percolation transitions in compressed sio_2 glasses. *Nature*, 599(7883):62–66.

Hassan, N., Soltero, A., Pozzo, D., Messina, P. V., and Ruso, J. M. (2012). Bioinspired templates for the synthesis of silica nanostructures. *Soft Matter*, 8(37):9553–9562.

Henderson, J. (1986). Statistical mechanics of spherical interfaces. *CA Croxton (Wiley, New York, 1986)*.

Herminghaus, S., Jacobs, K., Mecke, K., Bischof, J., Fery, A., Ibn-Elhaj, M., and Schlagowski, S. (1998). Spinodal dewetting in liquid crystal and liquid metal films. *Science*, 282(5390):916–919.

Hernández-Sánchez, J. F., Eddi, A., and Snoeijer, J. H. (2015). Marangoni spreading due to a localized alcohol supply on a thin water film. *Physics of Fluids*, 27(3):032003.

Heyes, D. and Melrose, J. (1988). Percolation thresholds of simple fluids. *Journal of Physics A: Mathematical and General*, 21(21):4075–4081.

Heyes, D. and Melrose, J. (1990). Continuum percolation of 2d and 3d simple fluids. *Molecular Simulation*, 5(5):329–343.

Heyes, D. M. and Melrose, J. R. (1989). Microscopic simulation of rheology: Molecular dynamics computations and percolation theory. *Molecular Simulation*, 2(4-6):281–300.

Higgins, A. M. and Jones, R. A. (2000). Anisotropic spinodal dewetting as a route to self-assembly of patterned surfaces. *Nature*, 404(6777):476–478.

Hirsch, C. (2007). *Numerical Computation of Internal and External Flows: The Fundamentals of Computational Fluid Dynamics*. Elsevier Science.

Höfling, F. and Dietrich, S. (2015). Enhanced wavelength-dependent surface tension of liquid-vapour interfaces. *Europhysics Letters*, 109(4):46002.

Hoover, W. G. (1985). Canonical dynamics: Equilibrium phase-space distributions. *Physical Review A*, 31(3):1695.

Howell, P. and Stone, H. A. (2005). On the absence of marginal pinching in thin free films. *European Journal of Applied Mathematics*, 16(5):569–582.

Hulshof, H. (1901). The direct deduction of the capillarity constant γ as a surface tension. *Annalen der Physik*, 4:165–186.

Ibergay, C., Ghoufi, A., Goujon, F., Ungerer, P., Boutin, A., Rousseau, B., and Malfreyt, P. (2007). Molecular simulations of the n-alkane liquid-vapor interface: Interfacial properties and their long range corrections. *Physical Review E*, 75(5):051602.

Irving, J. and Kirkwood, J. G. (1950a). The statistical mechanical theory of transport processes. iv. the equations of hydrodynamics. *The Journal of Chemical Physics*, 18(6):817–829.

Irving, J. H. and Kirkwood, J. G. (1950b). The statistical mechanical theory of transport processes. IV. The equations of hydrodynamics. *The Journal of Chemical Physics*, 18:817.

Israelachvili, J. N. (2011). *Intermolecular and surface forces*. Academic press.

Israelachvili, J. N. (2022). Surface forces. In *The Handbook of Surface Imaging and Visualization*, pages 793–816. CRC Press.

Ivanov, I. B., Radoev, B., Manev, E., and Scheludko, A. (1970). Theory of the critical thickness of rupture of thin liquid films. *Transactions of the Faraday Society*, 66:1262–1273.

Jacobs, K., Herminghaus, S., and Mecke, K. R. (1998). Thin liquid polymer films rupture via defects. *Langmuir*, 14(4):965–969.

Jang, S. S. and Goddard, W. A. (2006). Structures and properties of newton black films characterized using molecular dynamics simulations. *The Journal of Physical Chemistry B*, 110(15):7992–8001.

Jasnow, D. and Vinals, J. (1996). Coarse-grained description of thermo-capillary flow. *Physics of Fluids*, 8(3):660–669.

Jelinek, H. F., Jones, C. L., Warfel, M. D., Lucas, C., Depardieu, C., and Aurel, G. (2006). Understanding fractal analysis? the case of fractal linguistics. *Complexus*, 3(1-3):66–73.

Jewett, A. I., Stelter, D., Lambert, J., Saladi, S. M., Roscioni, O. M., Ricci, M., Autin, L., Maritan, M., Bashusqeh, S. M., Keyes, T., et al. (2021). Moltemplate: A tool for coarse-grained modeling of complex biological matter and soft condensed matter physics. *Journal of molecular biology*, 433(11):166841.

Johansson, P., Galliéro, G., and Legendre, D. (2022). How molecular effects affect solutal marangoni flows. *Physical Review Fluids*, 7(6):064202.

Jones, J. E. (1924). On the determination of molecular fields.—ii. from the equation of state of a gas. *Proceedings of the Royal Society of London. Series A, Containing Papers of a Mathematical and Physical Character*, 106(738):463–477.

Kadau, K., Barber, J. L., Germann, T. C., Holian, B. L., and Alder, B. J. (2010). Atomistic methods in fluid simulation. *Philosophical Transactions of the Royal Society, Series A*, 368(1916):1547–1560.

Kadau, K., Germann, T. C., Hadjiconstantinou, N. G., Lomdahl, P. S., Dimonte, G., Holian, B. L., and Alder, B. J. (2004). Nanohydrodynamics simulations: An atomistic view of the rayleigh–taylor instability. *Proceedings of the National Academy of Sciences*, 101(16):5851–5855.

Kanduc, M., Stubenrauch, C., Miller, R., and Schneck, E. (2024). Interface adsorption versus bulk micellization of surfactants: Insights from molecular simulations. *Journal of Chemical Theory and Computation*, 20:1568–1578.

Kashchiev, D. and Exerowa, D. (1980). Nucleation mechanism of rupture of newtonian black films. i. theory. *Journal of Colloid and Interface Science*, 77(2):501–511.

Keller, J. B. (1983). Breaking of liquid films and threads. *Physics of Fluids*, 26(12):3451–3453.

Kempkes, S. N., Slot, M. R., Freeney, S. E., Zevenhuizen, S. J., Vanmaekelbergh, D., Swart, I., and Smith, C. M. (2019). Design and characterization of electrons in a fractal geometry. *Nature Physics*, 15(2):127–131.

Kim, H.-Y., Qin, Y., and Fichthorn, K. A. (2006). Molecular dynamics simulation of nanodroplet spreading enhanced by linear surfactants. *The Journal of Chemical Physics*, 125(17):174708.

Kirkwood, J. G. and Buff, F. P. (1949). The statistical mechanical theory of surface tension. *The Journal of Chemical Physics*, 17(3):338–343.

Kitahata, H. and Yoshinaga, N. (2018). Effective diffusion coefficient including the marangoni effect. *The Journal of Chemical Physics*, 148(13):134906.

Knutton, S. (1979). Studies of membrane fusion.: Iii. fusion of erythrocytes with polyethylene glycol. *Journal of Cell Science*, 36(1):61–72.

Kono, S., Kaneko, T., and Ueno, I. (2014). Elevation of the temperature of liquid films caused by rapid rupturing. *Physical Review E*, 90(5):051004.

Koplik, J. and Banavar, J. R. (1993). Molecular dynamics of interface rupture. *Physics of Fluids A: Fluid Dynamics*, 5:521–536.

Koplik, J. and Banavar, J. R. (2000). Molecular simulations of dewetting. *Physical review letters*, 84(19):4401.

Kuzmin, V. and Romanov, V. (1994). Influence of the surface profile on the roughness contribution to the ellipticity coefficient. *Physical Review E*, 49(4):2949.

Langevin, D. (2017). Aqueous foams and foam films stabilised by surfactants. gravity-free studies. *Comptes Rendus Mécanique*, 345(1):47–55.

Langevin, D. (2020). On the rupture of thin films made from aqueous surfactant solutions. *Advances in Colloid and Interface Science*, 275:102075.

Leckband, D. and Israelachvili, J. (2001). Intermolecular forces in biology. *Quarterly reviews of biophysics*, 34(2):105–267.

Leenaars, A., Huethorst, J., and Van Oekel, J. (1990). Marangoni drying: a new extremely clean drying process. *Langmuir*, 6(11):1701–1703.

Lei, Y. A., Bykov, T., Yoo, S., and Zeng, X. C. (2005). The tolman length: Is it positive or negative? *Journal of the American Chemical Society*, 127(44):15346–15347.

Lemmon, E. W. (1998). *Thermophysical Properties of Fluid Systems*. Nat. Inst. Stand. Tech. Gaithersburg.

Lhuissier, H. and Villermaux, E. (2009a). Destabilization of flapping sheets: The surprising analogue of soap films. *Comptes Rendus Mecanique*, 337(6-7):469–480.

Lhuissier, H. and Villermaux, E. (2009b). Soap films burst like flapping flags. *Physical Review Letters*, 103(5):054501.

Lobanova, O., Avendaño, C., Lafitte, T., Müller, E. A., and Jackson, G. (2015). Saft-γ force field for the simulation of molecular fluids: 4. a single-site coarse-grained model of water applicable over a wide temperature range. *Molecular Physics*, 113(9-10):1228–1249.

Lohse, D. and Villermaux, E. (2020). Double threshold behavior for breakup of liquid sheets. *Proceedings of the National Academy of Sciences*, 117(32):18912–18914.

Lu, X. and Hu, Y. (2008). *Molecular Thermodynamics of Complex Systems*, volume 131. Springer.

Maldarelli, C., Donovan, N. T., Ganesh, S. C., Das, S., and Koplik, J. (2022). Continuum and molecular dynamics studies of the hydrodynamics of colloids straddling a fluid interface. *Annual Review of Fluid Mechanics*, 54:495–523.

Malijevskỳ, A. and Jackson, G. (2012). A perspective on the interfacial properties of nanoscopic liquid drops. *Journal of Physics: Condensed Matter*, 24(46):464121.

Mandracchia, B., Wang, Z., Ferraro, V., Villone, M. M., Maio, E. D., Maffettone, P. L., and Ferraro, P. (2019). Quantitative imaging of the complexity in liquid bubbles' evolution reveals the dynamics of film retraction. *Light: Science and Applications*, 8:20.

Manikantan, H. and Squires, T. M. (2020). Surfactant dynamics: hidden variables controlling fluid flows. *Journal of fluid mechanics*, 892:P1.

Marrink, S., Tieleman, D., and Mark, A. (2000). Molecular dynamics simulation of the kinetics of spontaneous micelle formation. *The Journal of Physical Chemistry B*, 104(51):12165–12173.

Marrink, S. J. and Tieleman, D. P. (2013). Perspective on the martini model. *Chemical Society Reviews*, 42(16):6801–6822.

Martínez, L., Andrade, R., Birgin, E. G., and Martínez, J. M. (2009). Packmol: A package for building initial configurations for molecular dynamics simulations. *Journal of Computational Chemistry*, 30(13):2157–2164.

Masoud, H. and Stone, H. A. (2014). A reciprocal theorem for marangoni propulsion. *Journal of Fluid Mechanics*, 741:R4.

Masson, J.-L. and Green, P. F. (2002). Hole formation in thin polymer films: A two-stage process. *Physical Review Letters*, 88(20):205504.

McEntee, W. R. and Mysels, K. J. (1969). Bursting of soap films. I. An experimental study. *The Journal of Physical Chemistry*, 73(9):3018–3028.

Mecke, M., Winkelmann, J., and Fischer, J. (1997). Molecular dynamics simulation of the liquid–vapor interface: The Lennard-Jones fluid. *The Journal of Chemical Physics*, 107(21):9264–9270.

Menger, F. M. and Rizvi, S. A. (2011). Relationship between surface tension and surface coverage. *Langmuir*, 27(23):13975–13977.

Mitra, S. and Mitra, S. K. (2016). Understanding the early regime of drop spreading. *Langmuir*, 32(35):8843–8848.

Mitrinović, D. M., Tikhonov, A. M., Li, M., Huang, Z., and Schlossman, M. L. (2000). Noncapillary-wave structure at the water-alkane interface. *Physical Review Letters*, 85(3):582.

Moody, M. and Attard, P. (2001). Curvature dependent surface tension from a simulation of a cavity in a Lennard-Jones liquid close to coexistence. *The Journal of Chemical Physics*, 115(19):8967–8977.

Morariu, M., Schäffer, E., and Steiner, U. (2003). Capillary instabilities by fluctuation induced forces. *The European Physical Journal E*, 12:375–381.

Morciano, M., Fasano, M., Boriskina, S. V., Chiavazzo, E., and Asinari, P. (2020). Solar passive distiller with high productivity and marangoni effect-driven salt rejection. *Energy & Environmental Science*, 13(10):3646–3655.

Moreno-Boza, D., Martínez-Calvo, A., and Sevilla, A. (2020). Stokes theory of thin-film rupture. *Physical Review Fluids*, 5(1):014002.

Motaghian, M., van der Linden, E., and Habibi, M. (2022). Surfactant-surfactant interactions govern unusual marangoni spreading on a soap film. *Colloids and Surfaces A: Physicochemical and Engineering Aspects*, 653:129747.

Mu, Q., Lu, J., Ma, Y., Paz de Banez, M., Robinson, K., Armes, S., Lewis, A., and Thomas, R. (2006). Neutron reflection study of a water-soluble biocompatible diblock copolymer adsorbed at the air/water interface: The effects of ph and polymer concentration. *Langmuir*, 22(14):6153–6160.

Müller, F., Kornek, U., and Stannarius, R. (2007). Experimental study of the bursting of inviscid bubbles. *Physical Review E*, 75(6):065302.

Myers, D. et al. (1999). *Surfaces, interfaces, and colloids*, volume 415. Wiley New York.

Mysels, K. J. and Stikeleeather, J. A. (1971). The bursting of soap films iii. spontaneous and induced bursting. *Journal of Colloid and Interface Science*, 35:159–162.

Neél, B. and Villermaux, E. (2018). The spontaneous puncture of thick liquid films. *Journal of Fluid Mechanics*, 838:192–221.

Nguyen, T. D., Carrillo, J.-M. Y., Matheson, M. A., and Brown, W. M. (2014a). Rupture mechanism of liquid crystal thin films realized by large-scale molecular simulations. *Nanoscale*, 6(6):3083–3096.

Nguyen, T. D., Fuentes-Cabrera, M., Fowlkes, J. D., and Rack, P. D. (2014b). Coexistence of spinodal instability and thermal nucleation in thin-film rupture: Insights from molecular levels. *Physical Review E*, 89(3):032403.

Nijmeijer, M., Bakker, A., Bruin, C., and Sikkenk, J. (1988). A molecular dynamics simulation of the lennard-jones liquid–vapor interface. *The Journal of Chemical Physics*, 89(6):3789–3792.

Nikolova, A. and Exerowa, D. (1999). Rupture of common black films: Experimental study. *Colloids and Surfaces A: Physicochemical and Engineering Aspects*, 149(1-3):185–191.

Nosé, S. (1984). A molecular dynamics method for simulations in the canonical ensemble. *Molecular physics*, 52(2):255–268.

Nusse, H. E., Yorke, J. A., and Kostelich, E. J. (1994). Basins of attraction. *Dynamics: Numerical Explorations*, pages 269–314.

Oratis, A. T., Bush, J. W., Stone, H. A., and Bird, J. C. (2020). A new wrinkle on liquid sheets: Turning the mechanism of viscous bubble collapse upside down. *Science*, 369(6504):685–688.

O'Brien, S. (1996). Drying flow in a thin film induced by the presence of alcohol vapour. *Progress in Industrial Mathematics at ECMI 94*, pages 341–348.

Palmer, S. (1976). The effect of temperature on surface tension. *Physics Education*, 11(2):119.

Pandit, A. B. and Davidson, J. F. (1990). Hydrodynamics of the rupture of thin liquid films. *Journal of Fluid Mechanics*, 212:11–24.

Pannuzzo, M., Raudino, A., and Böckmann, R. A. (2014). Peptide-induced membrane curvature in edge-stabilized open bilayers: A theoretical and molecular dynamics study. *The Journal of Chemical Physics*, 141(2):024901.

Pathak, S. N., Esposito, V., Coniglio, A., and Ciamarra, M. P. (2017). Force percolation transition of jammed granular systems. *Physical Review E*, 96(4):042901.

Petit, P., Le Merrer, M., and Biance, A.-L. (2015). Holes and cracks in rigid foam films. *Journal of Fluid Mechanics*, 774:R3.

Piegari, A. and Flory, F. (2018). *Optical thin films and coatings: From materials to applications*. Woodhead Publishing.

Pierson, J.-L., Magnaudet, J., Soares, E. J., and Popinet, S. (2020). Revisiting the Taylor-Culick approximation: Retraction of an axisymmetric filament. *Physical Review Fluids*, 5(7):073602.

Pilgrim, I. and Taylor, R. P. (2018). Fractal analysis of time-series data sets: Methods and challenges. *Fractal analysis*, pages 5–30.

Planchette, C., Marangon, F., Hsiao, W.-K., and Brenn, G. (2019). Breakup of asymmetric liquid ligaments. *Physical Review Fluids*, 4(12):124004.

Possmayer, F., Zuo, Y. Y., Veldhuizen, R. A., and Petersen, N. O. (2023). Pulmonary surfactant: A mighty thin film. *Chemical Reviews*, 123(23):13209–13290.

Prévost, M. and Gallez, D. (1986). Nonlinear rupture of thin free liquid films. *The Journal of chemical physics*, 84(7):4043–4048.

Rafaı, S. and Bonn, D. (2005). Spreading of non-newtonian fluids and surfactant solutions on solid surfaces. *Physica A: Statistical Mechanics and its Applications*, 358(1):58–67.

Rahman, M. R., Shen, L., Ewen, J. P., Collard, B., Heyes, D., Dini, D., and Smith, E. (2023). Non-equilibrium molecular simulations of thin film rupture. *The Journal of Chemical Physics*, 158(15).

Ramírez-Garza, O., Méndez-Alcaraz, J., and González-Mozuelos, P. (2021). Effects of the curvature gradient on the distribution and diffusion of colloids confined to surfaces. *Physical Chemistry Chemical Physics*, 23(14):8661–8672.

Rapaport, D. C. (2004). *The Art of Molecular Dynamics Simulation*. Cambridge University Press.

Redon, C., Brochard-Wyart, F., and Rondelez, F. (1991). Dynamics of dewetting. *Physical review letters*, 66(6):715.

Reiter, G. (1992). Dewetting of thin polymer films. *Physical Review Letters*, 68(1):75.

Reiter, G. (1994). Dewetting as a probe of polymer mobility in thin films. *Macromolecules*, 27(11):3046–3052.

Reynolds, O. (1886). Iv. on the theory of lubrication and its application to mr. beauchamp tower's experiments, including an experimental determination of the viscosity of olive oil. *Philosophical transactions of the Royal Society of London*, (177):157–234.

Ribeiro, A. C., Lobo, V. M., Azevedo, E. F., Miguel, M. D. G., and Burrows, H. (2003). Diffusion coefficients of sodium dodecylsulfate in aqueous solutions and in aqueous solutions of β-cyclodextrin. *Journal of molecular liquids*, 102(1-3):285–292.

Rideg, N. A., Darvas, M., Varga, I., and Jedlovszky, P. (2012). Lateral dynamics of surfactants at the free water surface: a computer simulation study. *Langmuir*, 28(42):14944–14953.

Robertson, K. (2021). The demons haunting thermodynamics. *Physics Today*, 74(11):44–50.

Roché, M., Li, Z., Griffiths, I. M., Le Roux, S., Cantat, I., Saint-Jalmes, A., and Stone, H. A. (2014). Marangoni flow of soluble amphiphiles. *Physical review letters*, 112(20):208302.

Roth, C., Deh, B., Nickel, B., and Dutcher, J. (2005). Evidence of convective constraint release during hole growth in freely standing polystyrene films at low temperatures. *Physical Review E*, 72(2):021802.

Rowlinson, J. S. and Widom, B. (2013). *Molecular Theory of Capillarity*. Courier Corporation.

Ruckenstein, E. and Jain, R. K. (1974). Spontaneous rupture of thin liquid films. *Journal of the Chemical Society, Faraday Transactions 2: Molecular and Chemical Physics*, 70:132–147.

Sangwai, A. V. and Sureshkumar, R. (2011). Coarse-grained molecular dynamics simulations of the sphere to rod transition in surfactant micelles. *Langmuir*, 27(11):6628–6638.

Sanjay, V., Sen, U., Kant, P., and Lohse, D. (2022). Taylor–Culick retractions and the influence of the surroundings. *Journal of Fluid Mechanics*, 948:A14.

Santiago-Rosanne, M., Vignes-Adler, M., and Velarde, M. G. (2001). On the spreading of partially miscible liquids. *Journal of Colloid and Interface Science*, 234(2):375–383.

Saulnier, F., Raphaël, E., and De Gennes, P.-G. (2002). Dewetting of thin-film polymers. *Physical Review E*, 66(6):061607.

Saulnier, L., Champougny, L., Bastien, G., Restagno, F., Langevin, D., and Rio, E. (2014). A study of generation and rupture of soap films. *Soft Matter*, 10(16):2899–2906.

Savva, N. and Bush, J. W. (2009). Viscous sheet retraction. *Journal of Fluid Mechanics*, 626:211–240.

Schebarchov, D., Lefèvre, B., Somerville, W., and Hendy, S. (2013). Filling a nanoporous substrate by dewetting of thin films. *Nanoscale*, 5(5):1949–1954.

Scheludko, A. (1962). Sur certaines particularités des lames mousseuses. *Proceedings of the Koninklijke Nederlandse Akademie van Wetenschappen B*, 65:86–99.

Schmitt, S., Fleckenstein, F., Hasse, H., and Stephan, S. (2023). Comparison of force fields for the prediction of thermophysical properties of long linear and branched alkanes. *The Journal of Physical Chemistry B*, 127(8):1789–1802.

Schwerdtfeger, P. and Wales, D. J. (2024). 100 years of the lennard-jones potential. *Journal of Chemical Theory and Computation*.

Scriven, L. E. and Sternling, C. (1960a). The marangoni effects. *Nature*, 187:186–188.

Scriven, L. E. and Sternling, C. (1960b). The Marangoni effects. *Nature*, 187:186–188.

Seaton, N. and Glandt, E. D. (1987). Aggregation and percolation in a system of adhesive spheres. *The Journal of Chemical Physics*, 86(8):4668–4677.

Seemann, R., Herminghaus, S., and Jacobs, K. (2001). Dewetting patterns and molecular forces: A reconciliation. *Physical Review Letters*, 86(24):5534.

Sega, M., Horvai, G., and Jedlovszky, P. (2014). Two-dimensional percolation at the free water surface and its relation with the surface tension anomaly of water. *The Journal of Chemical Physics*, 141(5):054707.

Senapati, S. and Berkowitz, M. L. (2001). Computer simulation study of the interface width of the liquid/liquid interface. *Physical Review Letters*, 87(17):176101.

Seveno, D., Blake, T. D., and De Coninck, J. (2013). Young's equation at the nanoscale. *Physical Review Letters*, 111(9):096101.

Shah, P., Ward, E., Arora, S., and Driscoll, M. M. (2023). Rupture dynamics of flat colloidal films. *Physical Review Fluids*, 8(2):024002.

Sharma, A., Mittal, J., and Verma, R. (2002). Instability and dewetting of thin films induced by density variations. *Langmuir*, 18(26):10213–10220.

Sharma, A. and Reiter, G. (1996). Instability of thin polymer films on coated substrates: rupture, dewetting, and drop formation. *Journal of Colloid and Interface Science*, 178(2):383–399.

Sheludko, A. (1967). Thin liquid films. *Advances in Colloid and Interface Science*, 1(4):391–464.

Shen, L., Denner, F., Morgan, N., Van Wachem, B., and Dini, D. (2020). Transient structures in rupturing thin films: Marangoni-induced symmetry-breaking pattern formation in viscous fluids. *Science Advances*, 6(28):eabb0597.

Shen, Z., Sun, H., Liu, X., Liu, W., and Tang, M. (2013). Stability of newton black films under mechanical stretch–a molecular dynamics study. *Langmuir*, 29(36):11300–11309.

Shi, K., Smith, E. R., Santiso, E. E., and Gubbins, K. E. (2023). A perspective on the microscopic pressure (stress) tensor: History, current understanding, and future challenges. *The Journal of Chemical Physics*, 158(4):040901.

Shi, P., Zhang, H., Lin, L., Song, C., Chen, Q., and Li, Z. (2019). Molecular dynamics simulation of four typical surfactants in aqueous solution. *RSC Advances*, 9(6):3224–3231.

Shinoda, W., DeVane, R., and Klein, M. L. (2008). Coarse-grained molecular modeling of non-ionic surfactant self-assembly. *Soft Matter*, 4(12):2454–2462.

Shiri, R., Schmeller, L., Peschka, D., Seemann, R., and Wagner, B. (2023). Impact of noise on spinodal dewetting of liquid-liquid films. *Communications Physics*, 6(1):109.

Shu, D. and Gong, X. (2001). Curvature effect on surface diffusion: The nanotube. *The Journal of Chemical Physics*, 114(24):10922–10926.

Sides, S. W., Grest, G. S., and Lacasse, M.-D. (1999). Capillary waves at liquid-vapor interfaces: A molecular dynamics simulation. *Physical Review E*, 60(6):6708.

Smith, E. (2013). On the Coupling of Molecular Dynamics to Continuum Computational Fluid Dynamics, PhD thesis, Imperial College London.

Smith, E., Müller, E., Craster, R., and Matar, O. (2016). A langevin model for fluctuating contact angle behaviour parametrised using molecular dynamics. *Soft Matter*, 12(48):9604–9615.

Smith, E. R. (2022). The importance of reference frame for pressure at the liquid–vapour interface. *Molecular Simulation*, 48(1):57–72.

Smith, E. R. and Braga, C. (2020). Hydrodynamics across a fluctuating interface. *The Journal of Chemical Physics*, 153(13):134705.

Sprittles, J. E., Liu, J., Lockerby, D. A., and Grafke, T. (2023). Rogue nanowaves: A route to film rupture. *Physical Review Fluids*, 8(9):L092001.

Stange, T., Evans, D., and Hendrickson, W. (1997). Nucleation and growth of defects leading to dewetting of thin polymer films. *Langmuir*, 13(16):4459–4465.

Stauffer, D. and Aharony, A. (2018). *Introduction to Percolation Theory*. CRC press.

Stephan, S., Liu, J., Langenbach, K., Chapman, W. G., and Hasse, H. (2018). Vapor-liquid interface of the lennard-jones truncated and shifted fluid: Comparison of molecular simulation, density gradient theory, and density functional theory. *The Journal of Physical Chemistry C*, 122(43):24705–24715.

Stetten, A. Z., Iasella, S. V., Corcoran, T. E., Garoff, S., Przybycien, T. M., and Tilton, R. D. (2018). Surfactant-induced marangoni transport of lipids and therapeutics within the lung. *Current Opinion in Colloid & Interface Science*, 36:58–69.

Stillinger, F. H. and Weber, T. A. (1982). Hidden structure in liquids. *Physical Review A*, 25(2):978.

Stillinger Jr, F. H. (1963). Rigorous basis of the frenkel-band theory of association equilibrium. *The Journal of Chemical Physics*, 38(7):1486–1494.

Stone, H. (1990). A simple derivation of the time-dependent convective-diffusion equation for surfactant transport along a deforming interface. *Physics of Fluids A: Fluid Dynamics*, 2(1):111–112.

Stone, H. A., Stroock, A. D., and Ajdari, A. (2004). Engineering flows in small devices: microfluidics toward a lab-on-a-chip. *Annual Review of Fluid Mechanics*, 36:381–411.

Sünderhauf, G., Raszillier, H., and Durst, F. (2002). The retraction of the edge of a planar liquid sheet. *Physics of Fluids*, 14(1):198–208.

Tammaro, D., Chandran Suja, V., Kannan, A., Gala, L. D., Di Maio, E., Fuller, G. G., and Maffettone, P. L. (2021). Flowering in bursting bubbles with viscoelastic interfaces. *Proceedings of the National Academy of Sciences*, 118(30):e2105058118.

Tarazona, P., Chacón, E., and Bresme, F. (2012a). Intrinsic profiles and the structure of liquid surfaces. *Journal of Physics: Condensed Matter*, 24(28):284123.

Tarazona, P., Martínez, H., Chacón, E., and Bresme, F. (2012b). Newton black films as wetting systems. *Physical Review B*, 85(8):085402.

Taylor, G. (1959). The dynamics of thin sheets of fluid iii. disintegration of fluid sheets. *Proceedings of the Royal Society of London, Series A*, 253:313–321.

Taylor, G. I. and Michael, D. H. (1973). On making holes in a sheet of fluid. *Journal of Fluid Mechanics*, 58(4):625–639.

Temprano-Coleto, F. and Stone, H. A. (2024). On the self-similarity of unbounded viscous marangoni flows. *arXiv preprint arXiv:2401.13647*.

Theodorakis, P. E., Smith, E. R., and Müller, E. A. (2019). Spreading of aqueous droplets with common and superspreading surfactants. a molecular dynamics study. *Colloids and Surfaces A: Physicochemical and Engineering Aspects*, 581:123810.

Thiele, U., Mertig, M., and Pompe, W. (1998). Dewetting of an evaporating thin liquid film: Heterogeneous nucleation and surface instability. *Physical Review Letters*, 80(13):2869.

Thiele, U., Velarde, M. G., and Neuffer, K. (2001). Dewetting: Film rupture by nucleation in the spinodal regime. *Physical Review Letters*, 87(1):016104.

Thompson, A. P., Aktulga, H. M., Berger, R., Bolintineanu, D. S., Brown, W. M., Crozier, P. S., in't Veld, P. J., Kohlmeyer, A., Moore, S. G., Nguyen, T. D., et al. (2022). Lammps-a flexible simulation tool for particle-based materials modeling at the atomic, meso, and continuum scales. *Computer Physics Communications*, 271:108171.

Todd, B., Evans, D. J., and Daivis, P. J. (1995). Pressure tensor for inhomogeneous fluids. *Physical Review E*, 52(2):1627.

Todd, B. D. and Daivis, P. J. (2017). *Nonequilibrium molecular dynamics: theory, algorithms and applications*. Cambridge University Press.

Tolman, R. C. (1949). The effect of droplet size on surface tension. *The Journal of Chemical Physics*, 17(3):333–337.

Trittel, T., Harth, K., Klopp, C., and Stannarius, R. (2019). Marangoni flow in freely suspended liquid films. *Physical Review Letters*, 122(23):234501.

Trittel, T., John, T., Tsuji, K., and Stannarius, R. (2013). Rim instability of bursting thin smectic films. *Physics of Fluids*, 25(5):052106.

van Giessen, A. E. and Blokhuis, E. M. (2009). Direct determination of the tolman length from the bulk pressures of liquid drops via molecular dynamics simulations. *The Journal of Chemical Physics*, 131(16):164705.

Vaynblat, D., Lister, J. R., and Witelski, T. P. (2001). Rupture of thin viscous films by van der waals forces: Evolution and self-similarity. *Physics of Fluids*, 13(5):1130–1140.

Verlet, L. (1967). Computer experiments on classical fluids. i. thermodynamical properties of lennard-jones molecules. *Physical Review*, 159(1):98.

Verma, R. and Sharma, A. (2007). Defect sensitivity in instability and dewetting of thin liquid films: Two regimes of spinodal dewetting. *Industrial & Engineering Chemistry Research*, 46(10):3108–3118.

Villermaux, E. (2020). Fragmentation versus cohesion. *Journal of Fluid Mechanics*, 898:P1.

Vögele, M., Holm, C., and Smiatek, J. (2015). Properties of the polarizable martini water model: A comparative study for aqueous electrolyte solutions. *Journal of Molecular Liquids*, 212:103–110.

Vrabec, J., Kedia, G. K., Fuchs, G., and Hasse, H. (2006). Comprehensive study of the vapour–liquid coexistence of the truncated and shifted lennard–jones fluid including planar and spherical interface properties. *Molecular Physics*, 104(09):1509–1527.

Vrij, A. (1966a). Possible mechanism for the spontaneous rupture of thin, free liquid films. *Discussions of the Faraday Society*, 42:23–33.

Vrij, A. (1966b). Possible mechanism for the spontaneous rupture of thin, free liquid films. *Discussions of the Faraday Society*, 42:23–33.

Vrij, A. and Overbeek, J. T. H. G. (1968). Rupture of thin liquid films due to spontaneous fluctuations in thickness. *Journal of the American Chemical Society*, 90:3074–3078.

Walton, J., Tildesley, D., Rowlinson, J., and Henderson, J. (1983). The pressure tensor at the planar surface of a liquid. *Molecular Physics*, 48(6):1357–1368.

Wang, S. and Larson, R. G. (2015). Coarse-grained molecular dynamics simulation of self-assembly and surface adsorption of ionic surfactants using an implicit water model. *Langmuir*, 31(4):1262–1271.

Watanabe, K., Kusudo, H., Bistafa, C., Omori, T., and Yamaguchi, Y. (2022). Quantifying the solid–fluid interfacial tensions depending on the substrate curvature: Young's equation holds for wetting around nanoscale cylinder. *The Journal of Chemical Physics*, 156(5):054701.

Weiand, E., Rodriguez-Ropero, F., Roiter, Y., König, P. H., Angioletti-Uberti, S., Dini, D., and Ewen, J. P. (2023). Effects of surfactant adsorption on the wettability and friction of biomimetic surfaces. *Physical Chemistry Chemical Physics*, 25:21916–21934.

Wen, J., Dini, D., Hu, H., and Smith, E. R. (2021). Molecular droplets vs bubbles: Effect of curvature on surface tension and tolman length. *Physics of Fluids*, 33(7):072012.

Werth, S., Lishchuk, S. V., Horsch, M., and Hasse, H. (2013). The influence of the liquid slab thickness on the planar vapor–liquid interfacial tension. *Physica A*, 392(10):2359–2367.

Willard, A. P. and Chandler, D. (2010). Instantaneous liquid interfaces. *The Journal of Physical Chemistry B*, 114(5):1954–1958.

Williams, M. B. and Davis, S. H. (1982). Nonlinear theory of film rupture. *Journal of Colloid and Interface Science*, 90(1):220–228.

Wu, Z., Cui, Q., and Yethiraj, A. (2011). A new coarse-grained force field for membrane–peptide simulations. *Journal of Chemical Theory and Computation*, 7(11):3793–3802.

Xie, R., Karim, A., Douglas, J. F., Han, C. C., and Weiss, R. A. (1998). Spinodal dewetting of thin polymer films. *Physical Review Letters*, 81(6):1251.

Xu, Y., Deng, L., Ren, H., Zhang, X., Huang, F., and Yue, T. (2017). Transport of nanoparticles across pulmonary surfactant monolayer: a molecular dynamics study. *Physical Chemistry Chemical Physics*, 19(27):17568–17576.

Yaminsky, V. V., Ohnishi, S., Vogler, E. A., and Horn, R. G. (2010). Stability of aqueous films between bubbles. part 2. effects of trace impurities and evaporation. *Langmuir*, 26(11):8075–8080.

Yang, F. and Stone, H. A. (2020). Formation, rupture, and healing of an annular viscous film. *Physical review letters*, 124(22):224501.

Yeh, I.-C. and Hummer, G. (2004). System-size dependence of diffusion coefficients and viscosities from molecular dynamics simulations with periodic boundary conditions. *The Journal of Physical Chemistry B*, 108(40):15873–15879.

Yesylevskyy, S. O., Schäfer, L. V., Sengupta, D., and Marrink, S. J. (2010). Polarizable water model for the coarse-grained martini force field. *PLoS Computational Biology*, 6(6):e1000810.

Zarragoicoechea, G. J., Pugnaloni, L. A., Lado, F., Lomba, E., and Vericat, F. (2005). Percolation of clusters with a residence time in the bond definition: Integral equation theory. *Physical Review E*, 71(3):031202.

Zhang, Y., Sprittles, J. E., and Lockerby, D. A. (2019). Molecular simulation of thin liquid films: Thermal fluctuations and instability. *Physical Review E*, 100(2):023108.

Zhao, C., Liu, J., Lockerby, D. A., and Sprittles, J. E. (2022). Fluctuation-driven dynamics in nanoscale thin-film flows: physical insights from numerical investigations. *Physical Review Fluids*, 7(2):024203.

Zhao, C., Sprittles, J., and Lockerby, D. (2019). Revisiting the Rayleigh–Plateau instability for the nanoscale. *Journal of Fluid Mechanics*, 861:R3.

IMPERIAL